COMPOSITE PRODUCTION RISER ASSESSMENT

A Dissertation

by

WON KI KIM

Submitted to the Office of Graduate Studies of
Texas A&M University
in partial fulfillment of the requirements for the degree of

DOCTOR OF PHILOSOPHY

May 2007

Major Subject: Mechanical Engineering

COMPOSITE PRODUCTION RISER ASSESSMENT

A Dissertation

by

WON KI KIM

Submitted to the Office of Graduate Studies of
Texas A&M University
in partial fulfillment of the requirements for the degree of

DOCTOR OF PHILOSOPHY

Approved by:

Chair of Committee,	Ozden O. Ochoa
Committee Members,	J. N. Reddy
	Hung-Jue Sue
	Richard Mercier
Head of Department,	Dennis L. O'Neal

May 2007

Major Subject: Mechanical Engineering

ABSTRACT

Composite Production Riser Assessment. (May 2007)
Won Ki Kim, B.S., Yonsei University;
M.S., Yonsei University
Chair of Advisory Committee: Dr. Ozden O. Ochoa

The performance of a deep water composite production riser from a system perspective is presented, and its advantages are articulated through comparisons with a typical steel riser under identical service conditions. The composite riser joints in this study were considered to be a part of a single Tension Leg Platform (TLP) riser string to be installed at a depth of 6000 ft in Gulf of Mexico. A series of numerical analyses – burst, collapse, fatigue, global and local – have been performed, and the capacities of the composite riser have been determined utilizing long-term strength properties.

The capacities associated with the hoop direction, i.e., burst and collapse, are limited by the presence of a steel internal liner whose function is to ensure pressure and fluid tightness. The collapse capacity of the riser can be drastically impaired by the presence of a debond between the liner and composite.

Due to the high strength to weight ratio of the carbon/epoxy composite, its response under combined axial tension and bending moment showed great safety margins, favoring pursuits of greater water depths. The study also constructed damage envelopes associated with axial tension and bending moment, which facilitate feasibility checks for expanding the use of the composite joints to other locations or systems.

The fatigue life of the composite body is expected to greatly exceed its design life, and the most critical element is the welds between the liner and metal end pieces. Since there is wide dispersion of S-N relationships for carbon/epoxy composites depending on the combinations of constituent materials, a parametric study was carried out in this study to suggest the range of acceptable S-N relationships.

The composite riser is estimated to offer only moderate damping, due primarily to

its specially orthotropic lay-up. The study also demonstrates that the use of Rayleigh stiffness proportional damping may not be suitable for deep water risers. A series of forced excitation analyses show that the system in sea water does not show notable resonance due to fluid drag. When compared with the steel riser, vibration amplitudes at low elevations are much lower.

DEDICATION

To my parents

ACKNOWLEDGMENTS

I would like to express my gratitude to the committee chair, Dr. Ochoa, for her encouragement, guidance, and support. I would also like to thank my committee members, Dr. Reddy, Dr. Sue, and Dr. Mercier, for their insight and feedback. I truly appreciate the support and opportunity from the Offshore Technology Research Center – Dr. Ward and the staff – and the Minerals Management Service.

Many thanks to my lab mates, Melanie and Douglas, for their willingness to help and being such good friends. I am greatly indebted to my parents for their continuous support and encouragement. Last but not least, I would like to thank Jenny, for being a wonderful partner and supporter, and Ashley, for the precious smiles.

TABLE OF CONTENTS

Page

Page

LIST OF FIGURES

FIGURE Page

FIGURE Page

LIST OF TABLES

TABLE Page

1. INTRODUCTION

During the past two decades, offshore exploration and production activities have moved significantly into deeper water. It is estimated that Gulf of Mexico reserves amount to 32 billion barrels of oil equivalent, and annual production has been continually growing, with a compound annual growth rate from 1996 to 2003 of 38% [1]. Deep water reserves in the Gulf of Mexico are far larger than shallow water fields, and their average production is 12 times that of shallow fields [2]. Deep water production has been enabled by the introduction of new production system concepts, such as Tension Leg Platform (TLP), Spar, Floating Production System (FPS) and Subsea System. TLP and Spar systems, which are categorized as top tensioned systems, feature vertical access to wells and are known to be relatively insensitive to increase in water depth in terms of cost [3,4].

The TLP concept began to draw interest in the 1960s. In the early 1980s the first working TLP, Hutton, was deployed in the North Sea. The first TLP introduced to the Gulf of Mexico was Jolliet (89), which was followed by numerous other TLP systems: Auger (94), Mars (96), Ursa (98), Marlin (99), and Magnolia (04), to name a few. A distinctive feature of a TLP is its vertical moorings called tendons or tethers. Tendons connect the platform to the sea floor and are always in tension which is maintained by excess buoyancy provided by the hull of the platform. Due to the tendons in tension, the structure is horizontally compliant, but vertically stiff. Oil / gas is transferred from the wells to the platform through vertical production risers which house production tubing. Fig. 1 shows a schematic of Shell's Brutus TLP in the Gulf of Mexico.

Although TLPs are less sensitive to increase in water depth than traditional fixed platforms, manufacturing and operational costs still become significant issues when extended water depths are pursued. It is reported that every pound of the platform payload increase requires 1.3 lbs of fabricated steel and 0.65 lbs of additional mooring pretension, which translates into $4 to 7 /lb [5,6]. Since the weight of a riser increases

---

This dissertation follows the style of Composites Science and Technology.

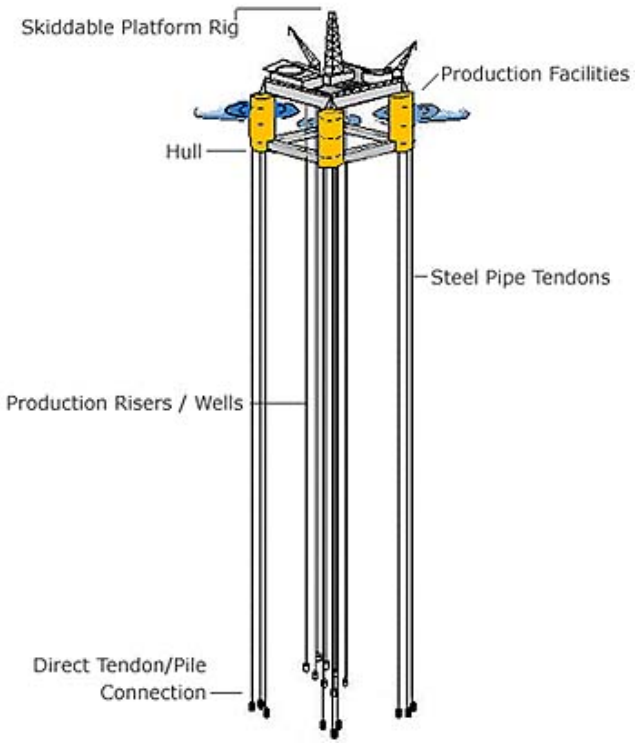

Fig. 1. Schematic of typical TLP [www.offshore-technology.com].

with water depth, deeper water necessitates higher top tension to be applied to the riser, and consequentially, more buoyancy of the hull. TLP size is not linearly dependent on the top tension, but increases at a higher rate as the top tension is larger. For higher tensioner capacity range, 700 kips or greater, a difference of one pound in the tensioner requirement is reflected by 2.11 times to the TLP size, while small top tension range, 500 kips or less, the ratio is only 1.33 [7].

Composite materials have attracted substantial attention from the offshore industry primarily due to their high specific strength. In addition to weight reduction, composites are expected to offer additional benefits such as excellent fatigue, damping, and thermal (insulation) properties, and high corrosion resistance. In spite of higher manufacturing

costs of composite risers, the transition from metallic risers to composite risers has become inevitable due to their influence on other system components and operational costs. Weight savings alone can bring significant impact on the design of a TLP system and total cost. Reduced riser weight directly affects required top tension which consequently lessens mooring tension and platform size. The significance of weight savings will be amplified for deeper water sites as the aforementioned studies predicts.

However, use of composites for offshore risers also introduces challenges and added complexities in design and analysis. First of all, the anisotropy of composite materials makes the current analysis technique not appropriate to composite riser analysis. Second, the construction of a composite riser is unavoidably far more complicated than conventional metallic risers. Since polymer matrix composites are not essentially water tight, additional barriers are required to ensure fluid tightness. Also, joining of riser segments, usually called joints, to form a long and continuous riser requires metallic end fittings. Due to the differences in material and construction, analysis of a composite riser may require different approaches than conventional riser analysis, and it is necessary to identify the particulars to which attention must be paid when analyzing a composite riser.

1.1. History of composite riser developments

The idea of introducing composite materials for offshore applications emerged decades ago. Composites are currently utilized for various platform topside components, spoolable piping and tubing, and flexible risers [4,8]. As the interest in deepwater reserves has grown immensely, numerous attempts are being made at developing composite tethers, buoyancy modules, and production and drilling risers to maximize the impact of the weight savings for deepwater operations [5,7,9-22].

The first attempt to design and analyze a composite production riser started in the 80's by Institut Francais du Petrole (IFP) and Aerospatiale of France [21,22]. IFP/Aerospatiale riser was designed for a concrete TLP in 500-1000 m water depth. The riser consists of internal and external buna liners, helical wound carbon fiber layers (±20°), and hoop wound glass fiber layers (90°). The inner diameter and wall thickness are 9 in and 0.7 in, respectively, and the length of one riser joint is approximately 50 ft. It was estimated that the apparent weight of the riser including tubing and couplings is 30 lbs/ft and the mean top tension for 1000 m water depth is 165 kips. Tests on burst, axial tension, tensile fatigue, and creep were carried out. For the burst and tension tests, failure occurred at 15.9 ksi and 1,047 kips. The tensile fatigue tests demonstrated that the riser has sufficient fatigue resistance, surviving after three times the number of cycles that would fail a steel riser.

In the mid 90's a joint industry project began, supported by National Institute of Standards and Technology (NIST) Advanced Technology Program (ATP), to develop a composite production riser [14-18] and a composite drilling riser [9,12,13]. The NIST/ATP composite production riser targeted deeper water, 3000 to 5000 ft, and both single and dual casing risers were considered. The wall has more complex construction than IFP/Aerospatiale riser does; there are carbon/glass hybrid hoop layers in addition to carbon helical layers and glass hoop layers. The weight of the composite tube and fittings is 27.0 lbs/ft. Numerous axial tension, burst, collapse, static fatigue, and impact tests were performed on short length and full-scale samples. It was reported that the burst, collapse, and axial tension capacities exceeded the requirements, reaching 11 ksi,

3.5 ksi, and 825 kips.

More recently, another joint industry project named the Magnolia composite production riser was initiated and is currently in progress [10]. The purpose of this project is to demonstrate the feasibility of fabricating a composite production riser joint that satisfies the same requirements as the steel joint used for the Magnolia TLP in the Gulf of Mexico in 4,700 ft water depth. The ultimate goal of this effort is to replace a few steel joints with prototype composite joints. Not all the details on the wall construction of the Magnolia composite production riser are made public, but it is known that the initial design had two inner liners, steel and rubber, and later the design was modified by adding a secondary steel liner between the rubber liner and structural composite layers.

Through these joint industry projects, it was demonstrated that the idea of using composites for production risers can be realized in the near future. Manufacturing technique is mature enough to fabricate riser joints that can meet the target capacities. However, there is lack of long term performance data for composite materials in actual sea environments. Although the effect of sea water absorption on moduli and strength has been investigated in many studies [23-27], the durations of exposure to sea water are not sufficiently long considering the usual service life of a production riser is greater than 25 years. Also, substantial amount of data for combined effect of sea water absorption, corrosion, and sustained loads need to be accumulated.

The aforementioned studies on composite production risers rely heavily on tests to quantify the capacity of the risers, in terms of axial tension, internal pressure (burst), external pressure (hydrostatic collapse), and impact. Testing does have its own importance especially for certification and reliability issues. However, computational predictions are of more significance for composite risers than they are for metallic risers due to the following reasons. First, failure of a composite part is not necessarily defined as the complete rupture of the part or specimen. There are multiple failure mechanisms, and one may occur as a result of another. Initiation and progression of damage and the mechanisms involved must be predicted when designing with composites. Second,

properties of composites exhibit significant dependence on time, permanent loads, and environment. It is nearly impossible to incorporate the effects of all these factors in a qualification testing, and test data must be complemented by numerical analyses where reduced material properties are used.

Since the past studies primarily focus on the performance on the joint level, the link between the global responses of a riser to its local behavior has not been fully explored. Bending moment is sometimes ignored, and the tensile capacity obtained through numerical analysis and tensile tests are compared with the requirements. This is acceptable for rough estimations, but contribution of bending differs from one riser system to another and for distinct environmental loading conditions. The maximum combined stress (axial and bending) under a certain sea state and operating condition has to be evaluated to achieve a better estimation of the safety factor for the particular condition. Especially for fatigue analysis, a small contribution of bending can cause a significant difference.

1.2. Overview of the study

This study will analyze a single string composite riser system which is part of a TLP in 6000 ft Gulf of Mexico environment. The riser system consists of wellhead, stress joint, tensioner joint, and surface tree, in addition to riser joints. A limited number of steel riser joints will be used near the stress joint and mean water level, where severe local loads are expected. Fig. 2 shows a schematic of the riser system to be analyzed in this study. Various aspects of the composite riser will be analyzed with ABAQUS finite element software.

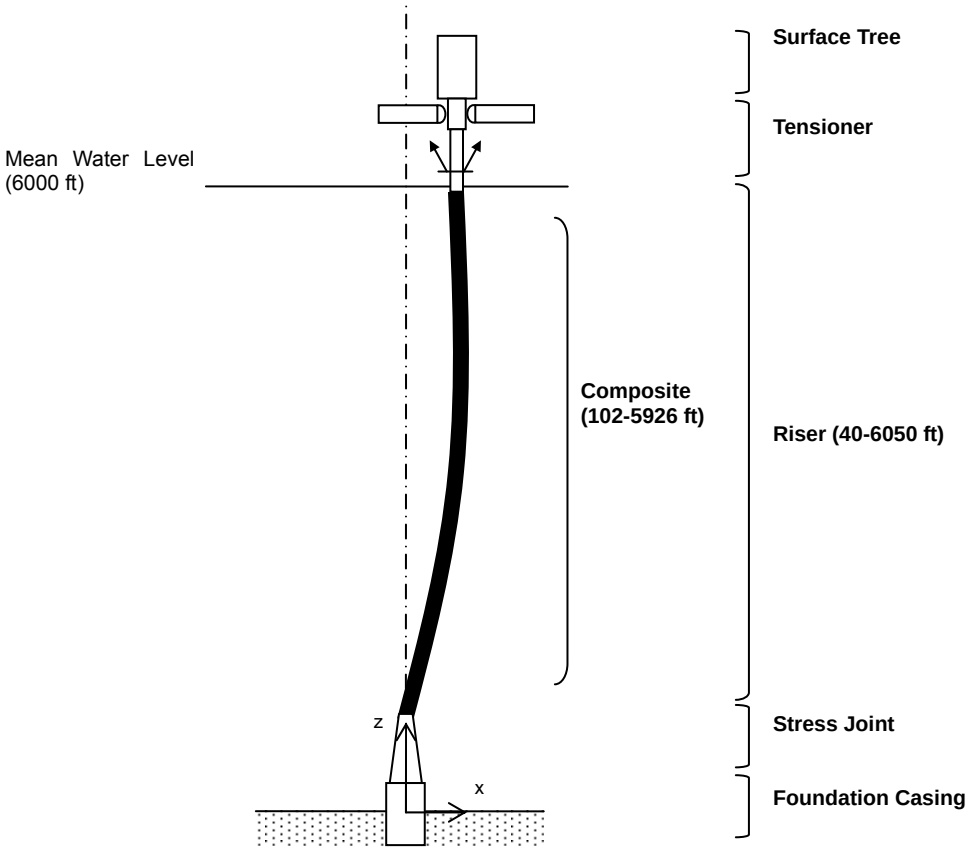

Fig. 2. Composite riser system configuration.

First, basic pressure capacities, i.e., burst and collapse, of the composite riser are estimated. In the burst analysis, the maximum internal pressure is applied to a riser section, and the stresses in all layers will be checked for failure. Then higher pressures are applied incrementally until fiber rupture occurs, and loss of stiffness resulting from initiation and progression of damage is applied to the finite element model. Collapse analysis is performed in a similar manner, but in this case the effect of debond areas between the structural composite body and internal liner will also be studied. When a debond exists, it may impair the collapse resistance of the composite riser. In addition, if sea water penetrates into the composite body building up pressure on the interface, local collapse of the internal liner may occur at a pressure far smaller than the collapse pressure of the riser section. Based on these scenarios, various debond geometry is incorporated in the analysis.

The combined loading responses are obtained in two steps: global and local. Analysis of a conventional metallic riser does not always require a local analysis. However, unlike isotropic materials, stresses and strains in each layer of the composite tubular are not conveniently calculated by simple formulas. In the global analysis, a few combinations of operational and environmental loads are applied to the complete riser system model. Based on the response data, a critical location along the span of the riser is selected, and the local load effects at this particular location, i.e., nodal forces and bending moment or displacements and rotation, are applied as the boundary conditions in the subsequent local analysis. Again, the failure analysis scheme used in the burst analysis is used in the local analysis.

In the fatigue analysis, wave fatigue at selected locations of the composite riser is estimated. Long term sea state is modeled by multiple sea states, and using the Rayleigh probability density function and S-N data, damage caused by each sea state is calculated. In addition to estimating total damage and fatigue life, representation of S-N data and effect of mean stress are discussed.

Lastly, the amount of damping in the composite riser is estimated based on the strain energy method, where damping is determined by the ratio of dissipated energy to

stored energy. Lamina damping properties in terms of specific damping capacity or loss factor are used to obtain the total dissipated energy. The value of damping thus obtained will be incorporated in an excitation simulation where the entire riser in water oscillates at one of its natural frequencies. The response will be compared with that of a steel riser and the composite riser with its damping ignored.

2. COMPOSITE RISER SPECIFICATIONS

2.1. Joint configuration

Risers are manufactured in short segments usually called joints. The length of one joint used in this study is 62 ft, and multiple joints are connected mechanically to form a long riser string. The mechanical connections require that the terminations of a composite tubular segment be attached to metal end fittings. The interface between the composite laminate and end fitting is called metal composite interface (MCI), and the most widely used type is the traplock concept [28-30] shown in Fig. 3. The end fitting has circumferential grooves, and each groove is filled by a group of layers during the winding process.

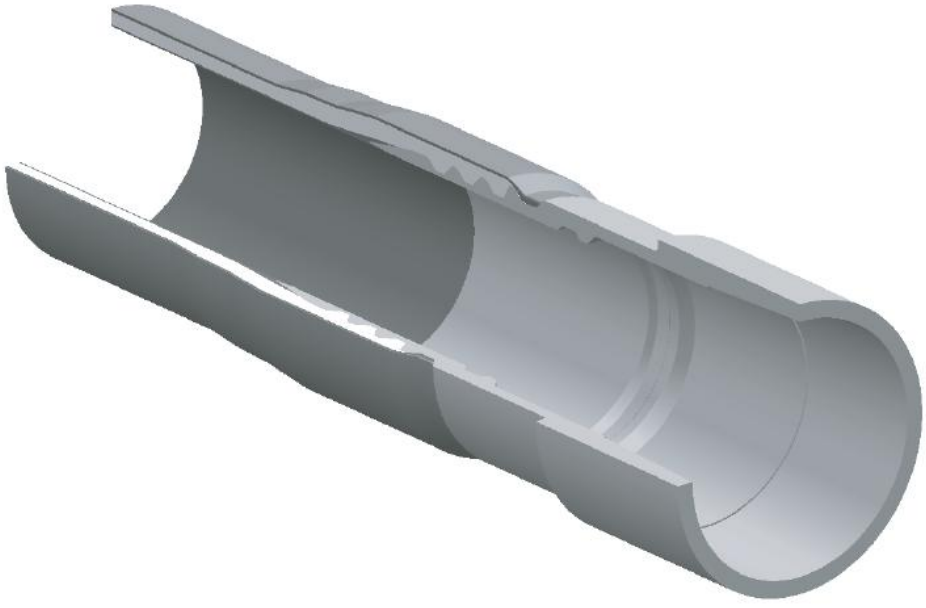

Fig. 3. Traplock metal to composite interface [1].

The construction of the composite production riser joint to be analyzed in this study is similar to those introduced in the past research activities. The most distinctive feature of the present design is a relatively thick steel internal liner. There is no additional polymeric liner, and the composite layers are attached directly to the steel liner. The terminations of the metal liner are welded to the end fittings. Generally, composite risers require external liners to ensure water-tightness and protect the structural composite body against gouging and impact. Since the external liners have no contribution toward load bearing, they are excluded from the subsequent analyses. However, their weight will be taken into account in the global analysis, based on an 1/8 in. thick glass-epoxy laminate. The structural composite body is composed of 19 alternating hoop (88°) and axial (0°) carbon-epoxy layers. Table 1 and 2 show the cross-sectional geometry and the layup of the composite body, respectively.

Table 1

Composite riser wall specifications

Overall			
	Inner Dia. (in)		9.720
	Outer Dia. (in)		12.414
Internal Liner			
	Thickness (in)		0.25
Structural Composite			
	Thickness (in)		0.972
		% Hoop	58.3
		% Axial	41.7
	Cross-Sectional Area (in^2)		34.176
		% Hoop	57.9
		% Axial	42.1
External Liner			
	Thickness (in)		0.125

Table 2

Composite riser layup

Layer	Orientation	Thickness (in)	Layer	Orientation	Thickness (in)
Liner		0.25	10	0	0.045
1	88	0.081	11	88	0.0405
2	0	0.045	12	0	0.045
3	88	0.081	13	88	0.0405
4	0	0.045	14	0	0.045
5	88	0.081	15	88	0.0405
6	0	0.045	16	0	0.045
7	88	0.081	17	88	0.0405
8	0	0.045	18	0	0.045
9	88	0.0405	19	88	0.0405

2.2. Material properties

The elastic properties of the carbon-epoxy lamina and structural steel are presented in Table 3. Using the classical lamination theory, the in-plane effective properties of the entire wall, including the internal liner, can be obtained. The effective properties in the global coordinates, where z and θ are axial and hoop directions, are presented in Table 4. The effective modulus in the axial direction is utilized in the global analysis, where the composite riser is represented by beam elements. When solving the problem of a pressurized riser, three-dimensional effective properties are needed. Calculation of out-of-plane effective properties is performed using the approach presented in Ref [31]. In this homogenization scheme, the relationship between macro-stress and macro-strain of a laminate is defined through the effective stiffness (or compliance) matrix, assuming the out-of-plane macro-stresses are same as the lamina

stresses in the corresponding directions. Table 5 presents the out-of-plane effective properties of the composite body.

Properties of composite materials exhibit dependence on time, permanent static loads, and the environment which includes water, chemicals, temperature, etc. Yet, there are no publicly available experimental data which account for all these factors comprehensively. In this study, a set of long-term lamina strengths presented in Ref. [6] is used in damage assessments.

Table 3

Lamina elastic properties

Carbon-Epoxy Lamina				Steel	
E_1 (msi)	E_2 (msi)	G_{12} (msi)	ν_{12}	E (msi)	ν
20.14	0.96	0.43	0.373	30	0.3

Table 4

In-plane effective properties of the riser

E_z (msi)	E_θ (msi)	$G_{z\theta}$ (msi)	$\nu_{z\theta}$
12.96	11.85	0.53	0.078

Table 5

Out-of-plane effective properties of the laminate

E_r (msi)	$G_{\theta r}$ (msi)	$\nu_{\theta r}$	ν_{rz}
0.96	0.43	0.226	0.0178

Table 6

Lamina long-term strengths

s_1^+ (ksi)	s_1^- (ksi)	s_2^+ (ksi)	s_2^- (ksi)	s_{12} (ksi)
220	150	5	22	10

2.3. Comparison with steel riser

As widely known, composites offer considerable amount of potential weight reductions over metals. From the perspective of axial tension, the required capacity of a riser is driven by its own weight, and the effect of weight savings is prominent. Table 7 shows the weights of bare composite joint, composite joint with fairings, and bare steel joint. Since most part of the riser system is submerged, effective weight is the most important measure. Effective weight is submerged weight of the riser including the internal fluid, whose density is much smaller than sea water in normal circumstances. When the end fittings are excluded, the effective weight of the main tube is slightly negative, even with the steel internal liner. Tensioner requirements are decided by multiplying the total effective weight of all the joints and tubing by a tension factor. For a tension factor of 1.3, the composite riser requires 319 kips of top tension, whereas a comparable steel riser requires 860 kips.

Table 7

Composite and steel riser weight comparison

	Air Wt.		Submerged Wt.		Effective Wt.		Effective Wt. w/ Tubing	
	Joint (lbs)	Unit (lbs/ft)	Joint (lbs)	Unit (lbs/ft)	Joint (lbs)	Unit (lbs/ft)	Joint (lbs)	Unit (lbs/ft)
Bare Joint	3698	59.65	2254	36.36	219	3.53	1916.56	30.91
w/ Fairings	4220	68.07	2404	36.78	369	5.96	2066.56	33.34
Steel Joint	7692	124.07	6687	107.86	4651	75.0	6348.56	102.38

3. ANALYSIS APPROACH

3.1. Pressure loads

One of the primary requirements for a production riser is to ensure pressure and fluid tightness. Leakage of internal fluids is especially of a great concern and should be avoided at all times. A riser is exposed to both internal and external pressures during its service life and is susceptible to two principal mishaps; failure of internal tubing and collapse due to external pressure associated with structural or manufacturing imperfections. The magnitude of external hydrostatic pressure is largest at the sea floor yet it is still less than the internal pressure. Even though the internal pressure is moderate (up to 100 psi) during normal operating condition, it rises significantly (8500 psi) when the internal tubing fails. The composite body including the liner, must remain intact under this circumstance.

3.1.1. Finite element models

Generally composite solid elements do not provide more accurate solution than composite shell elements [32] when modeling structures of moderate thickness subjected to in plane loads. However, for pressure capacity studies, the through the thickness stresses are not negligible. Thus ABAQUS C3D8 which is 8 noded hexahedron element is used for the burst and collapse analyses. Each node has three displacements, u, v, and w, as degrees of freedom. It is an isoparametric element, and therefore, linear interpolation is used. The interpolation function is presented in Appendix A.

The hexahedron C3D8 element has four integration points per section, and number of section points per lamina is defined by the user. Material properties for each layer can be specified in terms of engineering properties or entries in the stiffness matrix for an orthotropic material. Transverse isotropy is assumed when specifying material properties of each lamina. The constitutive relations are shown in Appendix B.

For the burst analysis, choice of element type and mesh refinement are of less importance since displacements are relatively small and hardly any distortion or bending of elements is involved. On the other hand, severe local bending occurs in the collapse analysis. Generally, quadratic (second order) elements provide more accurate results than linear elements for bending-dominated problems without complex contact conditions. However, as will be discussed later, the mesh needs to be partially disconnected in the collapse analysis to create various debond regions, and contact interaction is defined on the adjoining surfaces. In addition, manipulation of mesh to create various shapes and sizes of debond areas is more convenient when a linear element is used due to its simpler node pattern. To complement the bending behavior of C3D8 element and prevent node penetrations between the surfaces in contact, very fine mesh is used in the collapse simulation.

Shear locking occurs in structures that experience substantial bending loads when linear, fully integrated plane or solid elements are used in the models. Shear strains that are nonexistent in reality, called parasitic shear, create significant shear and bending resistance. A plausible approach to stay away from shear locking is to introduce incompatible mode elements that enhance bending behavior with additional incompatible modes as internal degrees of freedom. However, incompatible mode elements lose their accuracy when they have a parallelogram or trapezoidal shape. Also, incompatible mode elements are computationally more expensive than linear isoparametric elements. In order to assess the influence of element choices for the hoop buckling of a riser section, the following simulations are undertaken and compared: quadratic (C3D20), linear with full integration (C3D8), linear with reduced integration (C3D8R), and incompatible mode (C3D8I). Parasitic shear in linear elements and the interpolation functions for quadratic and incompatible mode elements are discussed in Appendix A as well.

3.1.2. Burst

The design pressure of the riser is set at 10 ksi, based on a maximum pressure of 8.5 ksi which is representative of a leak in the production tubing that requires well shut-in. Plane stress conditions that are routinely applied to estimate stresses in thin cylindrical pressure vessels are inadequate for the present effort. The wall of the composite production riser cannot be considered a thin wall since r/t ratio of thin-walled cylinders is usually about 10. Moreover, the wall consists of two different materials; steel liner and the composite laminate wall. The simplest approach one can take is to separate the steel internal liner and homogenize the structural composite layers into an equivalent orthotropic material as shown in Fig. 4 (a).

When the axial stress is neglected, the radial and tangential stress components of the isotropic liner are obtained using the following equations [33,34].

$$\sigma_r = \frac{p_i r_i^2 - p_o r_o^2 + (r_i r_o / r)^2 (p_o - p_i)}{r_o^2 - r_i^2} \tag{1}$$

$$\sigma_\theta = \frac{p_i r_i^2 - p_o r_o^2 - (r_i r_o / r)^2 (p_o - p_i)}{r_o^2 - r_i^2} \tag{2}$$

In this case, p_o for the liner is the interfacial pressure, p_{int}. For the liner, the radial displacement at a certain radial location r is

$$u_r = \frac{r}{E}(\sigma_\theta - \nu\sigma_r) \tag{3}$$

The radial displacement is expressed in terms of p_{int}, which is an unknown at this moment.

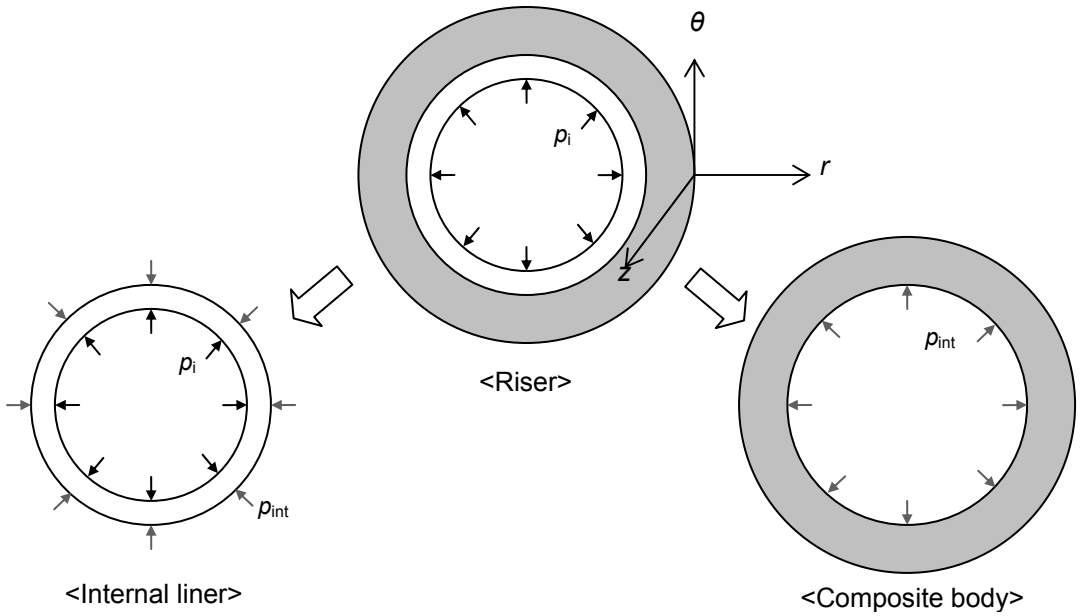

(a)

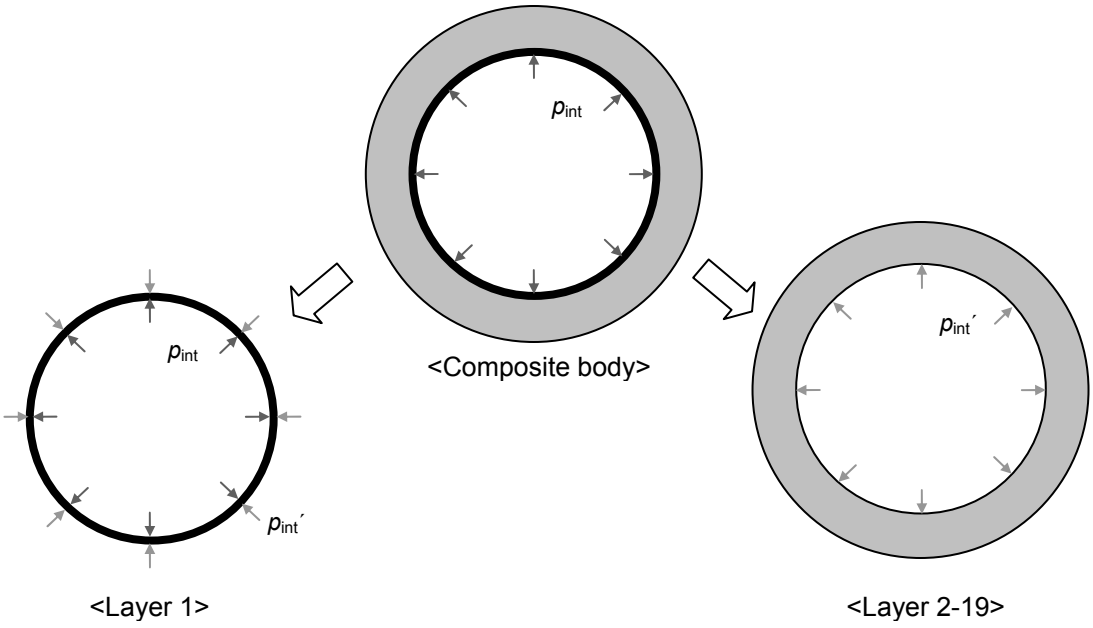

(b)

Fig. 4. Separation of two concentric cylinders under internal pressure. (a) liner and homogenized composite body, (b) layer 1 and homogenized layer 2 through 19.

Strains and radial displacement for the homogenized composite body as discussed in Section 2.2. are expressed in terms of the effective elastic properties of the laminate.

$$\varepsilon_r = \frac{\sigma_r}{E_r} - \frac{\nu_{\theta r}}{E_\theta}\sigma_\theta = \frac{du_r}{dr} \tag{4}$$

$$\varepsilon_\theta = \frac{\sigma_\theta}{E_\theta} - \frac{\nu_{r\theta}}{E_r}\sigma_r = \frac{u_r}{r} \tag{5}$$

$$u_r = r\left(\frac{\sigma_\theta}{E_\theta} - \frac{\nu_{r\theta}}{E_r}\sigma_r\right) \tag{6}$$

Differentiating Eqn (6) and equating the resulting equation with Eqn (4) gives

$$\frac{\sigma_\theta}{E_\theta} - \frac{\nu_{r\theta}}{E_r}\sigma_r + r\left(\frac{1}{E_\theta}\frac{d\sigma_\theta}{dr} - \frac{\nu_{r\theta}}{E_r}\frac{d\sigma_r}{dr}\right) = \frac{\sigma_r}{E_r} - \frac{\nu_{\theta r}}{E_\theta}\sigma_\theta \tag{7}$$

Use the following equilibrium equation for cylindrical coordinates [35] to replace σ_θ in Eqn (7) with σ_r and its derivative.

$$\sigma_r + r\frac{d\sigma_r}{dr} - \sigma_\theta = 0 \tag{8}$$

The resulting equation is

$$\left(\frac{1}{E_\theta} - \frac{1}{E_r}\right)\sigma_r + \frac{3}{E_\theta} r\frac{d\sigma_r}{dr} + \frac{1}{E_\theta} r^2 \frac{d^2\sigma_r}{dr^2} = 0 \tag{9}$$

This differential equation can be solved with the appropriate boundary conditions,

$\sigma_r(r_{\text{int}}) = -p_{\text{int}}$ and $\sigma_r(r_o) = 0$. Then σ_θ is also expressed as a function of r using Eqn (8), and Eqn (6) gives u_r at the interface in terms of the interfacial pressure, p_{int}.

Next, the continuity condition, which requires that the radial displacements of the liner (Eqn (3)) and composite body (Eqn (6)) at the interface should be identical, is utilized to identify the magnitude of p_{int}. Once the interfacial pressure is obtained, the stresses in the liner can be calculated by using Eqn (1) and (2). Now the problem has been reduced to the composite body with p_{int} applied as internal pressure to the innermost layer. Since the composite body is still thick, the simple average stress formula (pr/t) would not yield accurate answers. The stresses in the composite body can be estimated through repeating the same procedure. At this time, the innermost layer is treated as the inner tube, and the remainder of the composite body (layers 2 through 19) is homogenized into the outer tube, as sketched in Fig. 4 (b). Generally, a layer close to the center of a composite pipe experience higher stresses than ones farther from the inside. From the perspective of failure prediction, estimating the stress state of the innermost layer(s) is sufficient.

When the stresses in every layer need to be investigated, a more sophisticated approach can be used. Ref [36] proposed a solution procedure for cylinders consisting of specially orthotropic laminae. This approach is similar to the previous procedure for bulk, homogenous orthotropic materials. The difference lies in that the constitutive and equilibrium equations are now defined at the lamina level. When there are n layers, n equilibrium equations are solved simultaneously with $2n$ continuity conditions. Consequently, the solution is computationally more intensive, especially when the total number of layers is large. A similar approach was proposed in Ref [37], where each lamina is regarded as a general anisotropic material.

As discussed above, it is far more complicated to analyze a pressurized composite cylinder analytically when compared to analyzing an isotropic cylinder. The primary cause is the layered structure and discontinuity in stresses. The existence of a thick steel liner brings additional complexity. When the cylinder is axially unconstrained, an extra calculation step is required to calculate the longitudinal strain. In this case, the difference

in material and orientation between the layers results in different Poisson's ratios as well as stresses, and force equilibrium in the longitudinal direction is used to obtain the longitudinal strain. The stresses in the liner and the innermost hoop layer under the normal operating pressure are calculated for comparing the analytical and finite element solutions.

Finite element analysis tool is more convenient and enables more detailed investigation into the burst problem. Not only understanding the stress state under the design pressure, but also estimating burst capacity of the riser is essential. Failure of liner and each composite layer, i.e., pressure at which failure occurs, mode of failure, and loss of stiffness, needs to be incorporated into the burst capacity analysis. For the finite element model, a 10 ft cylinder is represented with hexahedral solid elements. The mesh consists of 60, 120, and 3 elements in the circumferential, longitudinal, and radial directions, respectively. The steel liner is represented by the innermost layer of elements, and the composite body is divided into two sublaminates which are represented by two layers of elements. The inner sublaminate contains the inner 8 layers, and the outer sublaminate contains the remaining 11 layers, which provides nearly identical sublaminate wall thicknesses. The radial and tangential degrees of freedom of the end nodes are constrained, and longitudinally the cylinder is free to contract.

A user material subroutine (UMAT) is utilized to incorporate a capability to identify damage modes and apply appropriate stiffness reduction. In the UMAT subroutine, the constitutive equation shown in Appendix B is specified, and a set of conditional statements are used to check the stresses at each integration point against a set of damage criteria. For this particular combination of lay-up, geometry, and loading condition, it is not likely that the riser will experience significant shear stresses. Therefore, simple maximum stress theory is implemented in the subroutine instead of other well-known interactive theories such as Hashin and Tsai-Hill criteria [38-41]. The lamina level stresses at every integration point are checked against the corresponding strengths in the user subroutine. If no damage is identified then the analysis proceeds to the next increment with the initial stiffness matrix maintained. If a certain damage mode

is detected, the subroutine applies discounts to the relevant entries in the stiffness matrix for the current integration point and updates the stress array using the discounted stiffness matrix. Also updated from the subroutine is the Jacobian matrix of the constitutive model, $\partial\Delta\sigma/\partial\Delta\varepsilon$. For linear elastic materials, the Jacobian matrix is identical to the stiffness matrix. As a result of loss of stiffness in one layer, additional stress is imposed on other layers.

Steel liner is assumed to be elastic-plastic, where its yield and ultimate strengths are 80 and 95 ksi and 17% elongation at failure is assumed. The design pressure, 10 ksi, is taken as the first load increment at the internal surface of the model, and the stresses in the liner and each layer of composite are investigated. The succeeding load increments are set to be 1 ksi in order for the UMAT subroutine to check for damage frequently, and the analysis is continued until fiber fracture in the hoop windings occurs.

3.1.3. Collapse

Hydrostatic pressure near the sea floor of 6,000 ft water depth is approximately 2.6 ksi. Therefore, it is highly unlikely that the entire wall will fail by hoop compression. However, collapse of a cylinder under external pressure can occur through hoop buckling, which is determined by the stiffness of the wall rather than its strength.

To assess the critical buckling pressure of a riser section, eigenvalue buckling analysis is performed in ABAQUS. Analytical solutions for buckling pressures of orthotropic cylinders have been proposed [42,43], but they are only applicable to thin-walled cylinders. In the problem of buckling under external pressure, as well as buckling under axial compression, critical load depends on the length of the cylinder for prescribed radius and wall thickness [44,45]. Generally, a shorter cylinder results in a higher critical pressure, and critical pressure shows very little dependence beyond a certain length. As a preliminary analysis, multiple riser sections with various lengths are analyzed to determine an appropriate model length for the subsequent analysis.

The finite element model used in this part of the study is similar to the previous

three-layer wall model. As mentioned previously, collapse analysis requires a highly refined model, and depending on the availability of computational resources, 90 or 120 elements in the circumference are be used. The number of elements in the longitudinal direction is 15 elements for every 10 inches for the former and 20 elements for the latter, totaling 180 and 240 elements in one row, respectively. The boundary conditions are the same as the burst analysis: constrained in the radial and tangential directions at both ends and longitudinally free at one end.

Although external liners are placed over the structural composite to prevent intrusion of sea water into the matrix of the composite, an extremely unfavorable situation is considered in this study; i.e., due to damage in the external liners, sea water penetrates into the composite body and through the end fittings. Then the water accumulates at the composite / liner interface and creates separation of the liner and the composite body. It is also assumed that the debond region is extensive, due to combined effects of initial flaws, sea water build up, service loads, thermal fatigue, etc. Two types of debond geometries shown in Fig. 5. are considered for the parametric studies. For the through-circumference type debond, length of the debond area is varied, and for the through-length type, arc angle is the variable. Eigenvalue buckling analysis is performed for each type of debond, and pressure loads are applied on the external surface and on the debond surfaces. It is assumed that there is no internal pressure, since the internal pressure under normal operating condition is not significant.

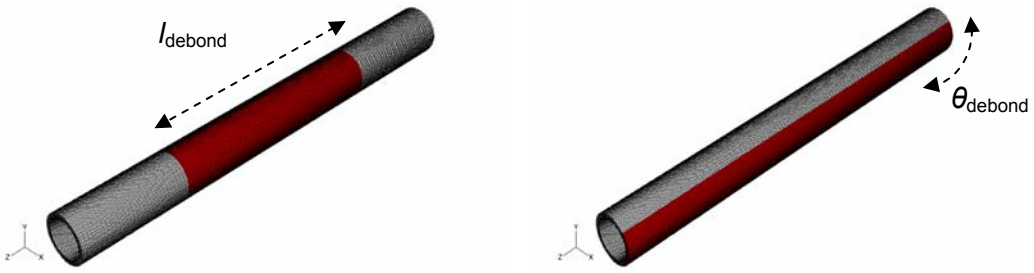

(a) (b)

Fig. 5. Debond types. (a) Through-circumference (b) Through-length.

Not only does the presence of a debond affect the hoop buckling pressure of the riser wall, it may also cause failure of the internal liner. If the sea water build-up results in a significant amount of pressure in the debond region, enough for the liner to yield, the steel liner may collapse plastically. In order to investigate this scenario, a static loading step is applied to each debond geometry. Equal amounts of pressure are applied incrementally to both the external surface and debond surfaces. Again, the material definition for steel is elastic-plastic with the same strengths used in the burst analysis. Since both geometric and material nonlinearities are involved in this case, the problem is analyzed with an artificial stabilization option to settle local instabilities. The stabilization is achieved through introducing an artificial viscous damping matrix, which is small enough not to change the behavior significantly but can prevent instantaneous collapse. The viscous damping used in this process is mass-proportional, and the damping factor (α) is chosen based on the prescribed ratio of the dissipated energy to the change in strain energy during the step [32].

3.2. Combined loads: tension and bending

In the combined loading analysis, the combined effects of functional and environmental loads in specific locations are examined. Unlike steel risers, stresses and strains in the composite riser cannot be directly obtained from a global analysis. Therefore, the analysis is carried out in two steps: global analysis and local analysis. In this study, a simplified global static analysis is performed due to the limitations of the available computing resources. Complete solutions for global dynamic analysis are provided by a collaborator [46].

3.2.1. Finite element models

The global analysis is performed with beam elements in a plane. The element of choice is B21H, which is a 2 node liner beam with hybrid formulation [32]. Being a linear element, it has one integration point in the middle. Each node has a total of three degrees of freedom: two displacements and one rotation. This element is a Timoshenko type beam and suitable for structures with large cross-sectional dimensions as well as slender structures, by allowing for transverse shear deformation. The rotation in the Timoshenko beam is independent of the transverse displacement. Therefore, the Lagrange interpolation can be used, whereas for the Euler-Bernoulli beam the Hermite cubic is used due to the need for interpolating both displacement and its derivative [47].

The hybrid formulation, sometimes called mixed element formulation, contains axial and shear forces as primary variables in addition to the displacements and rotation. For a flexing long pipe where there are large rotations, and the structure is rigid in axial tension and transverse shear, slight differences in nodal positions can result in large forces. Since the forces are primary variables, both force and displacement type variables are computed with comparable accuracy [48]. Throughout the model, pipe cross-sections are defined.

The global finite element model consists of 639 beam elements, most of which are

10 ft long. Higher level of discretization is used for the regions where there is transition in material or cross-sectional geometry. An additional rigid element representing the platform is created at the location of the tensioner centralizer. The tensioner ring is connected to the platform through a spring element, to which an appropriate linear load-displacement relationship is specified to incorporate the tensioner stiffness. Also a slider multi-point constraint is defined between the top region of the tensioner joint and the platform, in order for the riser to have relative movements vertically while its horizontal position is restricted by the platform. Therefore, top tension changes with the vertical motion of the riser relative to the platform, as well as the position of the platform.

Next, the local analysis is conducted with a cylinder consisting of shell elements. The length of the local model matches the dimension of the beam element or a set of elements at the location of interest selected upon inspecting the global analysis results. In this analysis, S8R element, an 8 node shell is used. This element categorized as a thick shell, since its formulation takes transverse shear into account. All six degrees of freedom, three displacements and three rotations, are active in every node. Since it has 8 nodes with no internal node, serendipity quadratic interpolation is used. For a 10 ft riser section, 20 and 80 elements are used along the circumference and length, respectively. This model is designated as TTT-1 (one element through the thickness). To ensure that no further mesh refinement is necessary, a 40 by 160 uniform mesh is used for one load case as a benchmark. In addition, a two-layer model, TTT-2, where an additional layer of elements is used to model the internal liner separately, is analyzed and compared with the original one-layer model. As seen in Fig. 6, the two layers overlap each other geometrically and share nodes, but different offset values are used to specify the locations of their mid-surfaces. For the liner, S8R5 thin shell element is utilized.

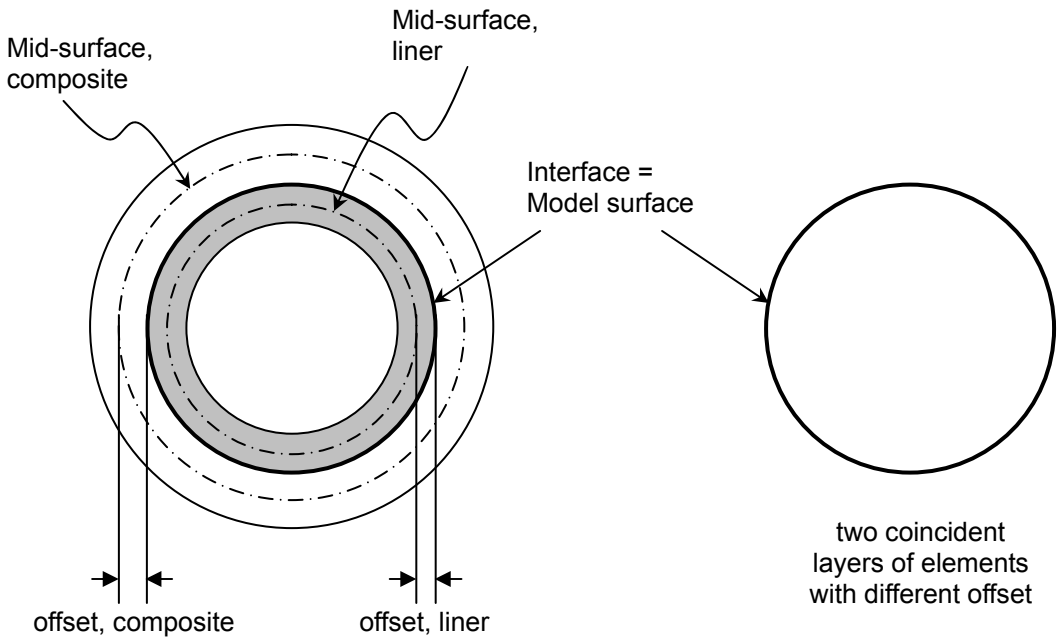

Fig. 6. Layering shell elements using offset.

When using a user material subroutine, the user must calculate and specify the transverse shear stiffness components. For composite materials, the transverse shear stiffnesses of the section can be obtained by equating the strain energy of the section resulting from shear forces with the sum of strain energies of individual layers, which can be obtained from transverse shear stresses and partial compliance matrices [32].

3.2.2. Global analysis

A real sea state is composed of multiple wave components. Incorporating numerous wave components into a direct integration (time domain) analysis is computationally expensive and requires multiple replicates. To overcome this difficulty, the frequency domain analysis technique is used, where regular wave solutions for multiple frequencies are superposed to obtain the irregular response [49]. This technique is not available in commercial finite element analysis codes, and only a single-wave time domain analysis is carried out in this study.

The governing equation for the lateral behavior of a riser subject to fluid forces is written as follows [50-52].

$$m\frac{\partial^2 x}{\partial t^2}+\frac{\partial^2}{\partial z^2}\left[EI(z)\frac{\partial^2 x}{\partial z^2}\right]-\frac{\partial}{\partial z}\left[T_e(z)\frac{\partial x}{\partial z}\right]+w(z)\frac{\partial x}{\partial z}=f(z,t) \tag{10}$$

where m: mass (per unit length) including contents, EI: bending stiffness, T_e: effective tension, w: weight.

The fluid force is represented by Morison's equation which consists of drag and inertia terms.

$$f(z,t)=\frac{1}{2}\rho C_D D\left(u-\frac{\partial x}{\partial t}\right)\left|u-\frac{\partial x}{\partial t}\right|+\rho A C_M\frac{\partial u}{\partial t}-\rho A(C_M-1)\frac{\partial^2 x}{\partial t^2} \tag{11}$$

where ρ: sea water density, u: fluid velocity, C_D: drag coefficient, C_M: inertia coefficient, D: diameter, A: entire area inside outer diameter.

According to the linear (Airy) wave theory, the horizontal fluid velocity for deep water, where the fluid particle orbits are circular, is given by the following equation [53].

$$u = \frac{\pi H}{T} e^{kz} \cos(kx - \omega t) \tag{12}$$

where H: wave height, T: period, k: wave number (=2π / wavelength), ω: wave angular frequency.

The loads to be applied in the global single wave analysis are based on the 100 year hurricane load case in a Gulf of Mexico location. The effective moduli presented in Section 2.2. are assigned to the composite riser region. The rest of the system, i.e., stress joint, steel riser joints, tensioner joint, etc., is made of steel with a Young's modulus of 30 msi. The joints in the top 1/3 of the composite riser region have fairings, which are streamlined devices for suppressing vortex-induced vibration (VIV). The contribution of the fairings to the stiffness of the joints is assumed to be negligible, but the increase in weight caused by the addition of the fairings is taken into account. The boundary condition at the very bottom of the system, 20 ft below the sea floor, is fixed, with an initial rotation of 1°. As discussed previously, the boundary condition at the top varies with the platform motion and relative vertical movement of the riser with respect to the platform.

Before all the loads are applied, the model is fine-tuned with the component weights and top tension only. Generally, top tension is one to two times greater than the sum of the effective weights of all the joints, depending on the service condition. The main purposes keeping the entire riser in tension are to control its deflection and to prevent buckling due to axial compression. In this study, a tension factor of 1.3 is used, which amounts to a nominal top tension of 319 kips. The stiffness of the tensioner is set to be 38.28 kips/ft. Since the top tension exceeds the total effective weight, the riser system is stretched upon application of the weight and top tension. The node definitions and the load-displacement curve for the tensioner should be adjusted iteratively until the top joints are at the desired elevations and the top tension is at the nominal value when the equilibrium is reached.

When the fine-tuning of the initial configuration and tensioner is completed, the

mean offset of the platform is applied. The amount of offset is 360 ft, and a downward setdown, which is a quadratic function of offset, is applied. As the final step, environmental loads and dynamic platform motions are applied simultaneously. In this particular scenario, the platform surge lags the wave by 90° and its amplitude is 64 % of the wave amplitude. The heave motion of the platform is relatively small compared to the setdown, and for this reason heave is neglected in this study. This time-dependent boundary condition is applied through a user subroutine for ABAQUS.

A sea state is often represented by significant wave height, H_s. Significant wave height is the average of the highest one-third of the waves during the sampling period, and this measure best represents the estimates made by experienced observers. The height of the highest 1% waves is approximately 1.67 times H_s, and theoretically the maximum wave height is 1.86 times greater than H_s. The wave height of the single wave applied in the time domain analysis is set to be the maximum wave height. Table 8 presents the major parameters for the environmental loading.

Table 8

Specifications for environmental loading: simplified single wave analysis

Surface Current (ft/sec)	H (ft)	T (sec)	C_D	C_M
4.0	76	14	1.0	2.0

The results of the single wave time domain analysis are compared with the frequency domain solutions for the 100 year hurricane condition. Additional load cases analyzed through frequency domain analysis are 100 year loop current and 1 year winter storm. The major parameters in the storm definitions are presented in Table 9 [46]. When

the frequency domain method is used, the drag force term in Eqn. (11) must be linearized with caution to minimize the loss of accuracy [54-56]. The results from frequency domain analysis are in root mean square, mean, and zero-crossing period of the responses. The maximum response is estimated using the following extreme factor F [54].

$$F \approx \sqrt{2\ln[D/(T_z P_e)]} \tag{13}$$

where D: duration of condition, T_z: zero-crossing period, P_e: exceedence probability. The maximum response is obtained by multiplying the root mean square response by the extreme factor and then adding the mean response.

Table 9

Specifications of storm conditions for frequency domain analysis

Storm Condition	H_s	T	Platform Offset	Tension Factor	RMS Low Freq. Motion
100 Year Hurricane	41	14	360	1.3	22.2
100 Year Loop Current	9	8	540	1.6	2
1 Year Winter Storm	16	9	120	1.3	6

3.2.3. Local analysis

Examination of global analysis solutions reveals the location which is most likely to have the largest total stress, which is a sum of the stresses due to tension and bending moment. Then a section corresponding to or enclosing the location of interest is defined, and the nodal forces and bending moment at the top and rotation at the bottom of the section are applied as boundary conditions for the subsequent local analysis. Alternatively, rotation and relative displacements can be applied at the top if the magnitudes provide sufficient precision. The boundary conditions are applied such that the nodes at each termination move as a rigid body. This can be achieved by placing rigid elements along the termination nodes and connecting them to a reference node in the center of the circle. Then the boundary conditions are applied to the reference nodes at the terminations. In the local analysis, the mean and maximum solutions from the global frequency domain analysis data are used. With the mean solutions applied, the reaction forces and moments at the bottom end of the local model match the global results. However, due to the fact that generally the maximum section forces and moment do not take place simultaneously, the local analyses under maximum solution yield slightly conservative estimates of the state of stress in the section. Table 10 shows the nodal forces and displacements at the top of the composite riser region as provided by the global frequency domain analysis [46].

Table 10

Boundary conditions for local analyses

Storm Condition		Top (5926 ft)			Bottom (5916 ft)
		F_x (lbs)	F_z (lbs)	M_y (lbs-ft)	θ_y (rad)
100 Year Hurricane	mean sol.	7904.68	301213.96	-4800.83	0.026454
	max. sol.	23769.88	364819.75	-15568.12	0.076733
100 Year Loop Current	mean sol.	7311.45	340489.85	-10558.37	0.022121
	max. sol.	9994.78	346495.03	-15144.42	0.029844
1 Year Winter Storm	mean sol.	2657.50	275291.03	-806.96	0.009666
	max. sol.	6103.77	283007.32	-6485.48	0.022041

As the boundary conditions are applied incrementally, a user material subroutine checks for damage and applying appropriate stiffness reductions according to the damage mode. The subroutine is similar to the one used in the burst analysis, except the constitutive equation is based on a state of plane stress. As discussed in Appendix A, the stress-strain relationship reduces to a 3 by 3 stiffness matrix consisting of four independent elastic constants.

In addition to evaluating failure based on the global analysis data, local analysis technique can be utilized to construct a failure envelope when various sets of loads are applied. A failure envelope may consist of any combination of pressure, axial tension and compression, bending moment, and torsion. For traditional metallic risers, since pressure and axial load are the principal loads, a failure envelope is usually constructed with these two loads as the main axes. On the other hand, in the composite body, coupling between axial load and pressure is not as significant since the laminate is near

cross-ply; the fibers in the axial layers carry the axial load, and the hoop fibers carry the pressure load. Instead of the combination of axial load and pressure, axial tension and bending moment is considered in this study. Unlike isotropic materials, failure of the entire wall does not occur in a concurrent manner, since it consists of multiple material systems, i.e., composite and steel, with the composite laminae having two different orientation angles. Therefore, not only failure of the entire wall (indicated by fiber fracture in the axial layers), but also damage in the secondary load bearing elements, i.e., yielding of the steel liner and matrix cracking in the hoop layers, needs to be identified. The failure envelopes will be useful for determining if the composite joints can be used in other circumstances, i.e., different loading conditions and/or system configurations. Once the failure envelope is established, global analysis data are sufficient for evaluating the serviceability of the composite joints, and the need for further local analyses can be eliminated.

3.3. Cyclic fatigue

In this section, evaluation of wave fatigue of the composite riser is discussed. First, global frequency domain solutions provided by Ref. [46] are converted into mean and root mean square stresses for a layer. Then a stress histogram, which represents applied stresses and corresponding durations for the particular layer incurred by a certain sea state, is generated through the Rayleigh probability density function. The cycles to failure at each category, i.e., stress level, of the histograms is evaluated through an S-N curve, with an optional extrapolation process where the raw mean and amplitude of the stress are converted to a set of equivalent mean and amplitude that matches the S-N curve. After this step is applied to all stress levels of every sea state, the well-known Palmgren-Miner's cumulative damage rule [57] is utilized to obtain total fatigue damage and life.

Fatigue of composites is a complex phenomenon where multiple damage mechanisms are involved. In general, a laminate coupon subject to cyclic loading undergoes matrix cracking, often followed by delamination and fiber/matrix debonding. As the number of cycle increases, fiber fails by brittle rupture. Since fatigue of composites is heavily dependent on constituent materials and lay-up, it is very difficult to accurately predict the fatigue behavior of a specific laminate without experimental works. Numerous analytical models for composite fatigue have been proposed during the past few decades, based on such concepts as residual stiffness [58,59], residual strength [60-64], or damage rate [65,66]. Unfortunately, there is no damage model that is widely accepted for common use or proven to yield excellent results regardless of material and lay-up. Also, attempts to introduce new damage measures and cumulative damage rules for multi-magnitude loading scenarios have been made, some of which are compiled in Ref. [67]. However, none of these models is as widely accepted as Miner's rule.

The fatigue performance of the composite riser cannot be readily evaluated on the laminate level since no S-N curve for this composite wall lay-up is available. However, a

simplified analysis procedure based on lamina-level fatigue is possible since the laminate is practically a cross-ply in a tubular geometry. In other words, the material is specially orthotropic, with the material coordinates coinciding with the global cylindrical coordinates. It is assumed that fatigue mechanisms involved in this particular case are only matrix cracking in hoop layers and fiber rupture in axial layers, excluding secondary mechanisms such as longitudinal fiber splitting and delamination. Being a tube, the composite wall has no free edges where excessive interlaminar stresses often lead to delamination. In general, fatigue of the primary load bearing layers (0°) in cross-ply laminates is hardly affected by other damage modes, and the only way matrix cracking in the hoop layers influences fatigue of the axial layers is by increasing the stresses on the axial layers [60,68].

In this study, fatigue failure of the composite riser is defined as failure of the outermost axial layer, which experiences the largest stress among all layers, and fatigue damage is evaluated at this layer only. When calculating the stresses in this layer induced by wave loading, it is assumed that the hoop layers carry no axial loads, thus eliminating the need for updating the stresses in the axial layers according to developing fatigue damage in the hoop layers. Discounting the entire hoop layers causes an increase of a few percent in σ_1 of the outermost axial layer. It is also assumed that stiffness degradation of the axial layers over long term exposure to service loads is negligible.

To obtain the applied stress levels, the frequency domain analyses data from Ref are utilized. Generally, a long term sea state is modeled by a series of short term sea states with different probability of occurrence. Each sea state has distinct wave characteristics represented by significant wave height and zero-crossing period. The frequency domain analyses results contain local axial tension and bending moment at the bottom (102 ft) and top (5926 ft) of the composite riser region. The results are presented in terms of mean and root mean square values for 27 short term sea states. As shown in Table 11, the low sea states are characterized by small and short waves with high probability of occurrence, and the opposite applies to the high sea states. Due to the differences in wave specifications, the statistical distributions of axial tension and

bending moment resulting from each sea state differ from others. Since global analysis does not directly provide layer-by-layer stresses, axial tension and bending moment are converted into tensile stress and bending stress on the lamina level through finite element analyses. The total stress is simply an algebraic sum of the two stress components.

Table 11

Sea states for wave fatigue assessment

Sea State	H_s (ft)	T_z (sec)	**Probability**	**Sea State**	H_s (ft)	T_z (sec)	**Probability**
1	2	2	0.041895	15	16	7.5	0.000514
2	2	3	0.22055	16	18	7.7	0.000354
3	2	4	0.10194	17	20	7.9	0.000251
4	4	3	0.081279	18	22	8.1	0.00016
5	4	4	0.19041	19	24	8.3	0.000103
6	4	5	0.053197	20	26	8.6	6.85E-05
7	6	4	0.088356	21	28	8.8	5.14E-05
8	6	5	0.072831	22	30	9	3.03E-05
9	6	6	0.013813	23	32	9.2	2.28E-05
10	8	5	0.041781	24	34	9.4	1.37E-05
11	8	6	0.016324	25	36	9.7	9.7E-06
12	10	6	0.013242	26	38	9.9	6.51E-06
13	12	6	0.005137	27	41	10.3	4.34E-06
14	14	6.5	0.003311				

Usually, fatigue analysis of an offshore structure utilizes a stress energy spectrum for which the wave energy spectrum is scaled by a transfer function at a location of interest for the given sea state. Instead of constructing a transfer function for the composite riser, the root mean square values of the total stresses can be utilized. The Rayleigh probability density function and cumulative probability function for a stress range distribution of each sea state are given by the following equations [46,69].

$$p(\Delta\sigma) = \frac{\Delta\sigma}{4\sigma_{RMS}{}^2} \exp\left[-\frac{\Delta\sigma^2}{8\sigma_{RMS}{}^2}\right] \quad \textbf{(}14\textbf{)}$$

$$P(\Delta\sigma) = 1 - \exp\left[-\frac{\Delta\sigma^2}{8\sigma_{RMS}{}^2}\right] \quad \textbf{(}15\textbf{)}$$

where $\Delta\sigma$: stress range (= 2 × σ_{amp}), σ_{RMS}: root mean square of stresses under the sea state (= square root of the 0-th spectral moment). The peak of the probability density function turns sharper and narrower as σ_{RMS} becomes smaller. Fig. 7 shows an example of probability density and cumulative probability, where interval = 0.002 ksi and σ_{RMS} = 0.1426 ksi.

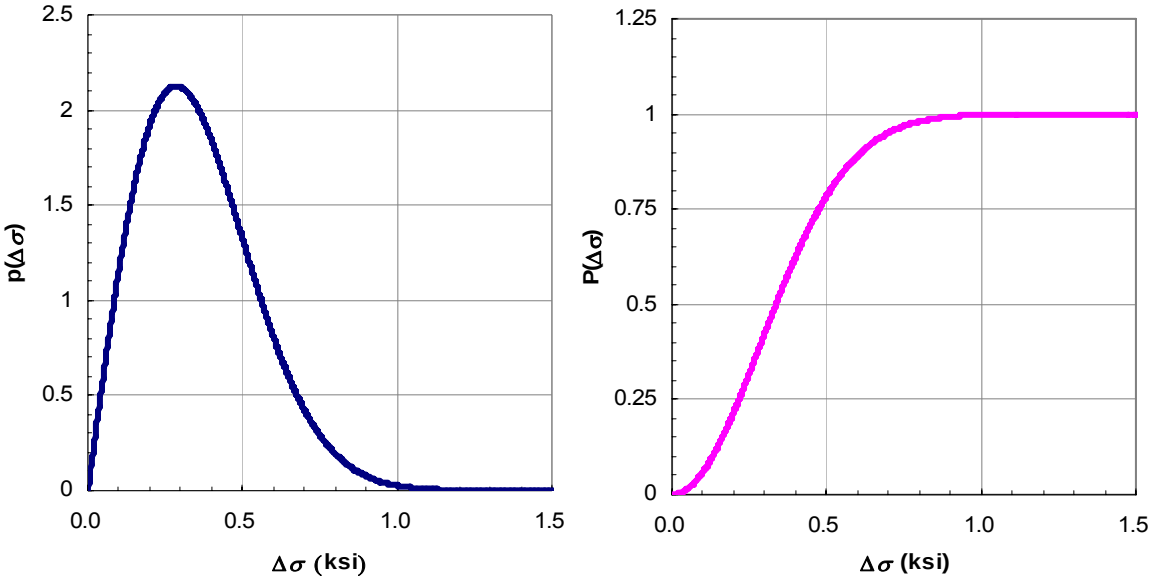

(a) (b)

Fig. 7. Rayleigh probability function. (a) probability density (b) cumulative probability.

Using the probability density, one can create a stress histogram where the number of cycles per unit time (e.g., year) for each small interval of stress range is displayed. When calculating the number of applied cycles (n_i) for each stress level, the probability of occurrence for the current sea state is taken into account as well as the period of the cycle.

Once n_i for every stress level is found, the cycles to failure (N_i) for each stress level needs to be decided. An S-N curve is used to obtain N_i's along with the constant life diagram if extrapolation is required. Due to the aforementioned simplifications and assumptions, S-N curves for uniaxial carbon-epoxy laminae can be utilized. S-N curves for composite materials under cyclic loading are usually represented in the following semi-log form.

$$S = a - b \log N \tag{16}$$

where S: maximum stress ($\sigma_{max} = \sigma_{mean} + \sigma_{amp}$) normalized by the static strength, a and b: material constants. Ideally, a is unity since $S = 1$ when the applied stress is equal to the static strength of the material. Sometimes N is replaced by $2N$ based on the idea that failure occurs at a half cycle when the amount of applied stress is identical to the static strength.

Numerous experimental S-N data sets are available in the literature, but the most of the data is obtained from more common stacking of laminates, such as angle-ply and quasi-isotropic laminates. These common lay-ups draw more interests because they are more generally and frequently used than uniaxial composites. In addition, these laminates with off-axis plies involve many damage mechanisms, while fatigue of uniaxial composites is extremely fiber-dominant and they generally show near-infinite fatigue lives. There are a limited number of S-N curves for unidirectional carbon-epoxy laminates [60,68,70-73] as shown in Fig. 8. Due to the differences in constituent materials and number of data points available for curve fitting, the curves are dispersed significantly. Since it is difficult to define a typical uniaxial S-N curve for carbon-epoxy, parameters a and b from Ref. [60], which is the most recent (1996) data of the nine S-N curves, are utilized for the estimation of the fatigue life. In addition, the degradation parameter b is replaced by larger values to study its effect on the predicted amount of damage and fatigue life. When normalizing the applied stress, the long term axial strength is used in order to achieve conservative results.

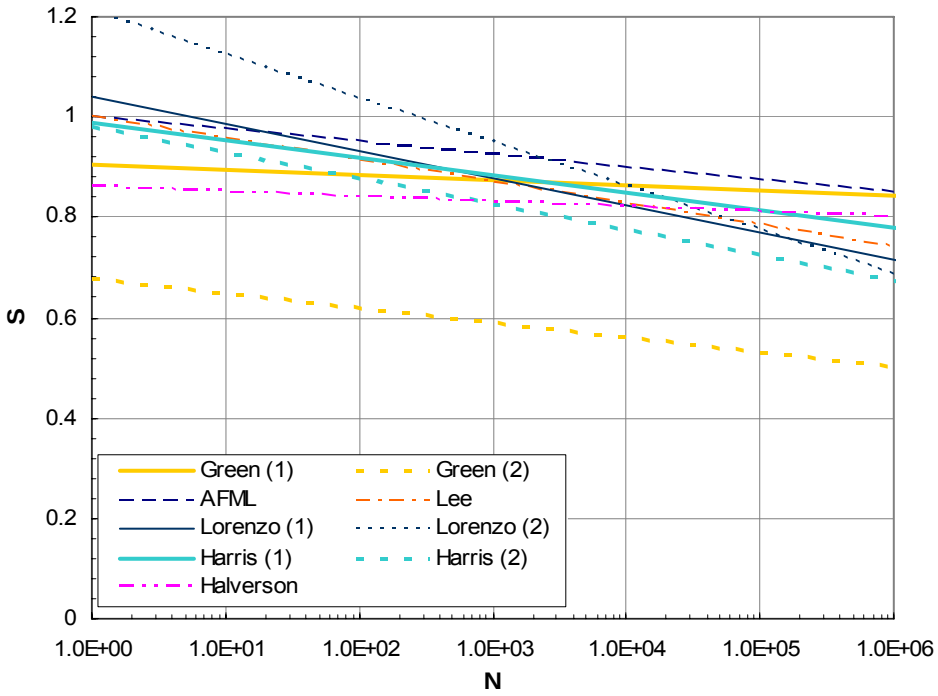

Fig. 8. S-N curves for unidirectional carbon-epoxy laminas.

When generating an S-N curve, the stress levels that are applied in the tests are identified with a specific stress ratio (also referred to as load ratio) R, which is defined as follows in terms of cyclic stress components in a lamina.

$$R = \frac{\sigma_{\min}}{\sigma_{\max}} = \frac{\sigma_{mean} - \sigma_{amp}}{\sigma_{mean} + \sigma_{amp}} \tag{17}$$

The most commonly used value of R is 0.1. In case where the stress cycles involve compressive stresses, a ratio of -1 is used. Cyclic stresses with identical σ_{amp} and different R ratios have different cycles to failure, which is often referred to as the mean stress effect. Traditionally, S-N curves for steel have represented stress range vs. cycles

to failure, and therefore higher mean stress is associated with acceleration of failure. However, since normalized maximum stress is commonly used for composites, using an S-N curve for higher mean value than the testing from which the curve is constructed does not always result in underestimation of fatigue damage. A cyclic stress whose R ratio does not have a corresponding S-N curve should be converted to an equivalent stress cycle whose R ratio matches an available S-N curve.

The conversion is performed using a constant fatigue life diagram, an example of which is shown in Fig. 9. In this diagram, a constant R appears as a straight line according to Eqn. (17). In this example, there are three constant R lines, each of which is associated with a distinct S-N curve. The segments of the constant life lines connect the points of the same fatigue life for which S-N curves are available, and more constant R lines give more accurate representation of constant life. All constant life lines converge onto the compressive and tensile static strengths on σ_{mean} axis, since loading is static when $\sigma_{\text{amp}} = 0$.

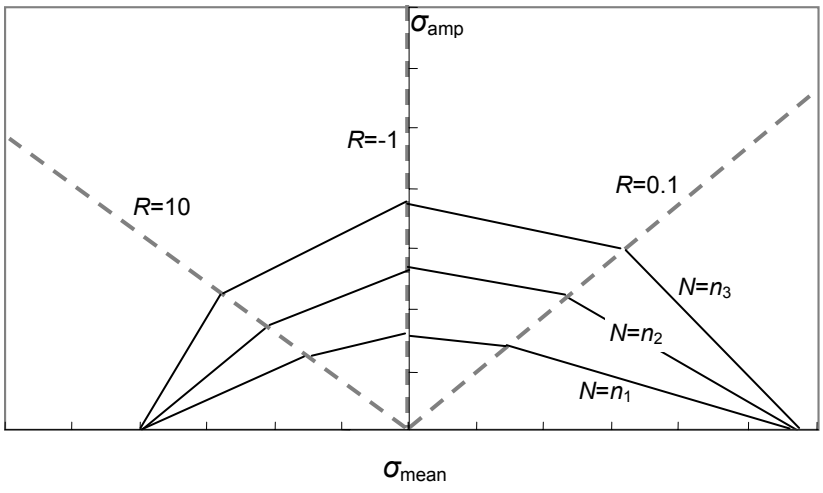

Fig. 9. Constant fatigue life diagram ($n_1 > n_2 > n_3$).

To further illustrate the stress extrapolation that is applied in the constant fatigue life diagram, $0.1 < R < 1$ region in Fig. 9 is redrawn in Fig. 10. For a given stress level represented by point b, the stress ratio $R = r$, and there is no experimental S-N data for this particular R ratio. Assuming that the S-N curve for $R = 0.1$ is available, the fatigue damage at point b is estimated through point b' on $R = 0.1$, which has the same fatigue life. The position of b' can be easily found by setting the ratio of the line segments, ab and bc to be equal to the ratio of a'b' to b'c'. Once the location of point b' is identified, the S-N curve for $R = 0.1$ is utilized along with σ_{mean} and σ_{amp} at this equivalent point to find the number of cycles to failure. Using σ_{max} of b without the extrapolation process would yield the cycles to failure at b'' where the constant σ_{max} line intersects the line that represents R = 0.1. For cyclic stresses with $0.1 < R < 1$, fatigue life would be underestimated without using the constant life diagram.

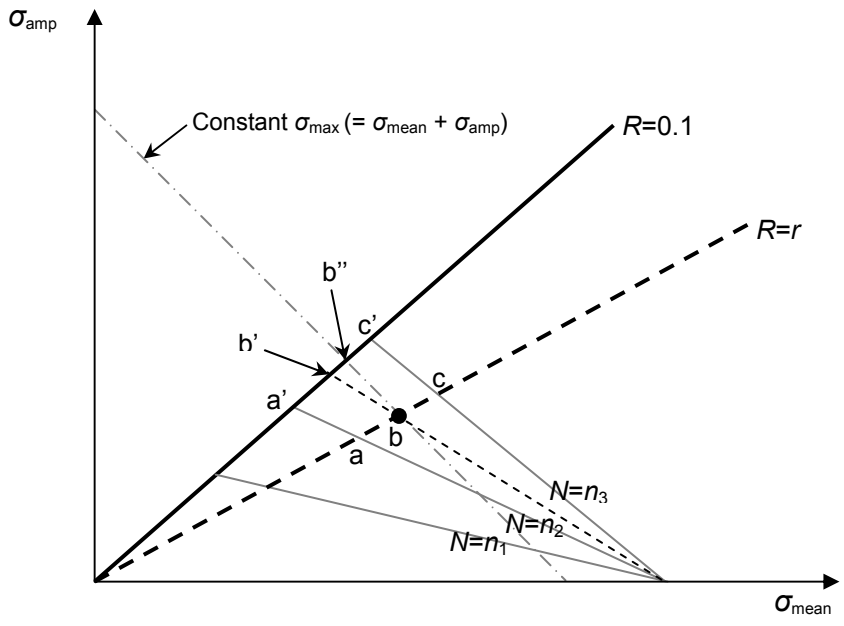

Fig. 10. Extrapolation of fatigue life using constant life diagram.

Ref [74] proposed the use of the following non-dimensional scalar quantity to take the mean stress effect into account, based on the observation that S-N curves for different R ratios can collapse into a master curve if the scalar quantity replaces the commonly used normalized maximum stress.

$$\Psi = \frac{\sigma_{amp}}{\sigma_B - \sigma_{mean}} \tag{18}$$

The S-N relationship used in this work is in the form of a power law relationship, which appears as a straight line on a log-log graph.

$$2N = \frac{1}{(\Sigma^*)^{n^*}} \tag{19}$$

where Σ^* is effective stress based on Tsai-Hill criterion and is a modified form of Ψ for complex state of stress. According to this work, the value of the exponent n^* is 11.9 for carbon-epoxy. In addition to the semi-log type S-N data, Eqn. (19) is used for calculating fatigue damage and life. Again, a parametric study with varying n^* is performed.

After obtaining N_i's for each stress level from the histograms, damage caused by individual stress levels needs to be estimated, and eventually total damage induced by all the sea states are calculated. Most of the fatigue models incorporating multiple loading cycles with various magnitudes are not readily applicable to estimating wave fatigue of the riser, since wave loading, due to its random nature, cannot be approximated as multiple blocks of constant amplitude loading with a known sequence. Although loading sequence does influence the development of fatigue damage in composites, the random nature of wave does not permit establishing a definitive time history of wave loading. For this reason, Miner's rule, which does not reflect the effect of loading sequence, is

used in this study to estimate fatigue damage from a long term sea state. Miner's rule is a linear cumulative damage theory and can be expressed as follows.

$$D = \sum_i \frac{n_i}{N_i} \tag{20}$$

where D: damage, n_i: number of cycles applied at i-th stress level, and N_i: cycles to failure at i-th stress level. The number of cycles to failure at a specific stress level can be found using S-N curves. For design purposes, it is typically assumed that fatigue failure occurs when $D = 1$. This procedure is performed for all short term sea states and finally the total damage per unit time is obtained by summing up the damage values of the individual sea states. Expected fatigue life is obtained simply by inverting the total damage.

In addition to evaluating fatigue damage of the composite body, fatigue assessment of the steel liner is carried out. Although carrying mechanical loads is not an intended function of the liner, it is inevitable in the current design that part of the loads is transferred from the end fittings to the liner. The circumferential welds that connect the liner and end fittings of a riser joint are considered to be a potential fatigue failure location. Generally, welded joints have poor fatigue performance to some extent, depending on the quality of welding. To assess fatigue damage of the welds, two S-N curves are utilized: DNV-C and DNV-E [75]. The C curve is used for welds that are dressed flush, and the E curve is for welds made at site and not machined. These curves are represented by power law relationships and plotted on a log-log scale. It should be mentioned that they are design curves, not failure curves; they are associated with 97.6 % probability of survival by shifting down from the mean by twice the standard deviation. When using the design curves, mean stress effect is usually not taken into account since the curves are already reduced and provide a certain extent of conservativeness.

3.4. Damping and resonant response

Composite materials are known to have excellent damping properties, which are primarily attributed to the viscoelastic nature of the matrix material. It is expected that composite risers possess superior damping and that they will suffer less from vibrations caused by sea water than steel risers do. In this study, the damping of the composite riser is estimated using the ratio of energy dissipated to energy stored. Then simulations are carried out where the top of the riser is excited in still water at its natural frequencies, and the effect of material damping is evaluated.

3.4.1. Damping

Damping of composites is a complex phenomenon, there being multiple sources of energy dissipation within the material, such as viscoelastic nature of constituent materials, interphase, damage, etc. [76]. There are two major approaches for the prediction of damping of composite materials: complex moduli [77-81] and strain energy method [82-86]. The complex moduli approach is based on the elastic-viscoelastic correspondence principle, and the real and imaginary parts of a complex modulus (E^*) represent the storage modulus (E') and loss modulus (E''), respectively. The ratio between the loss modulus and the storage modulus is referred to as loss factor, η.

$$\eta = \frac{E''}{E'} \tag{21}$$

Therefore, complex modulus can be expressed as the following equation.

$$E^* = E' + iE'' = E'(1 + i\eta) \tag{22}$$

Strain energy method is based on the fact that damping of a material can be

characterized by the ratio between the dissipated energy (ΔU) and the stored energy (U); this ratio is called specific damping capacity, ψ.

$$\psi = \frac{\Delta U}{U} \tag{23}$$

In a composite lamina, the dissipated energy is separated into three components, assuming energy dissipation in the out-of-plane directions is negligible. In k-th layer, the total dissipated energy is,

$$\Delta U^{(k)} = \Delta U_1{}^{(k)} + \Delta U_2{}^{(k)} + \Delta U_{12}{}^{(k)} \tag{24}$$

From the definition of ψ and U, the energy dissipation in 1-direction is

$$\Delta U_1{}^{(k)} = \frac{1}{2}\int_{\Omega}\int_{h_{k-1}}^{h_k} \psi_1 \sigma_1 \varepsilon_1 dz d\Omega \tag{25}$$

Then the total dissipated energy of the laminate is

$$\Delta U = \frac{1}{2}\int_{v} \{\varepsilon_{ij}\}^T [\Psi] \{\sigma_{ij}\} dV \tag{26}$$

where [Ψ]: diagonal matrix consisting of ψ_1, ψ_2, and ψ_{12}.

The previously introduced measures of damping have the following relationships with other common measures.

$$\psi = 2\pi\eta = 2\pi\frac{\omega_2 - \omega_1}{\omega_0} = \frac{2\pi}{Q} \approx 4\pi\zeta \approx 2\delta \tag{27}$$

where ω_1 and ω_2: frequencies on either side of resonant frequency for which the

amplitude is $1/\sqrt{2}$ times the resonant amplitude, ω_0: natural frequency, Q: dynamic amplification factor, ζ : fraction of critical damping (damping ratio), and δ : logarithmic decrement.

Efforts have been made towards obtaining loss factors or specific damping capacities of unidirectional laminae for various fiber volume fractions, either experimentally or numerically based on constituent properties [82,83,86-88]. In this study, the damping properties of carbon-epoxy composites from Refs [83,86] are utilized to estimate the range of damping that the composite riser can provide. Table 12 presents the specific damping capacities in the local lamina directions.

Table 12

Lamina damping properties

Ref [86]			**Ref [83]***		
ψ_1 (%)	ψ_2 (%)	ψ_{12} (%)	ψ_1 (%)	ψ_2 (%)	ψ_{12} (%)
0.45	4.22	7.05	0.98	10.64	8.00

* original values in loss factors

To calculate the damping of the composite riser, multiple sets of arbitrary loads are applied to the 10-ft local finite element model. The calculation of energy dissipation given by Eqn. (26) is performed through a user material subroutine where the lamina specific damping capacities are specified. Dissipated energy is calculated at every integration point of each element, and the total dissipated energy of the model is divided by the total strain energy to obtain the specific damping capacity of the riser.

In general, damping of a material system or structure is estimated through

responses. Unfortunately, there are not many practical data on riser damping reported in the literature. Damping is often ignored or assumed, usually as 0.3% of critical damping or 2% logarithmic decrement for steel risers [89,90], although there is no known basis for the assumption. In Ref [91] as much as 5% damping ratio is assumed. According to Ref [89], damping of steel risers can be much lower than the commonly used value. Speculations on damping of composite risers reflect great expectations and show a wide range of values. A VIV study of a composite top tensioned riser in Ref [92] made an estimation of 1.5% damping ratio, which was claimed to be conservative. In Ref [90] damping of a composite riser was assumed to be 5% in logarithmic decrement, which amounts to about 0.80% in damping ratio. Experimental data from Ref [93] report up to 2.3% of damping ratio for a large diameter composite tube.

When incorporating damping into structural analyses, the most general method is to use regard the damping as viscous damping. Although in many cases the actual damping phenomena are not viscous but viscoelastic or hysteretic, equivalent viscous damping is used due to the mathematical simplicity. Oftentimes, for minimal computational expenses, Rayleigh proportional damping is used. In ABAQUS, material damping is defined in terms of two coefficients in Rayleigh damping: mass proportional and stiffness proportional damping coefficients. The damping matrix then becomes a linear combination of mass and stiffness matrices. Damping ratio for *i*-th mode can be expressed as,

$$\zeta_i = \frac{a}{2\omega_i} + \frac{b\omega_i}{2} \tag{28}$$

where *a*: mass proportional coefficient and *b*: stiffness proportional coefficient. Mass proportional damping damps lower frequencies, while stiffness proportional damping damps higher frequencies.

The coefficients *a* and *b* are determined from actual response of the structure when two different natural modes are excited. Since it is impossible to perform such tests,

either entirely mass proportional or stiffness proportional damping is used in this study. When analyzing offshore structures, mass proportional damping is normally neglected, and a value of b that gives a realistic damping at the dominating wave frequency is used [94]. In this study, this common practice is verified by frequency sweep analyses of simple steel and composite beams. Either mass proportional or stiffness proportional damping is specified in steady state dynamic analyses, and the response of the structure near its natural frequency is examined to find ω_1 and ω_2 in Eqn. (27). Then it can be determined which proportional damping gives the response associated with the intended damping ratio.

3.4.2. Excitation

In this section, vibration responses of the composite riser with and without damping are studied. Through a series of direct integration dynamic finite element analyses, the effect of damping on vibration amplitudes of the riser is evaluated. The analyses are intended to simulate simple tests where the top of the riser is subject to sinusoidal excitation at natural frequencies of the riser. In addition to in-line (direction of free stream or top excitation) responses, transverse (perpendicular to the free stream) responses are also studied.

Vibration of a riser is an extremely complicated phenomenon due to the interaction between the structure and sea water. Sea wave exerts fluid drag on the structure, and the structure alters the flow pattern around the structure itself. The resulting effect is swirling vortices, which oftentimes cause vortex-induced vibration (VIV) [55] in the transverse direction. The vortex pattern is a function of Reynolds number. The most significant effect of VIV is lock-in or synchronization. As the vortex shedding frequency (or its multiple or submultiple) approaches the natural frequency of a structure, the shedding frequency becomes equal to the natural frequency. As a result, the vibration amplitude of the structure increases substantially. Also, the transverse vibration increases the drag on the structure.

It is computationally intense to incorporate fluid-structure interaction faithfully into a structural analysis. A number of models to represent VIV have been proposed, and the simplest model is linear harmonic model. Based on the fact that vortex shedding is a more or less sinusoidal process, the model represents the transverse lift force (f_L) as a function of shedding frequency (ω_s).

$$f_L = \frac{1}{2}\rho u^2 D C_L \sin(\omega_s t) \tag{29}$$

The above equation is very similar to the drag force term in Eqn. (11), and the coefficient C_L is referred to as lift coefficient. Lift coefficient is dependent upon Reynolds number and vibration amplitude. It is known that vibration amplitude do not exceed 1.5 diameters since large vibration produces unstable vortex pattern and causes the lift coefficient to diminish significantly [55].

Analytical solutions for vibrations of beams are available in many cases. The equation of motion for risers in Eqn. (10) contains terms associated with axial tension and weight in addition to the basic beam equation. Ref [95] proposed a simplified solution technique to obtain modal vibration characteristics of hinged-hinged risers, where both weight and tension are taken into account. However, since a riser string consists of multiple types of joints with different geometry and material, one must resort to a numerical method such as finite element technique to obtain accurate results. In this study, mode shapes and natural frequencies of the composite riser are obtained through a finite element analysis. The finite element model is same as the one used in Section 3.2. Added mass effect is included in the analysis with $C_M = 2.0$.

After the natural frequencies are extracted, modes near the peak periods of the storm conditions (Table 9) are selected. The selected natural frequencies are used as the excitation frequencies in the subsequent vibration analyses with top oscillation. The top oscillation is applied at 6080 ft above the sea floor, where the riser centralizer is located. The forcing function is sinusoidal with an amplitude of 10 ksi. Fluid drag in situations involving wave and/or current is one of the major sources of excitation. On the contrary,

in this scenario where the riser oscillates in still water, drag resists the motion of the structure and weakens the vibration. For this reason, a smaller value of drag coefficient gives more conservative results in this particular case, and a drag coefficient of 0.7 is assumed.

Transverse lift force in global y-direction is applied using a user element subroutine. User-defined elements can be used to apply forces to a node as a function of displacement or velocity at another node. Since transverse lift is a function of in-line relative velocity (fluid velocity relative to structure or vice versa), a user element subroutine can be constructed to calculate and apply transverse lift at each node. For the riser oscillating in still water, Eqn. (29) can be modified as follows.

$$f_L(y) = \frac{1}{2}\rho \frac{\partial x}{\partial t}\left|\frac{\partial x}{\partial t}\right| DC_L \tag{30}$$

In this study, upon the B31H beams (3-D, 6 degrees of freedom version of B21H used in Section 3.2) that constitute the riser, as many user elements are superimposed sharing all the nodes. The user elements have negligible mass and stiffness in order to apply transverse nodal forces without altering the structure.

4. RESULTS

4.1. Pressure loads

In this section, performance of the composite riser under either internal or external pressure is evaluated. Layer-by-layer stresses under the design internal pressure (10 ksi) are presented, and burst capacity of the riser is decided through a failure analysis. To evaluate the performance of the composite riser under external pressure, eigenvalue buckling analyses are performed for rough estimates of overall collapse. Local plastic collapse of the steel liner is analyzed through continuous response analyses. The effects of partial debonding at composite / liner interface and geometrical imperfection, i.e., out-of-roundness, on collapse are investigated.

4.1.1. Burst

The main stresses to be discussed in this section are Von Mises stress in the steel liner (σ_{liner}), fiber direction in the hoop layers (σ_1^{hoop}), and in-plane transverse direction in the axial layers (σ_2^{axial}). Through-thickness normal (σ_3) in the composite body is important since, if neglected, it impairs the accuracy of the hoop stress evaluation. However, the regarding failure, it does not require special attention since its magnitude is smaller than σ_2^{axial} and the transverse normal strength in compression is far greater than the tensile strength.

The analytical procedure presented in Eqn. (1) through (9) in Section 3.1 is applied to evaluate the hoop stresses in the liner and layer 1 under an internal pressure of 100 psi. The radial displacement of the liner at the interface is

$$u_r^{liner}(r_{\text{int}}) = 3.23\times10^{-4} - 3.35\times10^{-6}\, p_{\text{int}} \tag{31}$$

The solution for Eqn. (9) is

$$\sigma_r = 0.00729 p_{\text{int}} r^{2.488} - 2150 p_{\text{int}} r^{-4.488} \tag{32}$$

Then the radial displacement on the composite side is

$$u_r^{comp}(r_{\text{int}}) = 2.91 \times 10^{-6} p_{\text{int}} \tag{33}$$

The continuity of the radial displacement at the liner-composite interface leads to p_{int} = 51.6 psi. The resulting hoop stress in the mid-surface of the liner is 889 psi. A good agreement is shown between the analytical solution and the finite element solution whose prediction is approximately 882 psi. Next, layer 1 is separated from the composite body, and the interfacial pressure between layer 1 and the rest of the composite body is found to be 42.7 psi. The hoop stress of layer 1, which is equivalent to a thin pipe subjected to internal and external pressures of 51.6 psi and 42.7 psi, is 517 psi, whereas the finite element solution is 521 psi.

Under 10 ksi internal pressure, Von Mises stress at the mid-wall of the steel liner is 80.0 ksi, and the liner starts to yield at this point. The major stresses in the composite body are presented in Fig. 11. The major stresses in the composite body are greater in the inner layers and diminish as moving outwards. The stresses in the hoop layers are less than 25.5 % of its long term allowable. In the innermost axial layer, transverse normal stress reaches 48.4 % of its long term allowable.

As the internal pressure is increased further with an increment of 1 ksi, the composite body experiences additional stresses due to the yielding of the liner. At p_i = 16 ksi, first matrix cracking occurs in layer 2, and at p_i = 19 ksi all the axial layers undergo matrix cracking. Finally, when p_i = 26 ksi fiber fracture occurs in layer 1. Fig. 12 shows the growth of σ_2 in layer 2 and σ_1 in layer 1 with increasing p_i. Additional stresses on the hoop layers resulting from matrix cracking in the axial layers are not substantial and hence irrecognizable in the figure.

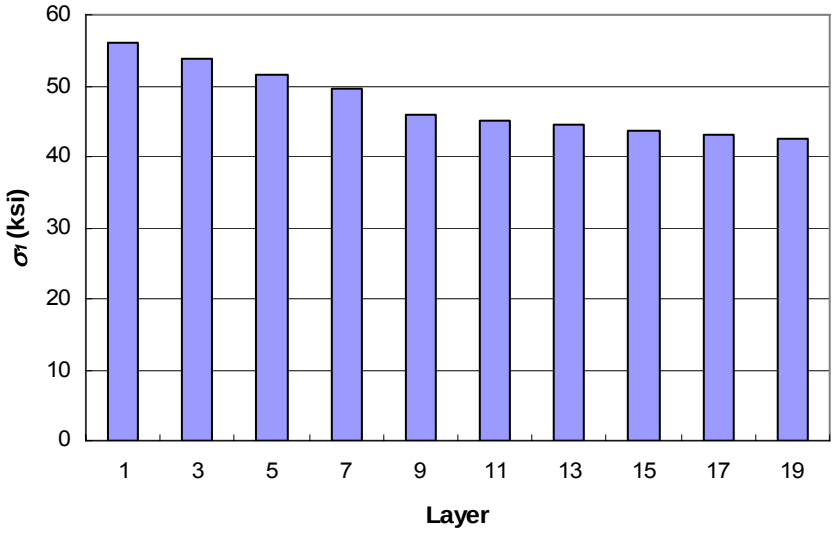

(a)

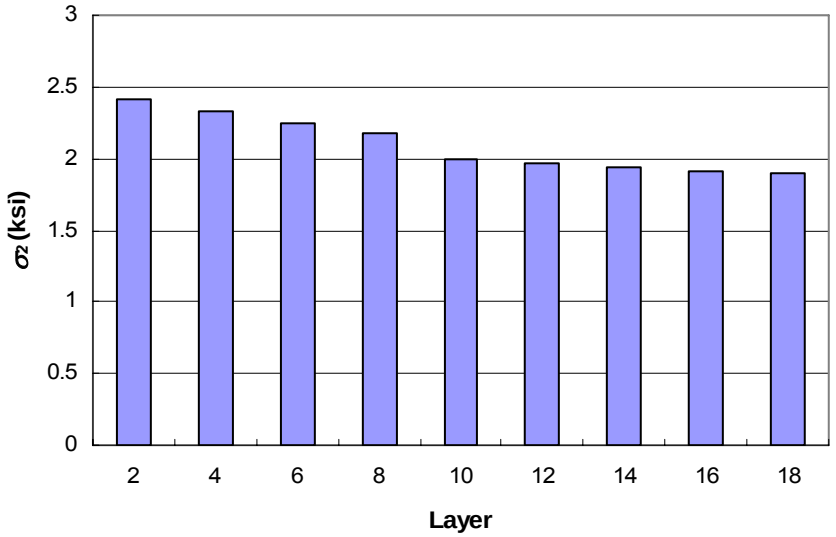

(b)

Fig. 11. Stresses in composite layers under p_i = 10 ksi. (a) σ_1^{hoop} (b) σ_2^{axial}.

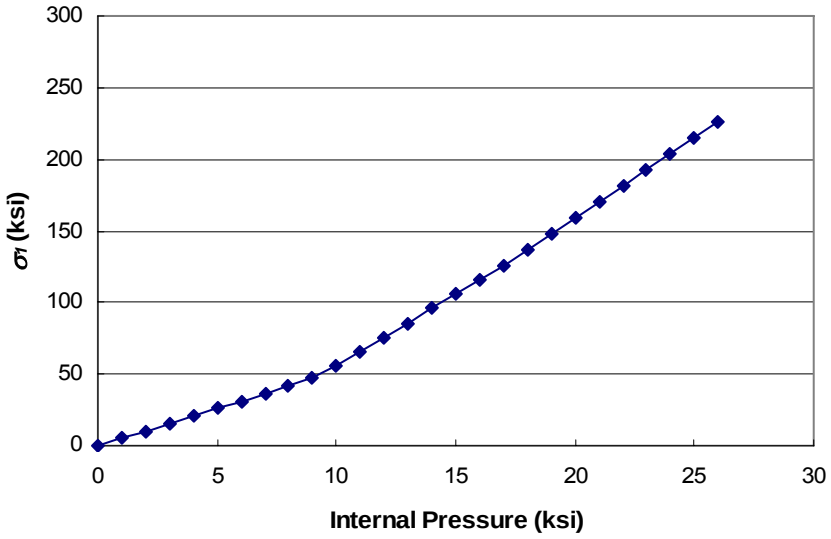

(a)

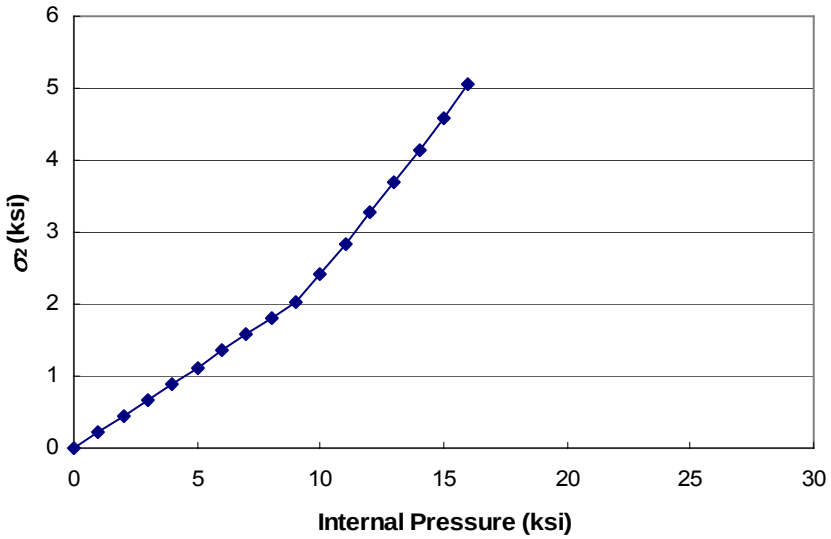

(b)

Fig. 12. Stresses vs. incremental internal pressure. (a) σ_1 in layer 1 (b) σ_2 in layer 2.

4.1.2. Collapse

4.1.2.1. Eigenvalue buckling analysis

To investigate the effect of model length on buckling pressures, 12 perfectly bonded cylinders of different lengths, from 10 in to 120 in, are analyzed. The results show that not only the buckling pressures but also the mode shapes are dependent on the length of the model. Table 13 presents mode shapes of the first three modes in terms of *m*, number of circumferential waves, and *n*, number of half waves along the axial direction. Examples of mode shapes are presented in Fig. 13.

Table 13
Influence of model length on mode shapes

length (in)	**Mode 1**		**Mode 2**		**Mode 3**	
	m	**n**	**m**	**n**	**m**	**n**
10	4	1	3	1	5	1
20	2	1	3	1	4	1
30	2	1	3	1	3	2
40	2	1	3	1	2	2
50	2	1	2	2	3	1
60	2	1	2	2	3	1
70	2	1	2	2	2	3
80	2	1	2	2	2	3
90	2	1	2	2	2	3
100	2	1	2	2	2	3
110	2	1	2	2	2	3
120	2	1	2	2	2	3

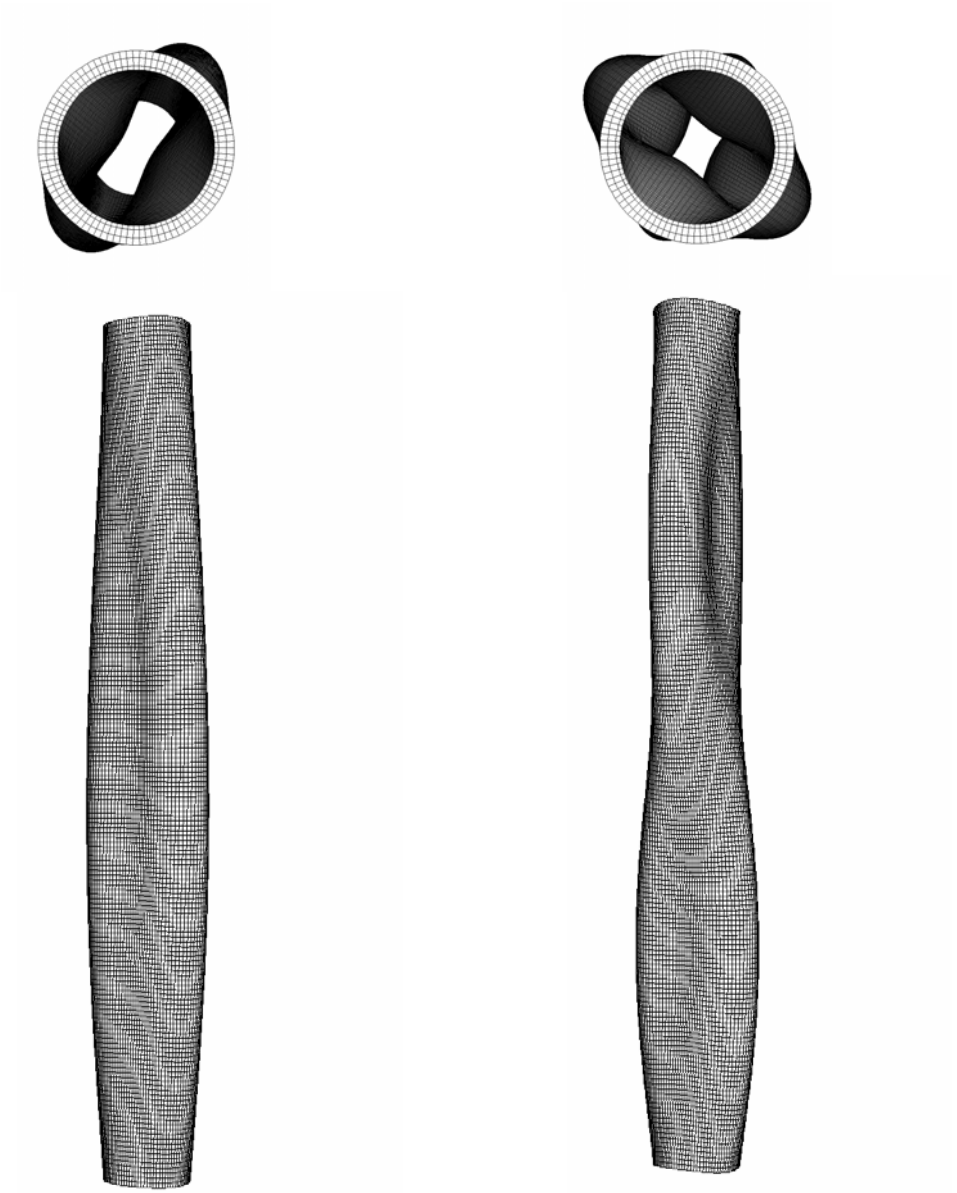

(a) (b)

Fig. 13. Mode shapes (l = 120 in). (a) 1st mode (m=2, n=1) (b) 2nd mode (m=2, n=2).

Fig. 14 shows the convergence of buckling pressures. The critical buckling pressure shows a good convergence at l = 70 in, and the length dependence is eliminated at l = 120 in. Therefore, subsequent studies are performed through 120-in models.

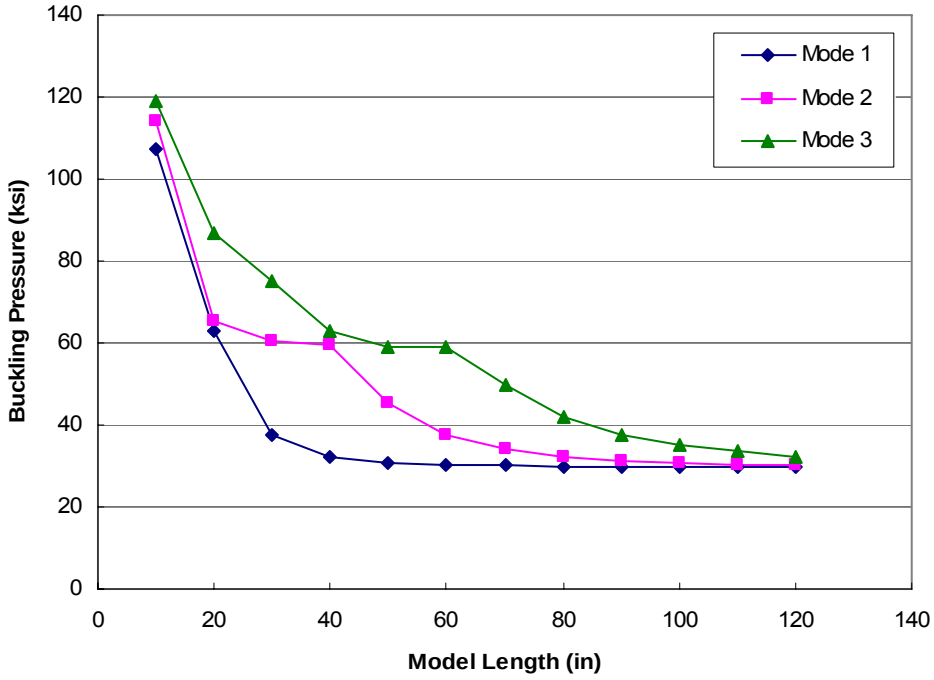

Fig. 14. Length dependence of buckling pressures.

Effects of element choice and mesh refinement on the critical pressure are summarized in Table 14. The C3D8 linear element does not show any effect of shear locking, and there are no notable differences among the results.

Table 14

Critical pressures from various element choices and meshes

Element	Mesh (long/circum)	P_{cr} (ksi)
C3D8	180 / 90	29.805
	240 / 120	29.44
C3D8R	180 / 90	29.208
C3D8I	180 / 90	30.209
C3D20	90 / 45	29.828
	180 / 90	29.802

Ovalization of the riser cross-section, where the inner radius is decreased in one direction and increased in the perpendicular direction, does not cause significant reduction in the buckling capacity. When the riser is ovalized by 1% of its inner radius, with the shorter and longer radii of 4.8114 and 4.9086 in respectively, the critical pressure was 29.784 ksi. Doubling the ovalization does not have a notable effect either, with the critical pressure being 29.722 ksi.

To investigate the effect of debond, ten debond geometries for each debond type are created. For the through-circumference debonds, the debond length (l_{debond}) is varied from 10 to 100 in with an increment of 10 in. For the through-length debonds, the debond arc angle (θ_{debond}) is increased by 30°. Examples of buckled shapes of the riser section with various debond geometries are presented in Fig. 15 and 16. For a through-circumference type debond, the shape is similar to the completely bonded case, except buckling is confined within the debond area. The cross-sectional shape for a buckled riser section with a through-length type debond is dependent on the arc angle of the debond region, θ_{debond}. For a small or large θ_{debond}, the shape is identical with the completely bonded case, while an intermediate debond area causes the riser to be crushed only on the side where the debond exists.

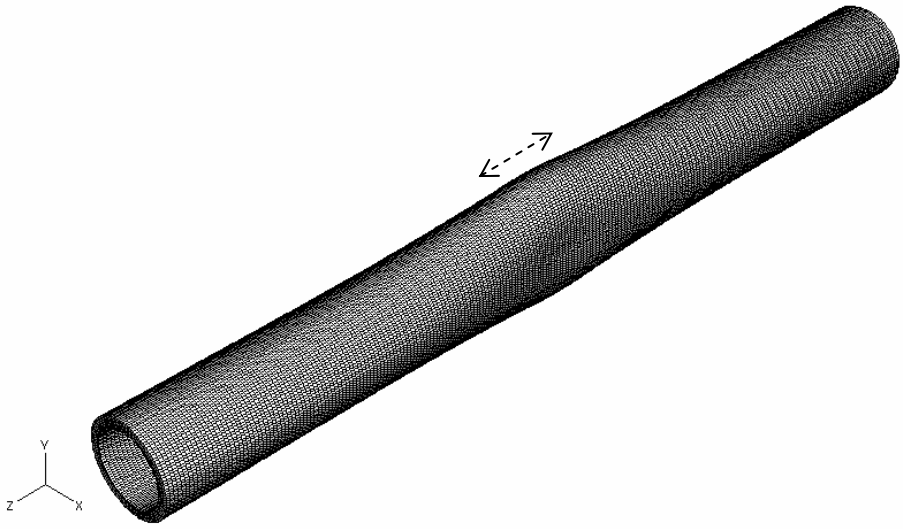

(a)

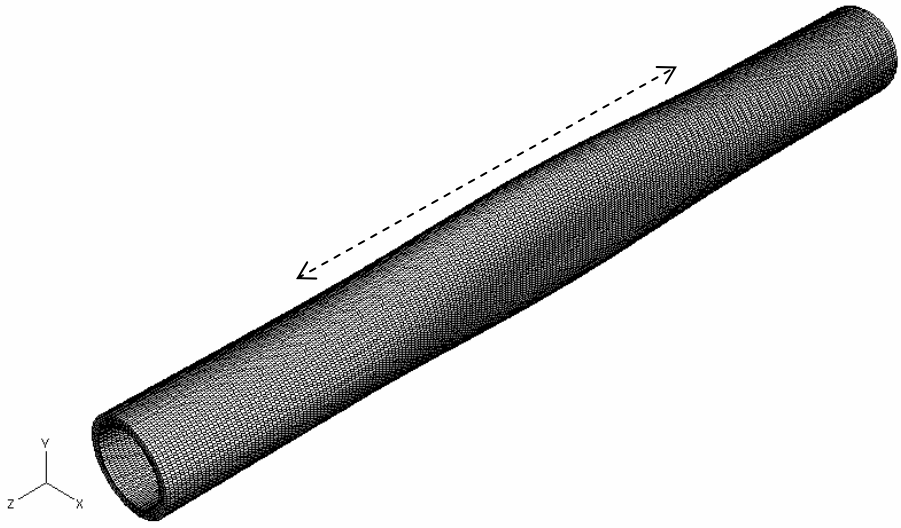

(b)

Fig. 15. Buckled shapes of cylinders with through-circumference debonds. (a) l_{debond} = 10 in (b) l_{debond} = 60 in.

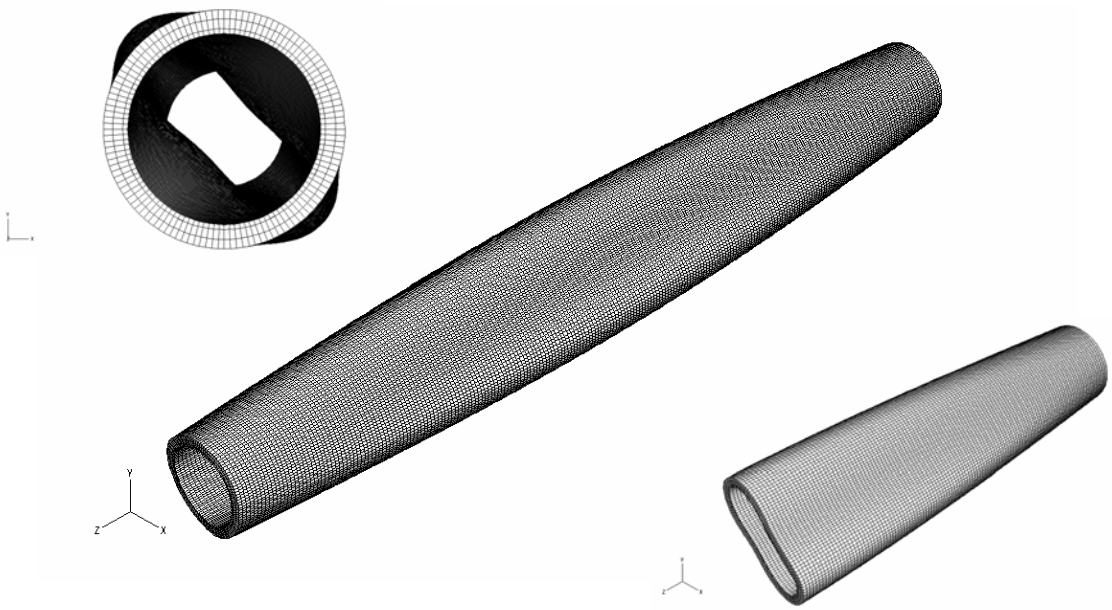

(a)

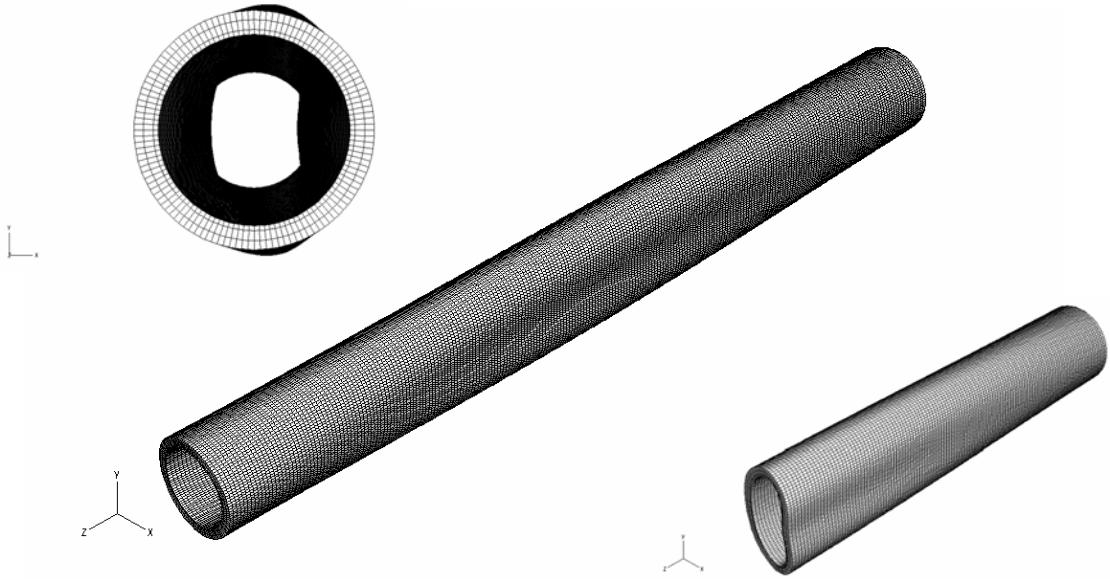

(b)

Fig. 16. Buckled shapes of cylinders with through-length debonds. (a) $\theta_{\text{debond}} = 30°$ (b) $\theta_{\text{debond}} = 180°$.

Fig. 17 shows the decrease of critical buckling pressure as debond area is expanded. Through-circumference type debonds have more significant undermining effects, and for both debond types, decreases in buckling capacity occur more rapidly for smaller debond areas.

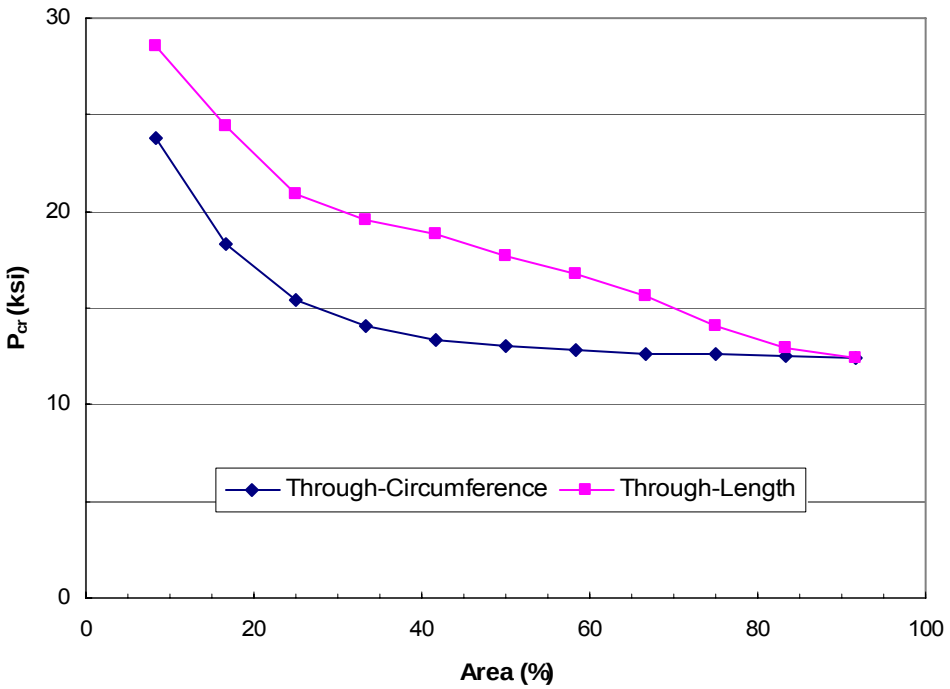

Fig. 17. Critical pressure vs. debond geometry.

In the case where the liner is completely unbonded, the critical pressure becomes 12.806 ksi. Again, ovalization does not cause significant decline in the critical pressure: 12.770 ksi for 1% ovalization and 12.661 ksi for 2%. With the absence of the internal liner, the composite body buckles at 11.7 ksi of external pressure.

4.1.2.2. Continuous response analysis – Liner collapse

When the steel internal liner is exposed to increasing hydrostatic pressure without being surrounded by the composite body, it buckles at less than 1 ksi. However, when a liner is confined in a thick and stiff body, the liner can resist a significantly higher external pressure before it collapses. First, the 1st buckling mode shape is superposed upon the perfect cylinder in order for the deformation of the liner to conform to the buckling mode shape. Then incremental pressure is applied on the debond surfaces and the exterior of the riser. The superposed mode shape is scaled so that the largest perturbation (Δr_{max}) is 1% and 10% of the liner thickness (case (a) and (b)). In the next two cases, the cross-section is ovalized in the same ways as the previous section, to investigate the effect of severe out-of-roundness: 1% and 2% with respect to the inner radius (case (d) and (e)). In addition, mode superposition with Δr_{max} of 0.0486 in (case (c)) is performed to compare its collapse behavior with the ovalized riser with the same maximum perturbation value (case (d)). Table 15 summarizes the five cases of geometrical imperfections considered.

Table 15
Applied geometrical imperfections

Case	Type	Δr_{max}	Note
(a)	mode superposition	0.0025	1% liner thickness
(b)	mode superposition	0.025	10% liner thickness
(c)	mode superposition	0.0486	1% inner radius
(d)	ovalization	0.0486	1% inner radius
(e)	ovalization	0.0972	2% inner radius

Fig. 18 shows the maxima of von Mises stress in the riser section with the various geometric imperfections. While buckling of the entire riser section is hardly affected by ovalization regardless of the bonding of the liner, liner collapse shows high sensitivity due to its small thickness. Collapse does not begin immediately after local yielding takes place, and maximum stress stays near the yield strength for additional 300 to 500 psi of internal pressure. Case (e), where Δr_{max} is the largest, shows that yielding, as well as collapse, is significantly accelerated. The curves for case (c) and (d) before collapse are very close to each other, but collapse occurs slightly faster in case (c). The maximum gap (δ_{max}) between the liner and composite body expands in the same manner as the development of the maximum stress, as shown in Fig. 19. Therefore, either may be used as an indicator of collapse. Examples of deformed liner upon yielding, upon failure, and after failure are presented in Fig. 20 and 21. The range for the stress contours is from the yield strength to the ultimate strength, and hence black areas indicate occurrence of failure.

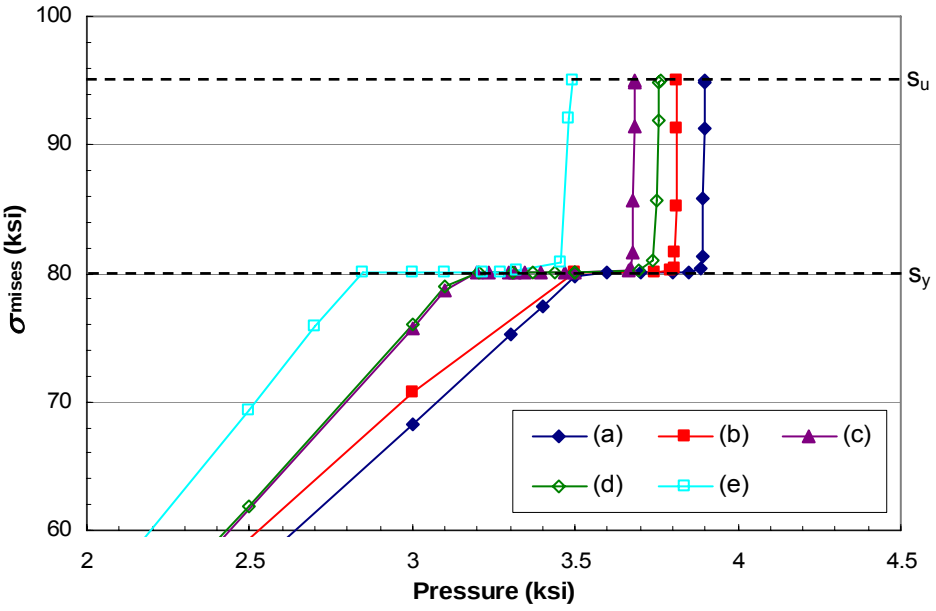

Fig. 18. Maximum von Mises stresses in unbonded liner.

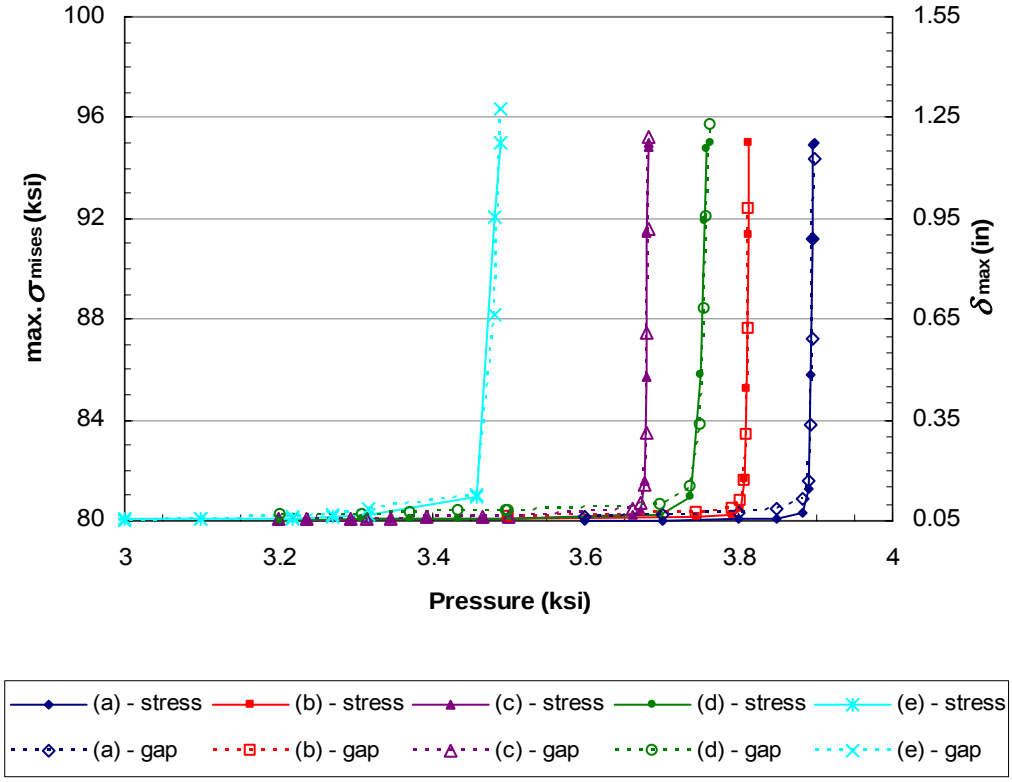

Fig. 19. Growth of maximum stress and maximum gap for unbonded liner.

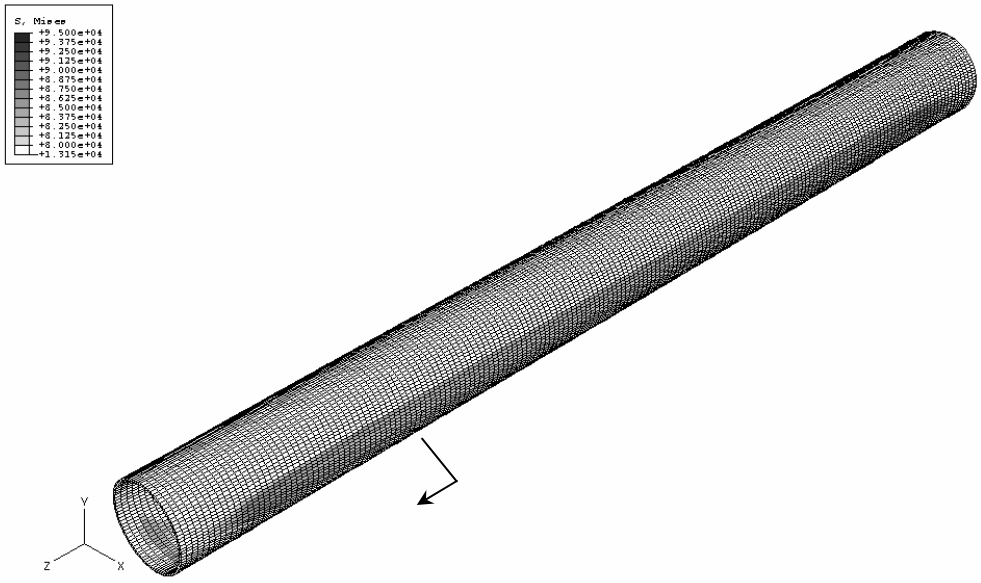

(a)

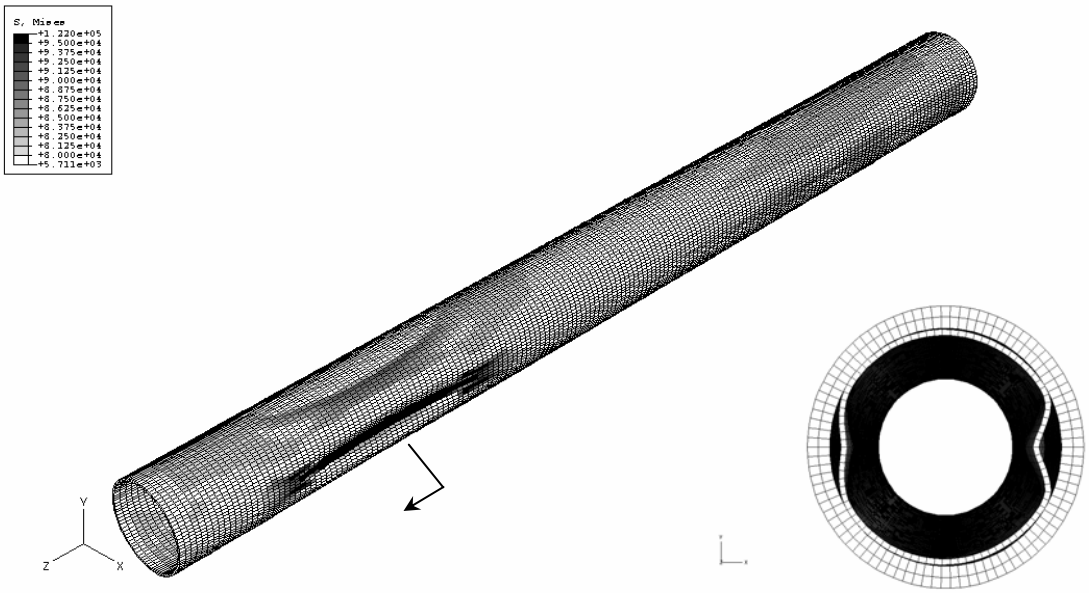

(b)

Fig. 20. Progression of liner collapse in case (d). (a) p = 3.5 ksi, δ_{max} = 0.0825 in (b) p = 3.7627 ksi, δ_{max} = 1.228 in.

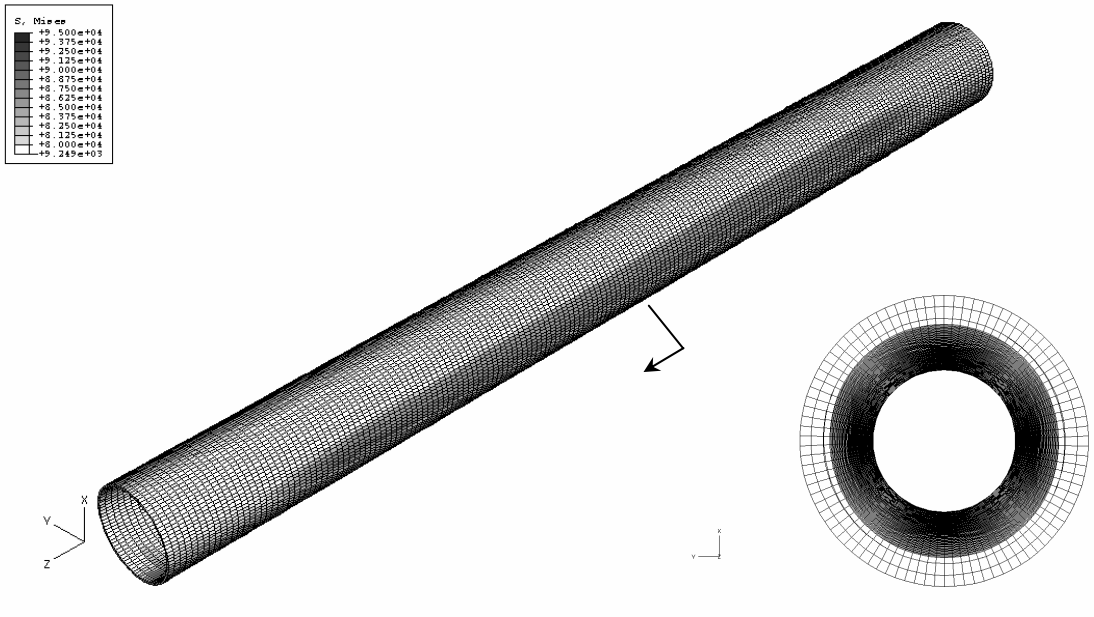

(a)

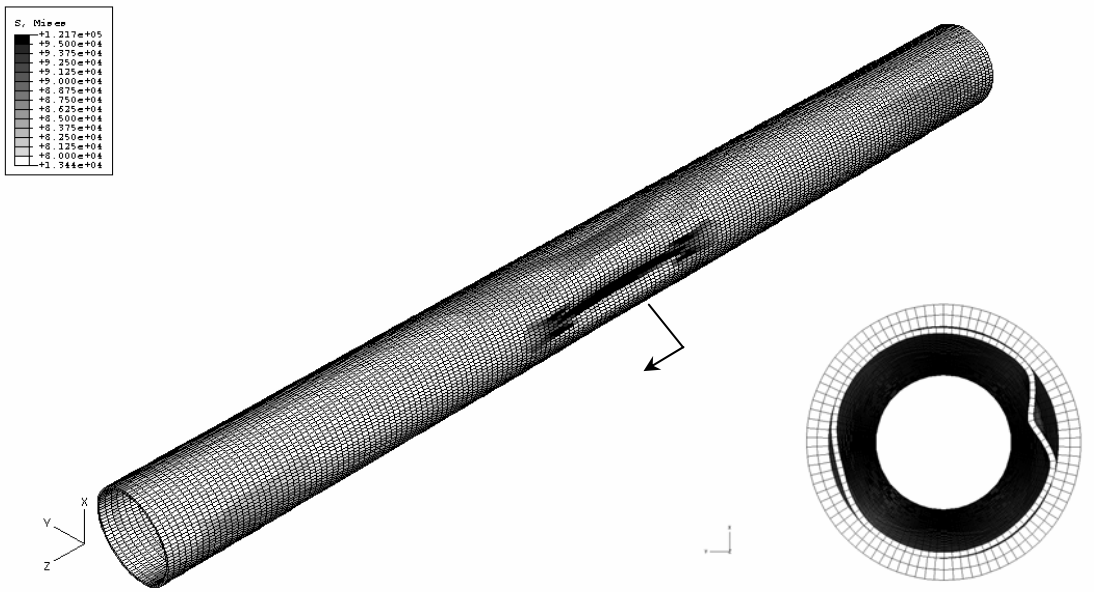

(b)

Fig. 21. Progression of liner collapse in case (b). (a) p = 3.5 ksi, δ_{max} = 0.0593 in (b) p = 3.8135 ksi, δ_{max} = 0.977 in.

The effect of partial debonding on liner collapse is investigated in a parametric manner with varying geometric parameters, as was done in the previous section. No initial geometric imperfection is incorporated in this set of analyses. The debond length for the through-circumference type is increased by 20 in, and an increment of 40° debond arc angle is used for the through-length type.

Fig. 22 shows the load vs. maximum stress curves for the through-circumference debonds. With this type of debonds, the liner yields at 4.1 ksi of interfacial pressure regardless of the length of debond region. However, the collapse pressures do depend on the debond length, ranging from 4.8 to 5.0 ksi. Relatively short debond lengths (20 and 40 in) show slightly higher collapse resistance, and maximum stresses at collapse are higher. The collapse pressure then decreases as the debond region is extended. Interestingly, when the debond length is 100 inches, the collapse pressure increases back, close to small debond cases. Fig. 23 shows the growth of δ_{max} through incremental pressure, and the cross-sectional deformation for the 60-inch case is presented as an example. Again, the expansion of the maximum gap shows the same trend as the maximum stress curve. Fig. 24 presents stress contours which show failure areas for two example cases.

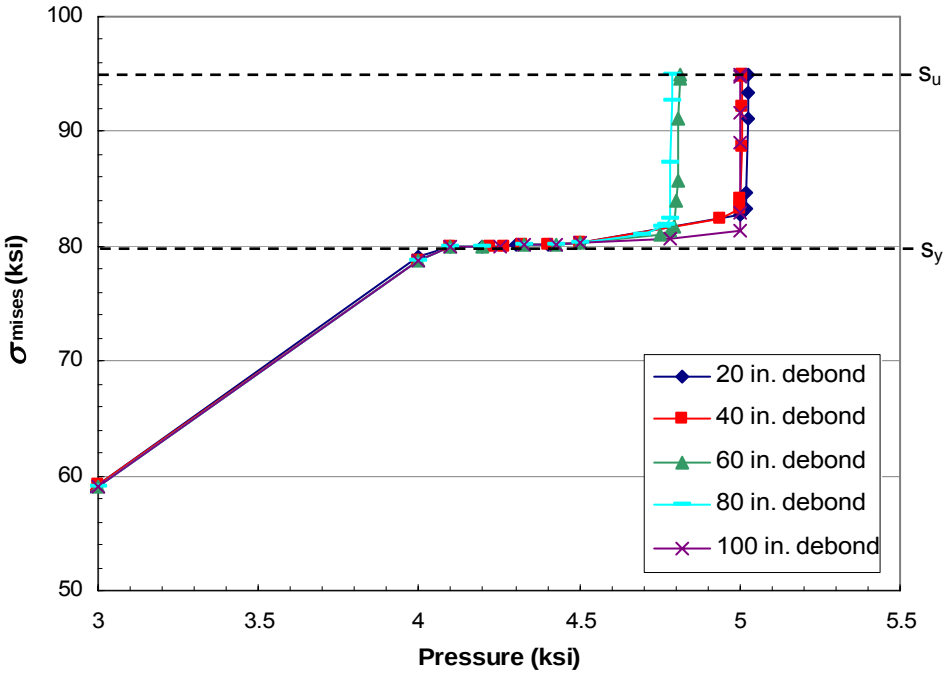

Fig. 22. Maximum stress vs. pressure: through-circumference debonds.

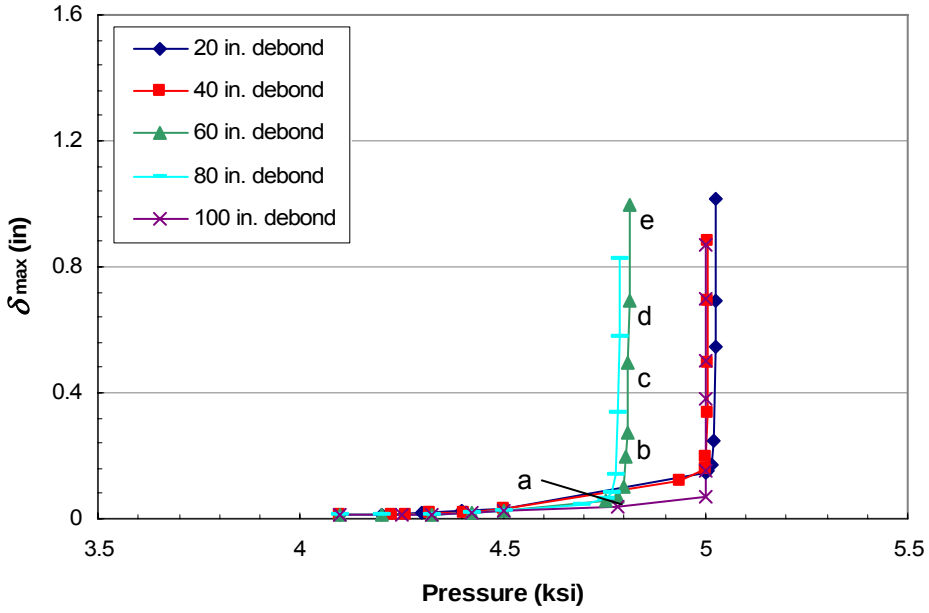

(a)

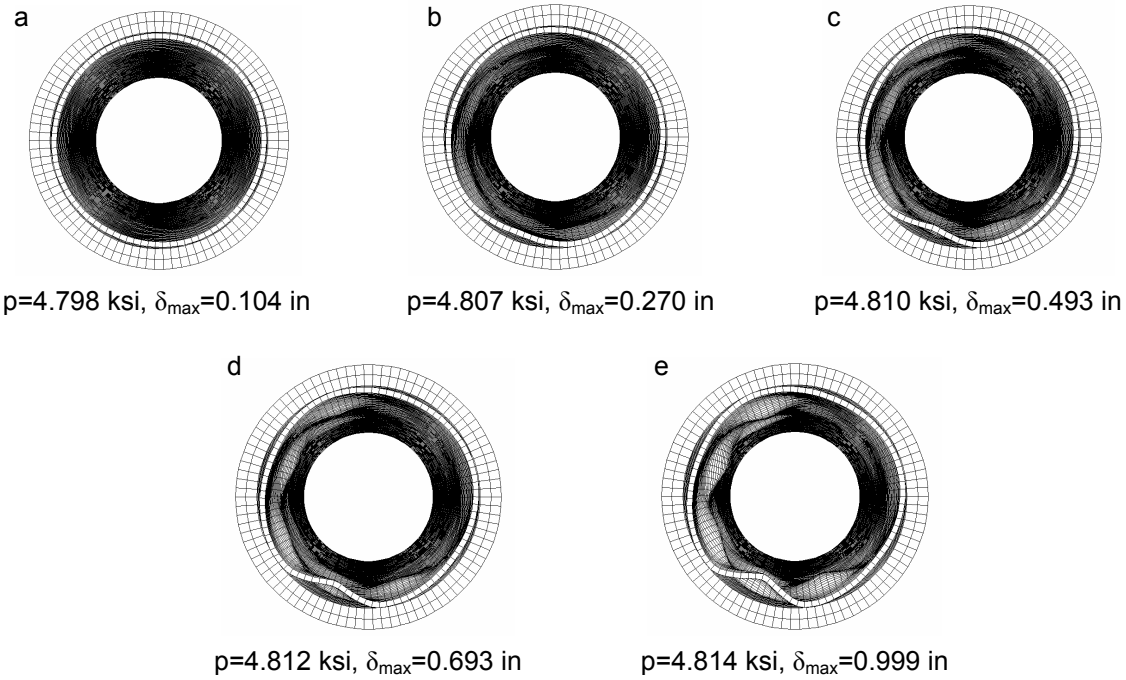

(b)

Fig. 23. Expansion of gap: through-circumference debonds. (a) Maximum gap vs. pressure (b) Cross-section for l_{debond} = 60 in.

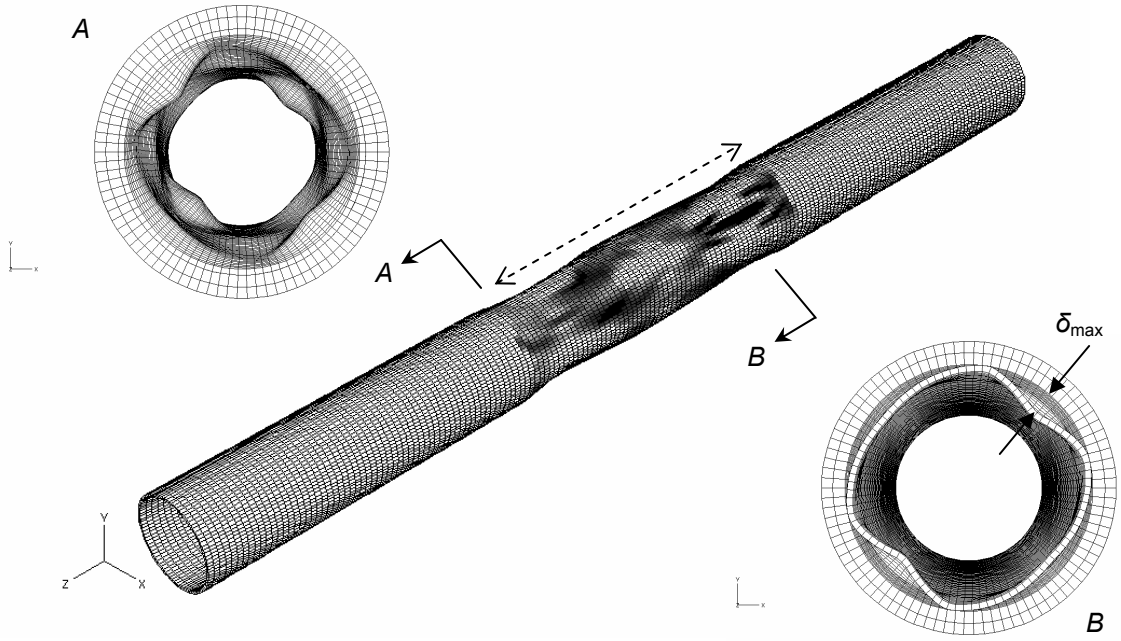

(a)

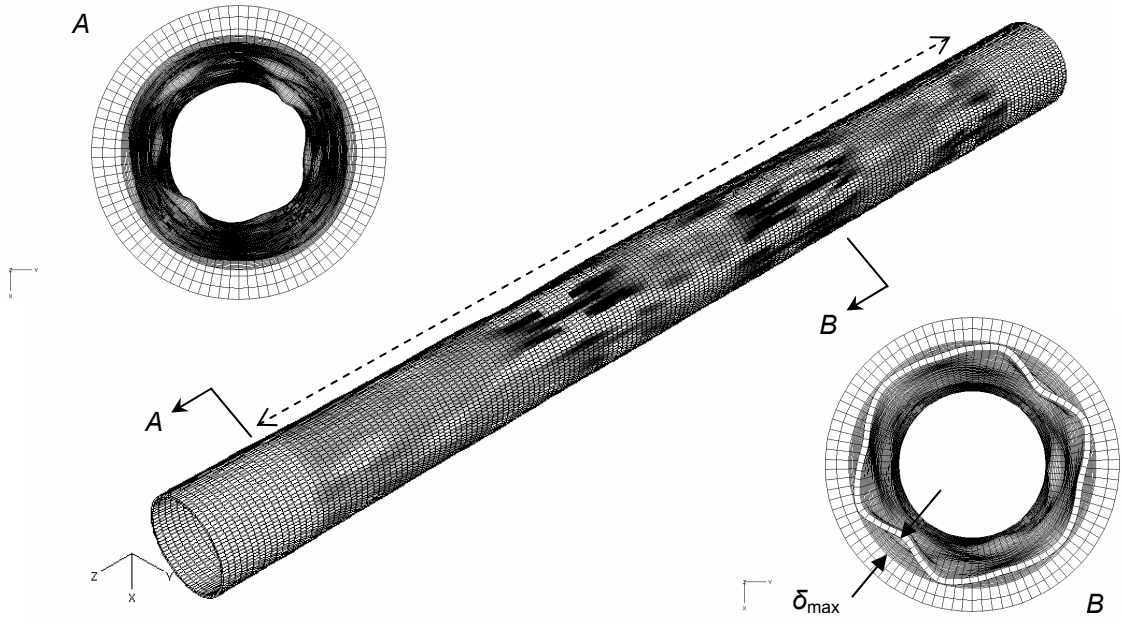

(b)

Fig. 24. Failed areas and cross-sections: through-circumference debonds. (a) l_{debond} = 40 in (p = 5.0083 psi, δ_{max} = 0.885 in) (b) l_{debond} = 100 in (p = 5.0013 psi, δ_{max} = 0.872 in).

The through-length type debonds promote yielding and collapse significantly when compared to the through-circumference type. Fig. 25 shows the maximum stress versus incremental pressure curves. Due to the connectivity between the liner and composite, neither the structure nor loading is axisymmetric. Therefore, the cross-section of the liner tend to deviate from the perfect circle faster than when the entire cross-section is debonded, expediting both yield and collapse. The smallest debond, where the debond arc angle (θ_{debond}) is 40°, shows a unique behavior, as can be seen in Fig. 26. In this particular case, collapse appears throughout the length, and the small debond width arrests the advancement of radial deformation. Therefore, the instability ends before the maximum stress reaches the ultimate strength, and the liner carries additional 300 to 400 psi until it fails.

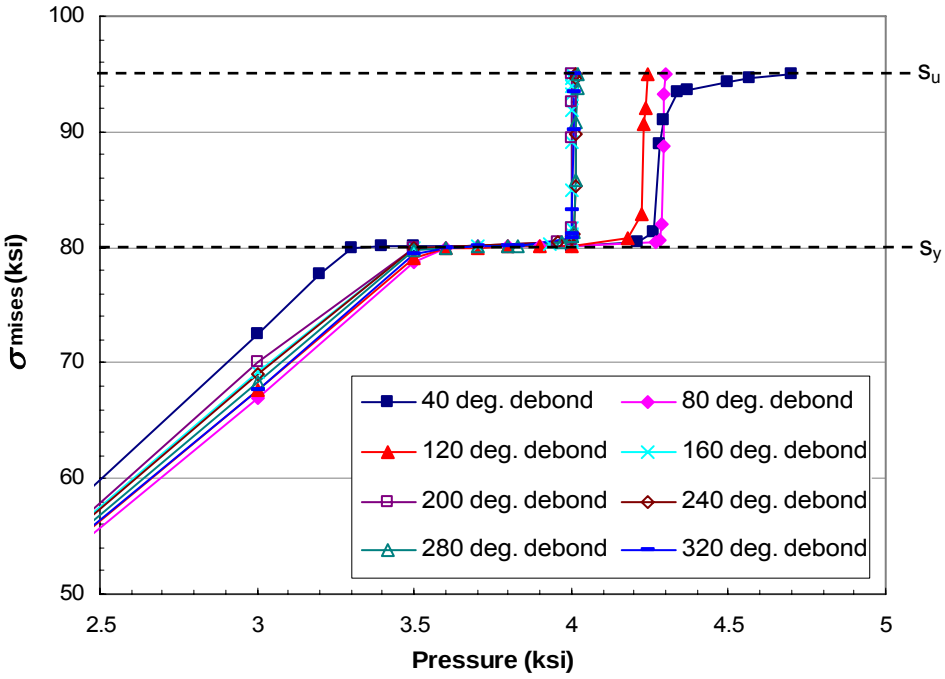

Fig. 25. Maximum stress vs. pressure: through-length debonds.

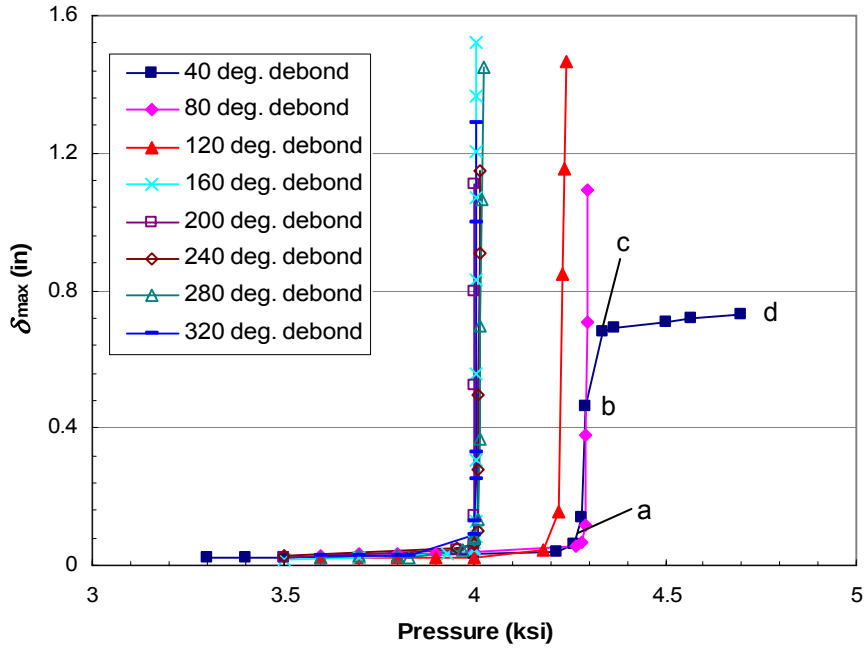

(a)

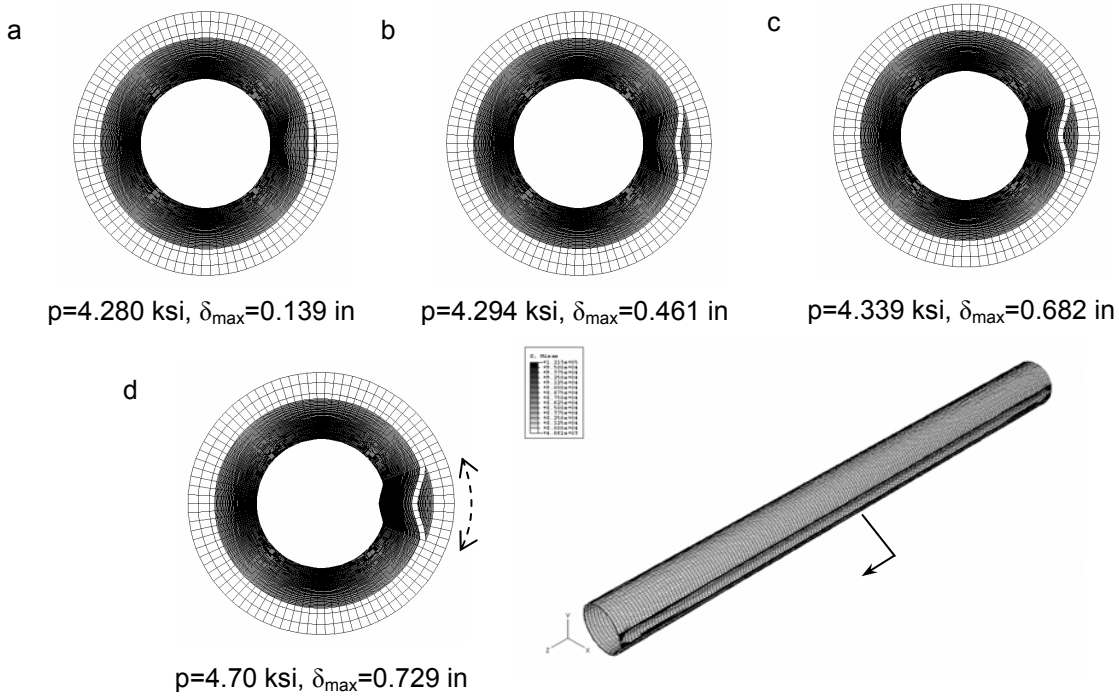

(b)

Fig. 26. Expansion of gap: through-length debonds. (a) Maximum gap vs. pressure (b) Cross-section for $\theta_{debond} = 40°$.

On the other hand, collapse is local for the rest of the through-length debonds, as seen in Fig. 27. When θ_{debond} is 80°, the collapse location is about a quarter of the length of the model away from the top, which is axially unconstrained. In the figure, it can be seen that another collapse location begins to appear on the opposite side when the collapse in the main location is fully developed. For θ_{debond} = 120° or larger, the location of collapse is the top end which axially unconstrained. For θ_{debond} = 160° and above, the debond arc angle has hardly any effects on the collapse capacity of the liner as shown in Fig. 25 and 26. However, the cross-sectional deformed shapes differ, and therefore, the progression of δ_{max} differs as well. Fig. 28 presents the cross-sectional shapes for debond arc angles of 120° through 320°.

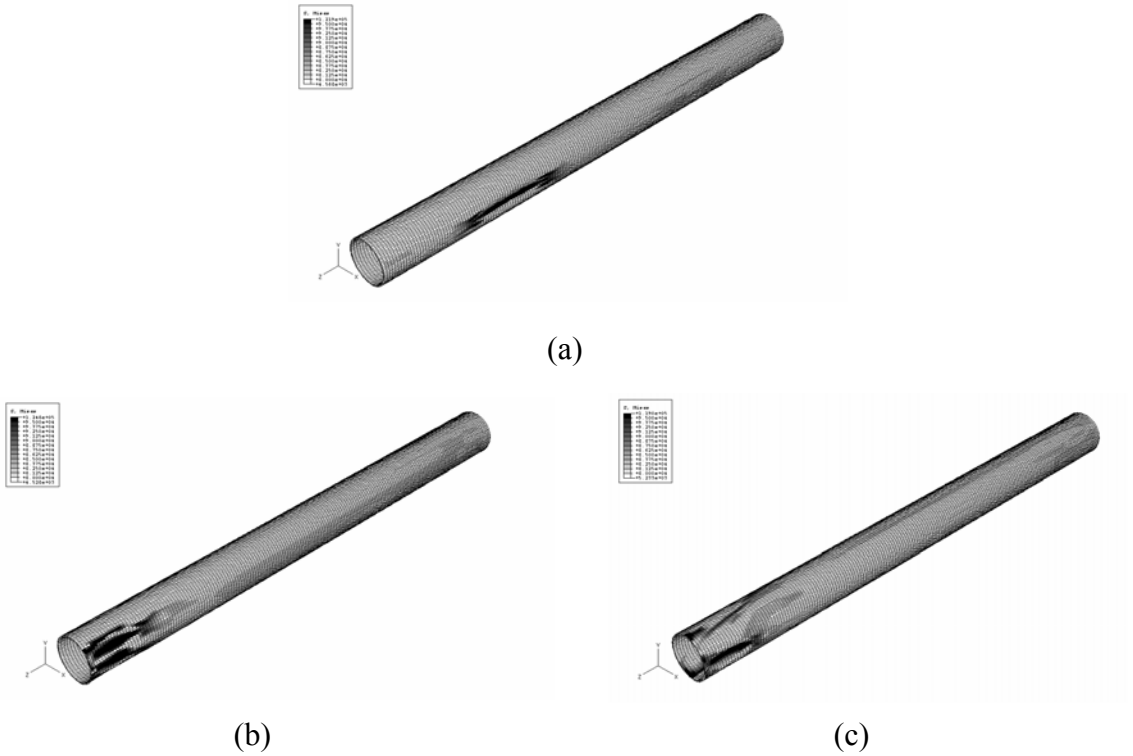

(a)

(b) (c)

Fig. 27. Locations of liner collapse for selected cases. (a) 80° (b) 160° (c) 280°.

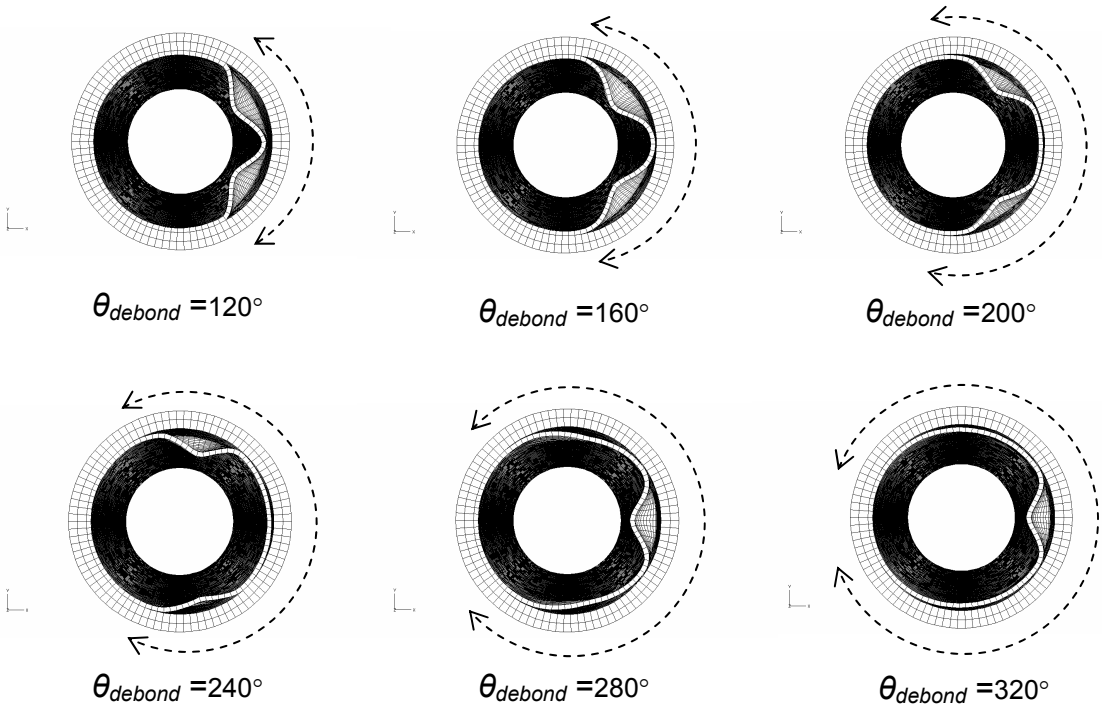

Fig. 28. Cross-sectional shapes of the liner at failure.

4.2. Combined loads: tension and bending

4.2.1. Global response

In this section, the results of the single-wave time domain analysis are presented and compared with the frequency domain solution for 100 year hurricane condition from Ref. [46]. Overall, the single-wave time domain global analysis underestimates the axial tension and bending moment that the riser system is subjected to, since it does not fully represent the real wave condition where numerous regular waves coexist. In addition to representing the sea state as a single regular wave and neglecting the heave motion, another significant simplification is the exclusion of the low frequency motion. Fig. 29 and Fig. 30 compare the axial tension and bending moment profiles obtained from the single-wave time domain analysis and the frequency domain analysis. Note that absolute values are plotted for the bending moment profiles.

Fig. 29 shows the axial tension profiles within the composite riser region, which ranges from 102 ft to 5926 ft above the sea floor. Axial tension changes linearly with elevation due to the constant weight per unit length. The single-wave time domain analysis underestimates axial tension, and the underestimation at the top of the composite riser region is 11 %. It appears that not including the low frequency motion of the platform primarily accounts for the difference.

As can be seen in Fig. 30, most part of the composite riser experiences very insignificant amount of bending moment. Within the composite riser region, the bending moment profiles from the two analyses do not show a remarkable difference, the simplified analysis underestimates the bending moment in the stress joint and wellhead region (under 100 ft elevation) by 20 % as shown in the bottom of Fig. 30. Smaller extent of underestimation is observed near the tensioner joint (6050 ft) as well.

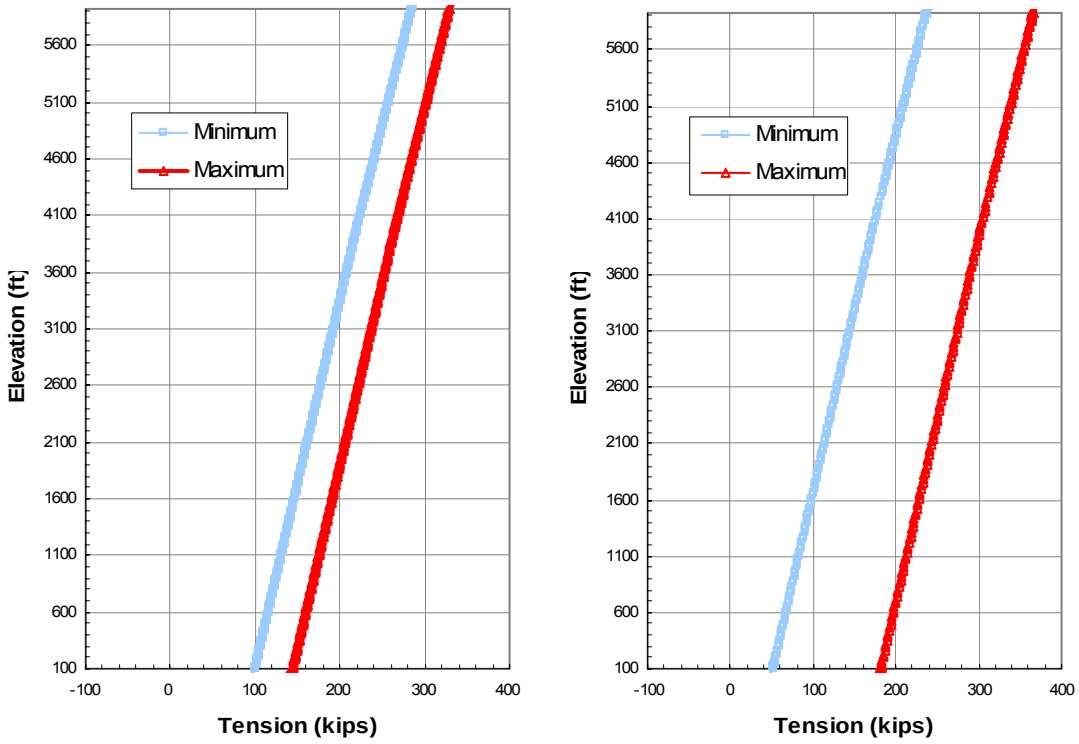

(a) (b)

Fig. 29. Axial tension profile of the composite riser region. (a) single-wave time domain analysis (b) frequency domain analysis [46].

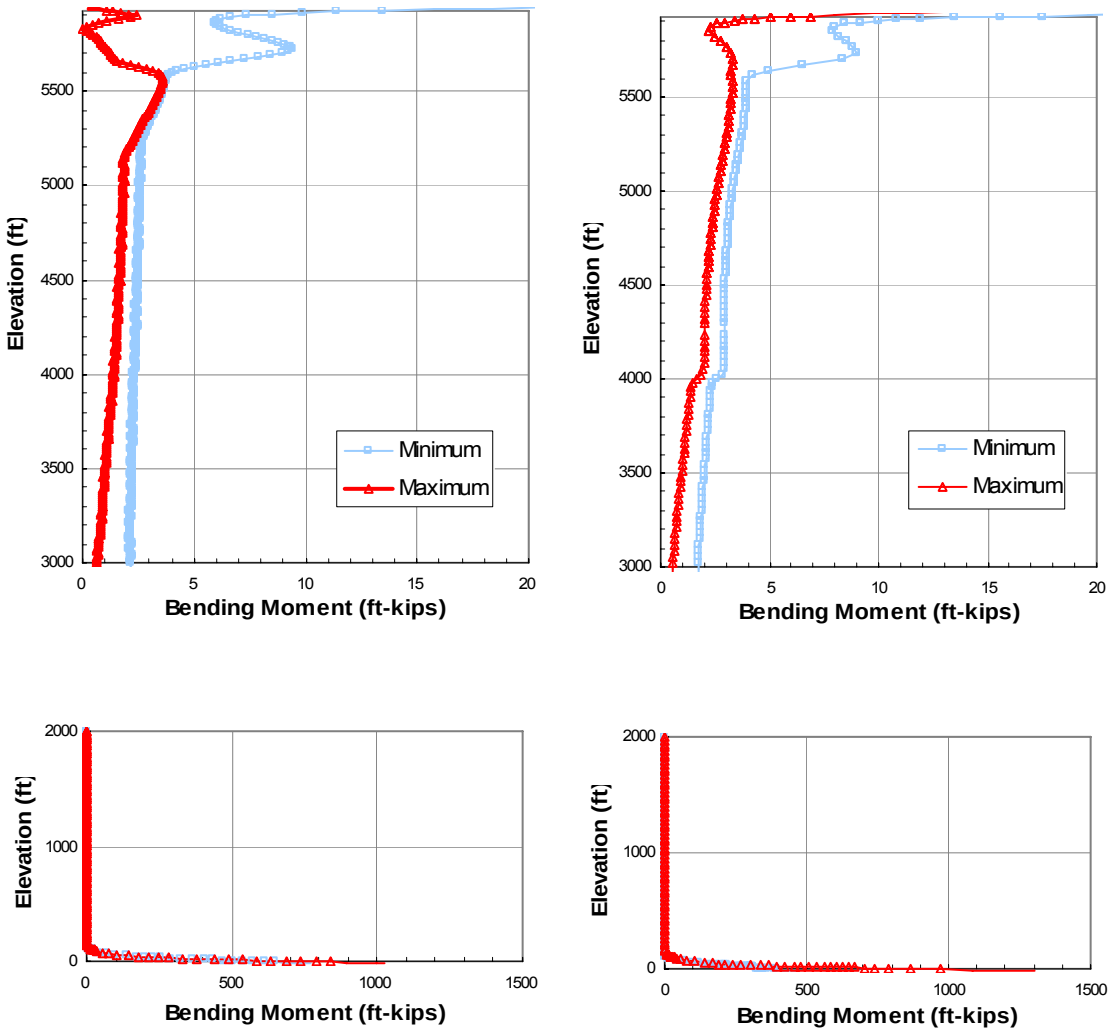

(a) (b)

Fig. 30. Bending moment profile of the composite riser region. (a) single wave time domain analysis (b) frequency domain analysis [46].

4.2.2. Local response

Since the homogenized material properties of the composite tubular are used in the global analysis, lamina stress cannot be obtained directly. Therefore, local analyses must follow the global analyses in order to calculate major stresses on the lamina level, utilizing the nodal degrees of freedom and/or forces obtained from the global analyses. The results for three storm conditions, 100 year hurricane, 100 year loop current, and 1 year winter storm, presented in section 3.2 are applied to the local 10-ft section model.

First, the 20×80 TTT-1 mesh is compared with the 20×80 TTT-2 model and the finer 40×160 TTT-1 mesh. The stress estimates provided by the 20×80 TTT-2 model are slightly greater, and there is no difference at all between the 20×80 and 40×160 TTT-1 meshes. All the subsequent analyses are performed with the 20×80 TTT-1 mesh where the liner is combined with the composite layers, since this mesh hardly compromises the accuracy of the results with the least amount of computational demand.

Under axial tension and bending moment, the major stress components of interest are those along the global z (axial) direction: σ_1 in the axial layers (AL) and σ_2 in the hoop layers (HL). The stresses are presented at the middle of the riser, on the tension side which is the positive x direction in Fig. 31. Due to bending, the major stress among the layers of same orientation is higher as the layer is closer to the exterior. Note that bending moment causes compression on the opposite side, but the sum of stresses caused by axial tension and bending moment is positive unless the tensioner fails to deliver the prescribed tension. Fig. 32 shows the major stress components at the top of the composite riser region under maximum local loads of 100 year hurricane. The stress in the axial layers ranges from 17.4 to 18.1 ksi due to the high modulus in local 1 direction, whereas the stress in the hoop layers is around 0.8 ksi. Shear stress is negligible regardless of the storm condition. As expected, layer 18 shows the greatest stress of all axial layers, and among the hoop layers the stress in layer 19 is the highest. In the rest of this section, the axial layers and hoop layers are represented by these two outermost layers when evaluating stress and damage.

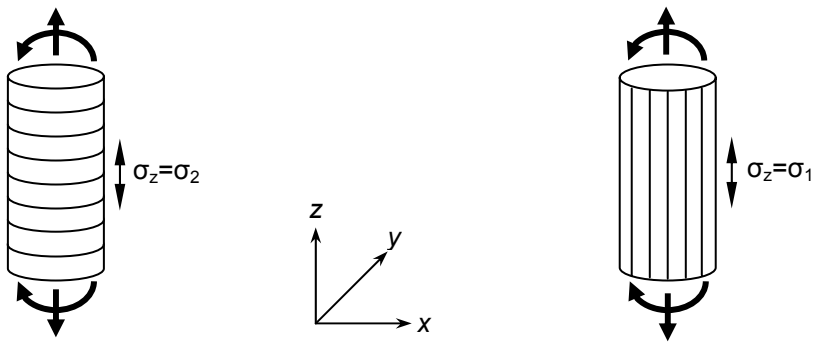

Fig. 31. Major stress components under axial tension and bending moment. (a) hoop layers (b) axial layers.

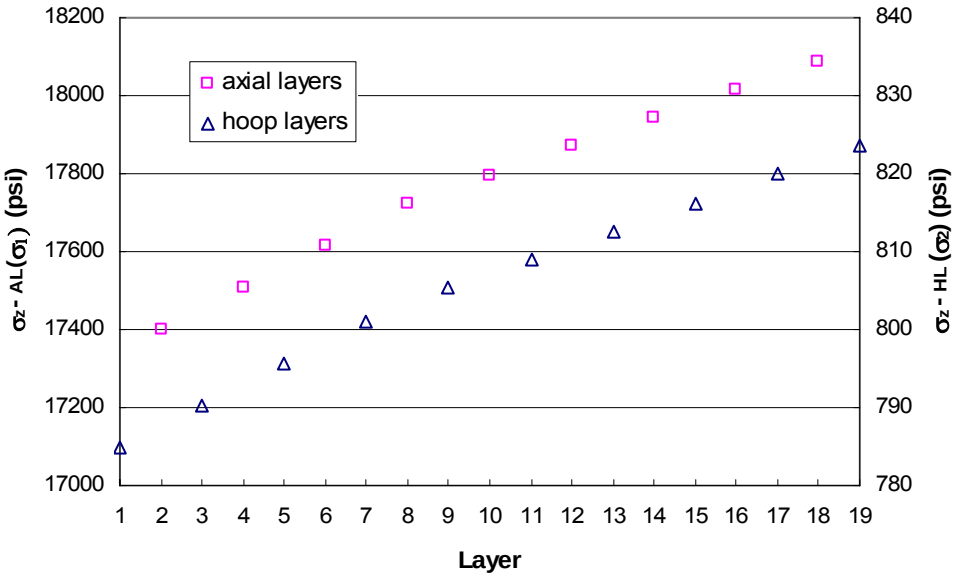

Fig. 32. Major stresses (σ_z) in the composite wall under 100 year hurricane condition.

Examples of stress contours are presented in Fig. 33. This example depicts the state of stress for the liner and the outermost axial layer, under the maximum local loads by 100 year loop current applied to the top section (5916-5926 ft elevation). The stress contours of other storm conditions are similar, except for the ranges of stress.

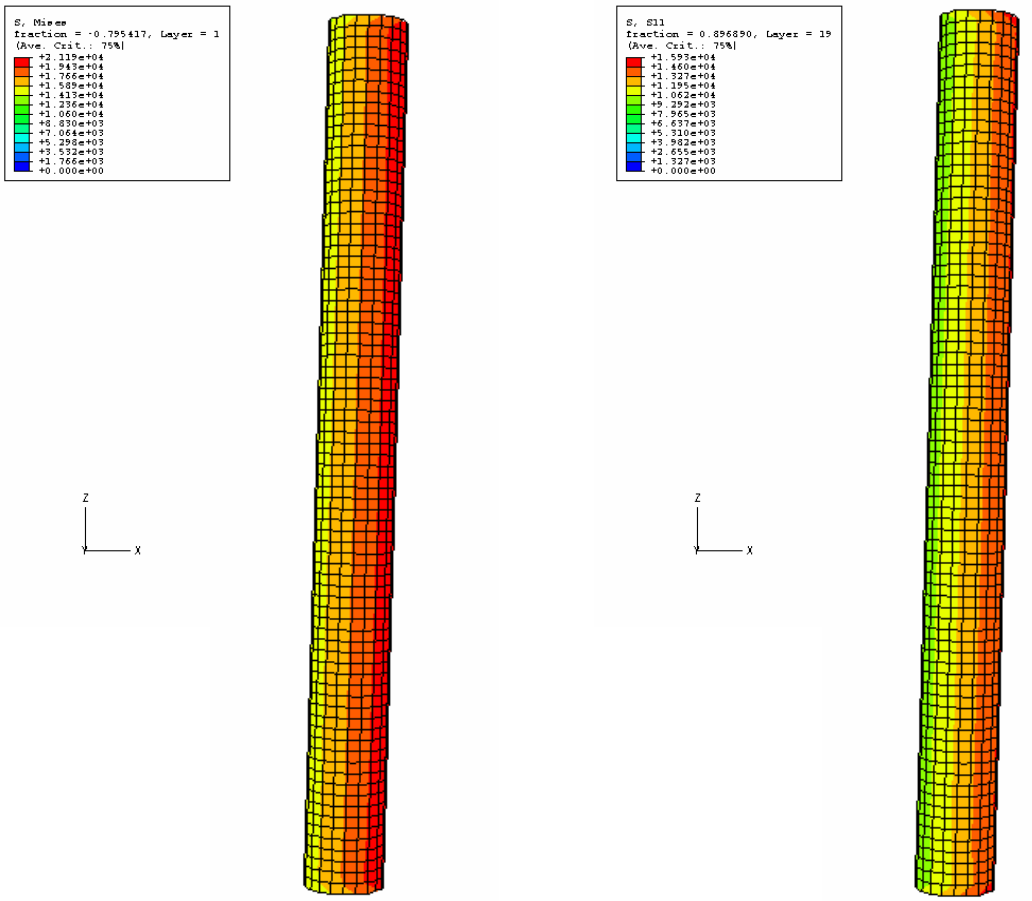

(a) (b)

Fig. 33. Stress contours for 100 year loop current (maximum solution). (a) σ_{mises} in steel liner (22 ksi max.) (b) σ_1 in layer 18 (16 ksi max.).

Table 16 presents the lower and upper limits of σ_z, i.e., von Mises stress in the liner, σ_1 in the outermost axial layer, and σ_2 in the outermost hoop layer at the top section. All three load cases previously defined are considered, and the mean and maximum solutions of each case are applied to the local section model. According to the results, it is highly unlikely that any type of failure will occur. Especially, the stress in the fiber direction is less than 10 % of its long term allowable regardless of load case.

Instead of applying the local loads obtained from global analyses to the local section model, damage in the composite riser can also be predicted in the opposite way. First, damage envelopes are constructed based on numerous local loading scenarios. Then global analysis is performed, and occurrence of damage is predicted based on the location of axial tension and bending moment on the plot with respect to the envelope. The damage envelopes for this study are constructed based on 17 loading scenarios. The loading scenarios consist of predefined tensile preloads followed by incremental bending moment and incremental axial tension after specified bending preloads. Table 17 presents the details of the loading scenarios used for the analyses. The first letter of load designation identifies preload, with the number specifying its magnitude, and the final letter refers to the type of incremental load. Incremental load is applied until the fibers in the axial layers show the first sign of fracture. Note again that axial tension and bending moment are not increased simultaneously.

Table 16

Ranges of axial stresses for storm conditions

σ_z	**Range**											
	minimum (ksi)						**maximum** (ksi)					
	100 yr. hurricane		**100 yr. loop current**		**1 yr. winter storm**		**100 yr. hurricane**		**100 yr. loop current**		**1 yr. winter storm**	
	Mean sol.	**Max. sol.**	**Mean sol.**	**Max. sol.**	**Mean sol.**	**Max. sol.**	**Mean sol.**	**Max. sol.**	**Mean sol.**	**Max. sol.**	**Mean sol.**	**Max. sol.**
Von mises, liner	13.75	8.50	14.50	13.87	13.29	12.51	16.57	28.69	19.82	21.12	14.38	15.99
σ_1, AL (layer 18)	9.69	4.50	10.04	9.45	9.48	8.75	12.05	22.38	14.57	15.65	10.34	11.68
σ_2, HL (layer 19)	0.437	0.197	0.452	0.424	0.429	0.395	0.569	1.06	0.688	0.740	0.488	0.552

Table 17

Loading scenarios used to observe damage initiation and progression

Designation	Preload	Incremental Load
B0T	n/a	Axial Tension, up to 3970 kips
B1T	Bending, 1000 kip-in	Axial Tension, up to 3390 kips
B2T	Bending, 2000 kip-in	Axial Tension, up to 2930 kips
B3T	Bending, 3000 kip-in	Axial Tension, up to 2670 kips
B4T	Bending, 4000 kip-in	Axial Tension, up to 2410 kips
B5T	Bending, 5000 kip-in	Axial Tension, up to 2140 kips
B6T	Bending, 6000 kip-in	Axial Tension, up to 1900 kips
B7T	Bending, 7000 kip-in	Axial Tension, up to 1500 kips
B8T	Bending, 8000 kip-in	Axial Tension, up to 1040 kips
T0B	n/a	Bending Moment, up to 8900 kip-in
T5B	Axial Tension, 500 kips	Bending Moment, up to 9200 kip-in
T10B	Axial Tension, 1000 kips	Bending Moment, up to 7850 kip-in
T15B	Axial Tension, 1500 kips	Bending Moment, up to 5150 kip-in
T20B	Axial Tension, 2000 kips	Bending Moment, up to 4100 kip-in
T25B	Axial Tension, 2500 kips	Bending Moment, up to 2200 kip-in
T30B	Axial Tension, 3000 kips	Bending Moment, up to 1300 kip-in
T35B	Axial Tension, 3500 kips	Bending Moment, up to 450 kip-in

The results for the loading scenario of Table 17 are presented in Fig. 34. The damage modes that are tracked throughout the load increments are yield limit for steel liner, matrix cracks in hoop layers, and fiber fracture in axial layers. For each scenario, the magnitudes of applied loads that initiate each damage mode are plotted. The hollow symbols represent the loading scenarios where bending moment is applied as preload,

and the solid symbols indicate that axial tension is applied as preload. Regardless of the loading scenarios, liner yield occurs first, followed by matrix cracking in hoop layers and then by fiber fracture in axial layers.

The load combinations that predict liner yield form the straight line AB in Fig. 34. Obviously, any combination of axial tension and bending moment that lies beneath line AB will not cause liner yielding. On the other hand, the points indicating fiber fracture in axial layers do not form a single smooth curve. Instead, they are separated into two groups according to preload types; the cases where the preload is tension form the lower bound, and those associated with bending preload form the upper bound. The same observation applies to matrix cracking in the hoop layers, to which the separation of points indicating damage is less pronounced.

Post liner yield, i.e., for load combinations outside line AB, the initiation and growth of damage mode in a layer follow different paths. For example, loading scenario B4T, in which axial tension is added immediately after passing point A, sees a gradual spreading of the damage. At point A, liner yield appears locally, and adding axial tension does not immediately lead to yielding of the entire liner. On the contrary, T15B case passes point B via preload tension, where the entire liner yields and no longer carries applied loads. As bending moment is added after passing point B, the remaining layers experience accelerated initiation and progression of damage. Since the severity of damage experienced by a layer affects the stress state of the remaining layers, the load history is consequential to forthcoming damage mode and eventually to complete failure of the riser. It can be expected that any combinations of tension and bending that are increased simultaneously will fall within the bounds. For practical purposes, the lower bound may be considered as the envelope for each damage mode.

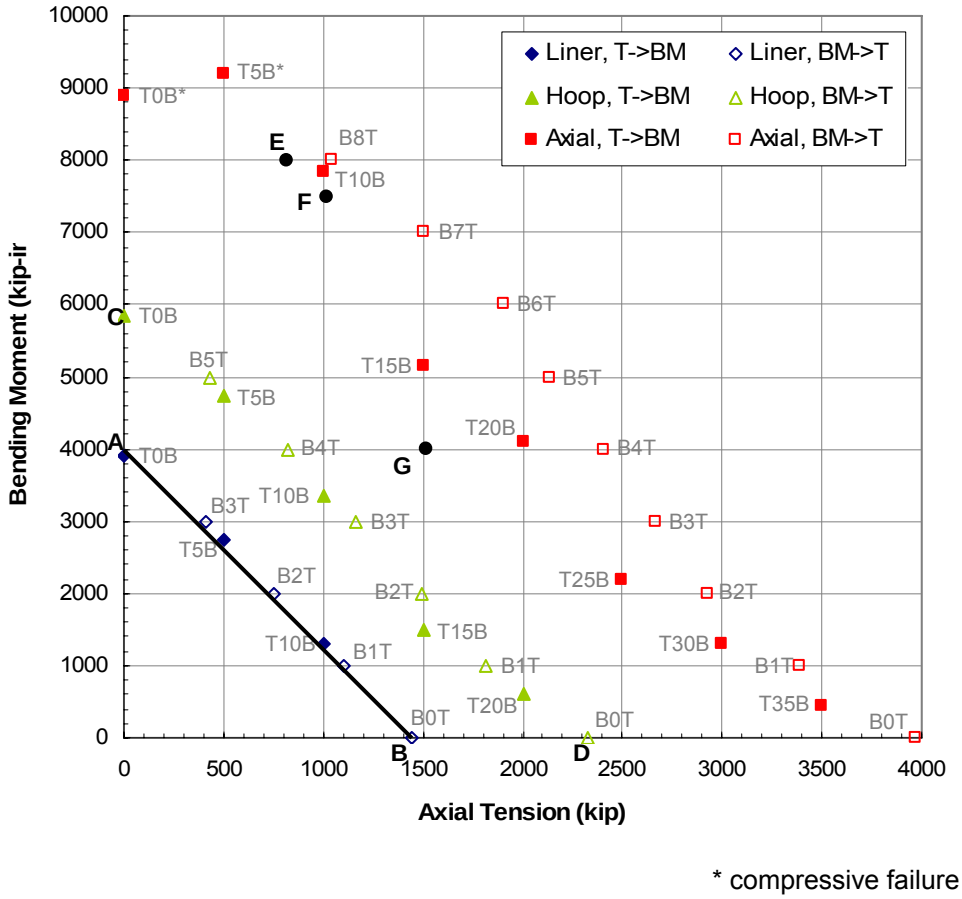

Fig. 34. Combinations of axial tension and bending moment for damage initiation.

Instead of examining the entire loading scenarios presented in Fig. 34, when our interest is confined to the scenarios with tension preload, i.e., T0B through T35B, three distinct zones can be observed in Fig. 35. The zones reflect the damage initiation points on the horizontal axis: points B and D. In zone I, no damage occurs under the prescribed axial tension, and damage begins to take place when additional bending moment is applied. In zone II, the liner has fully yielded and carries no load. In zone III neither the

liner nor hoop layers carry any load; only the fibers in axial layers bear the entire load. The discontinuous slopes at the zone junctions are attributed to load and damage history. Note that fiber fracture in zone I does not present a straight line since cases T0B and T5B fail in compressive mode. Due to the lower compressive strength in local 1 direction, damage occurs on the compression side under combinations of high bending moment and minor axial tension.

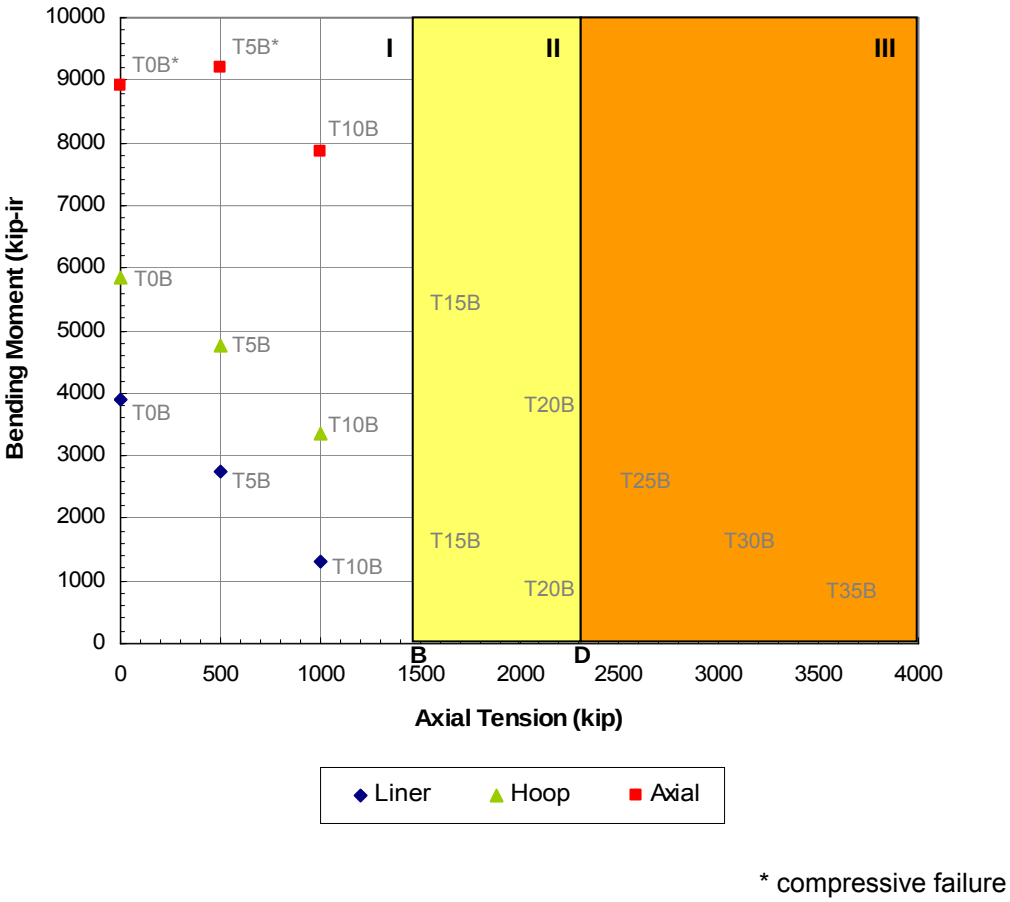

Fig. 35. Envelopes for tension preload cases and three damage zones.

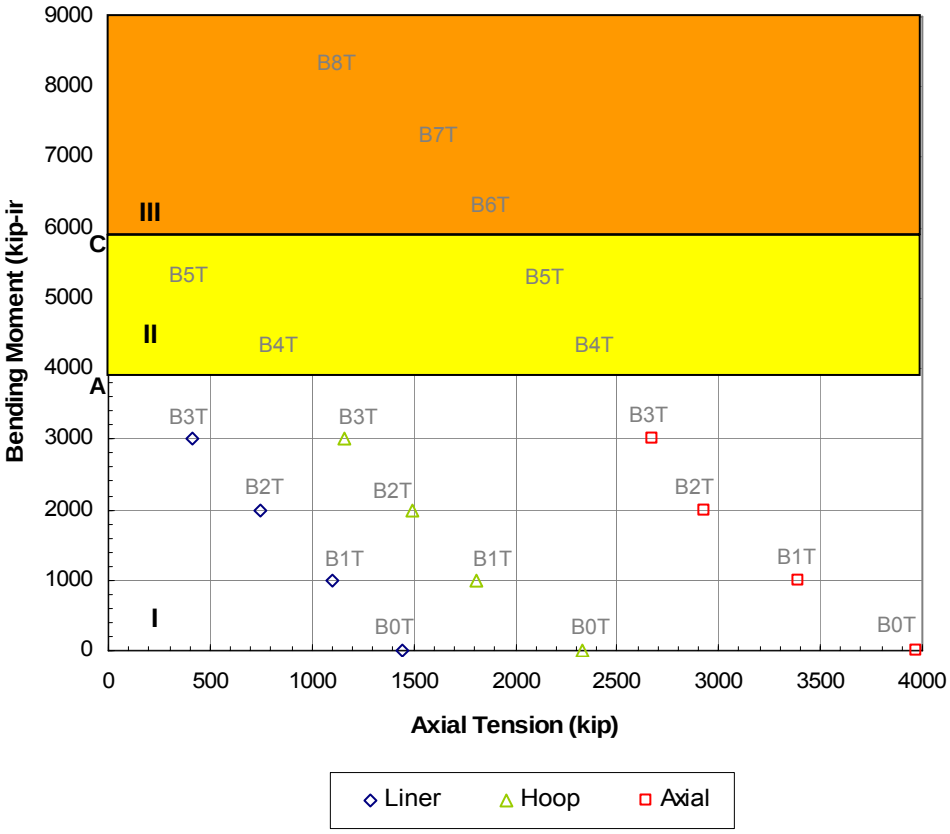

Fig. 36. Envelopes for moment preload cases and three damage zones.

Fig. 36 shows the envelopes for the load scenarios where bending moment is applied as preload. The zones in this case are defined base on point A and C in Fig. 34. In zone I, no damage occurs by prescribed bending moment. In zone II, partial yielding of the liner takes place, and in zone III, hoop layers are partially damaged as well as the liner. Each zone represents the damage mode(s) induced by preload, which is analogous to Fig. 35. However, note again that damage is relatively local in these cases. Unlike the previous set of cases, no discontinuity between the zones is observable. The curvature of the continuous curve slightly changes as they enter different zones.

The loading scenario B8T prior to final failure, which is designated as point “E” in Fig. 34, is presented in detail in Fig. 37 (a). Damage state at point “F”, which represents T10B scenario prior to failure, is presented Fig. 37 (b) for comparison. Although final failure under B8T and T10B scenarios occur at very similar magnitudes of axial tension and bending moment, the damage state of the liner and hoop layers prior to failure is far from identical. Fig. 38 shows the damage state at point “G” resulting from two different paths, B4T and T15B. In spite of the same magnitudes of axial tension and bending moment, damage state of the liner and the outermost hoop layer resulting from the two different scenarios is distinguishable. Note that in T15B scenario, the liner yields under the prescribed tension preload, accelerating the other damage modes as a result.

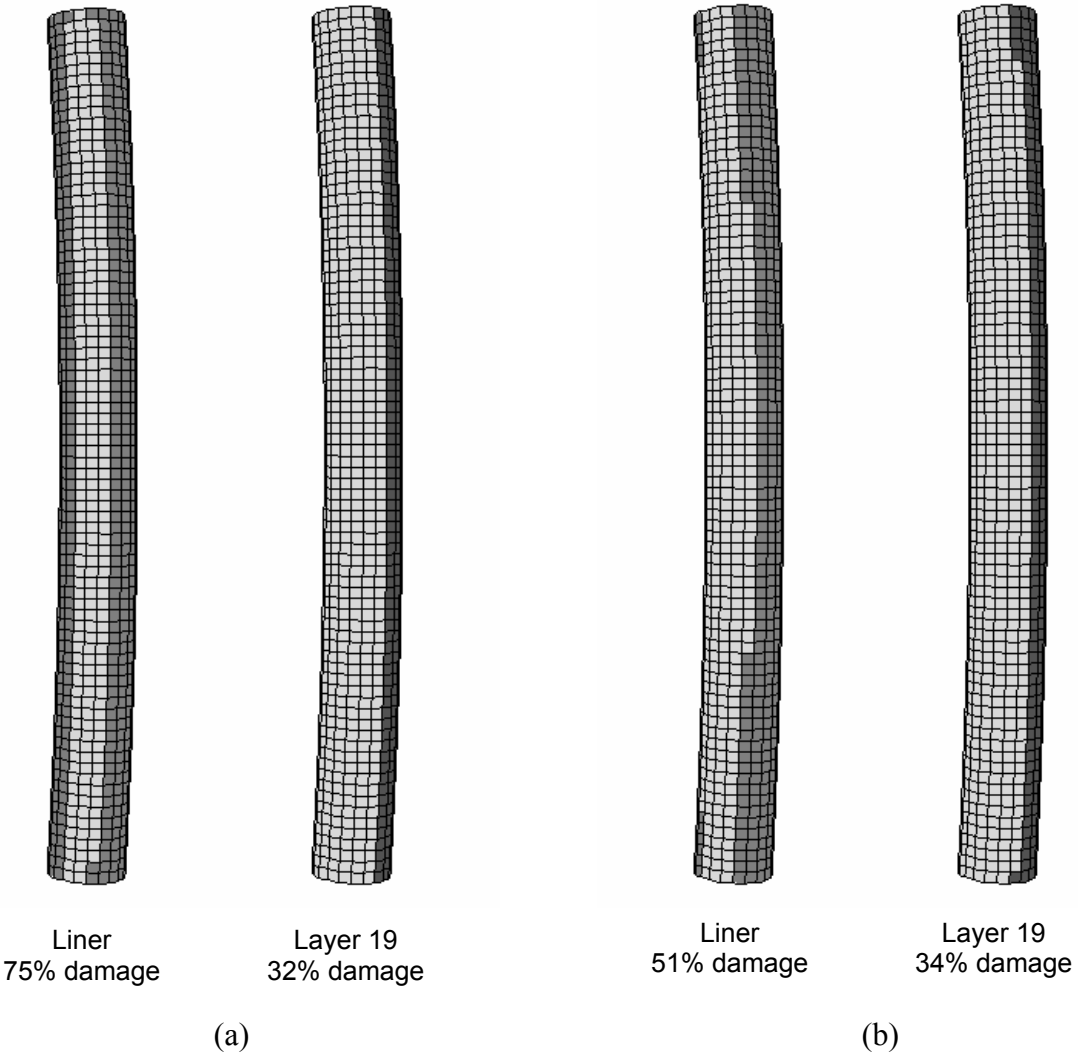

Fig. 37. Elements with damage in the liner and outermost hoop layer before failure. (a) Point “E” (8000 kip-in + 800 kip) (b) Point “F” (1000 kip + 7500 kip-in).

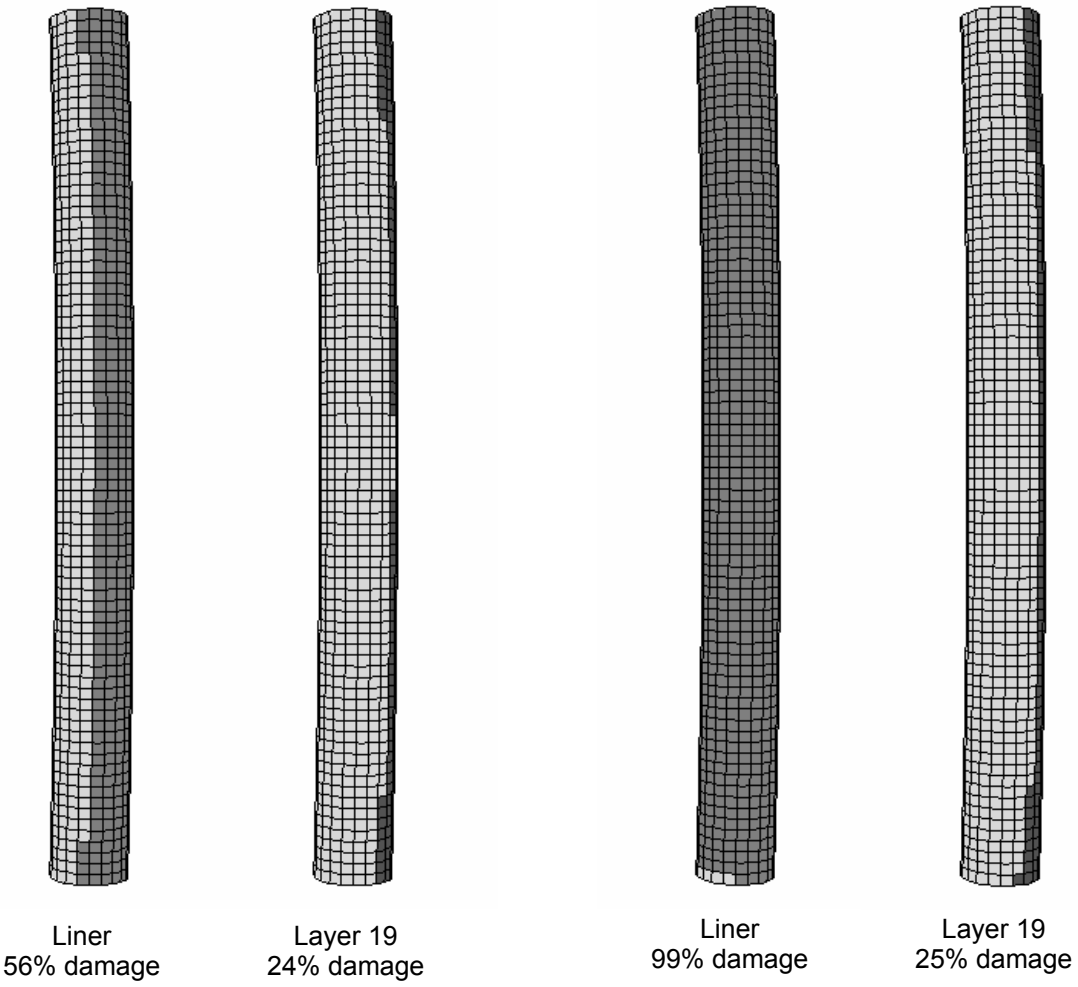

Fig. 38. Elements with damage in the liner and outermost hoop layer resulting from different load histories, at point "G" (4000 kip-in bending and 1500 kip tension). (a) B4T (b) T15B.

The local loads experienced at the top (5926 ft) and bottom (102 ft) of the composite riser during the storm conditions as provided by Ref. [46] are presented in Fig. 39. Note that the steel liner yield line of Fig. 34 is now at the upper right hand corner. For the current system configuration and environmental loads, the composite riser has excessive capacity for sustaining axial loads. It will be possible to extend the use of the composite joints to locations that are subject to more intense loads: for example, near the sea surface and next to the stress joint where steel joints are currently utilized.

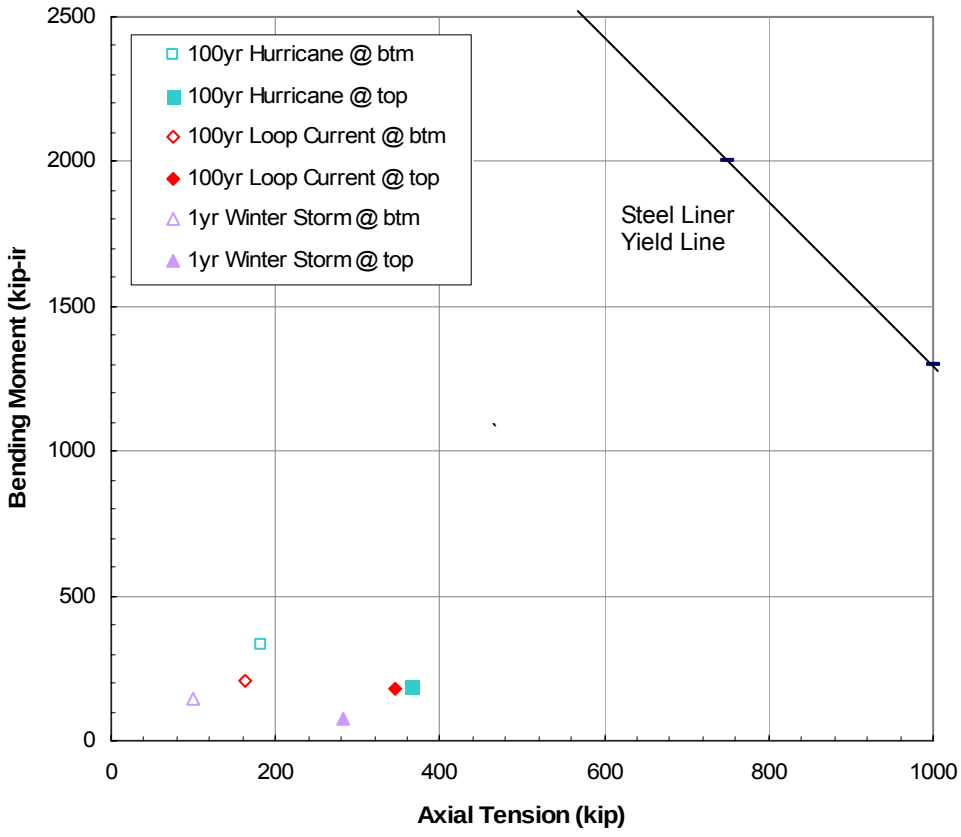

Fig. 39 Local axial loads under the storm conditions.

4.3. Fatigue

In this section, estimates of fatigue damage and life of the composite body and steel liner are presented. Fatigue is assessed at the extremities of the composite riser region: 102 and 5926 ft above the seabed. For the composite body, five semi-log relationships are applied first without finding equivalent stresses using the constant life diagram. To investigate the mean stress effect, the diagram is utilized for a selected case. Also, five power law relationships with various exponent values are applied, and the damage values from the individual sea states as well as the total damage are compared with the results from the semi-log relationships. For the steel riser, two well-established design S-N curves are used for the estimation of fatigue life at welds: one for high quality welds and the other for moderate quality.

The stress data from the short term sea states show that σ_{RMS} is far greater in higher sea states while the variation of σ_{mean} is moderate. Stress histograms in Fig. 40 show the differences in resulting stress among the sea states. As discussed in section 3.3., a low sea state is characterized by small and short waves, and therefore, the distribution of stress range is narrow as seen in Fig. 40 (a) and (b). However, due to its short period, its number of cycles is large. Furthermore, all the sea states with high probability of occurrence are in the lower half. On the other hand, (c) and (d) show that the high-magnitude stresses resulting from the high sea states have nearly negligible number of cycles.

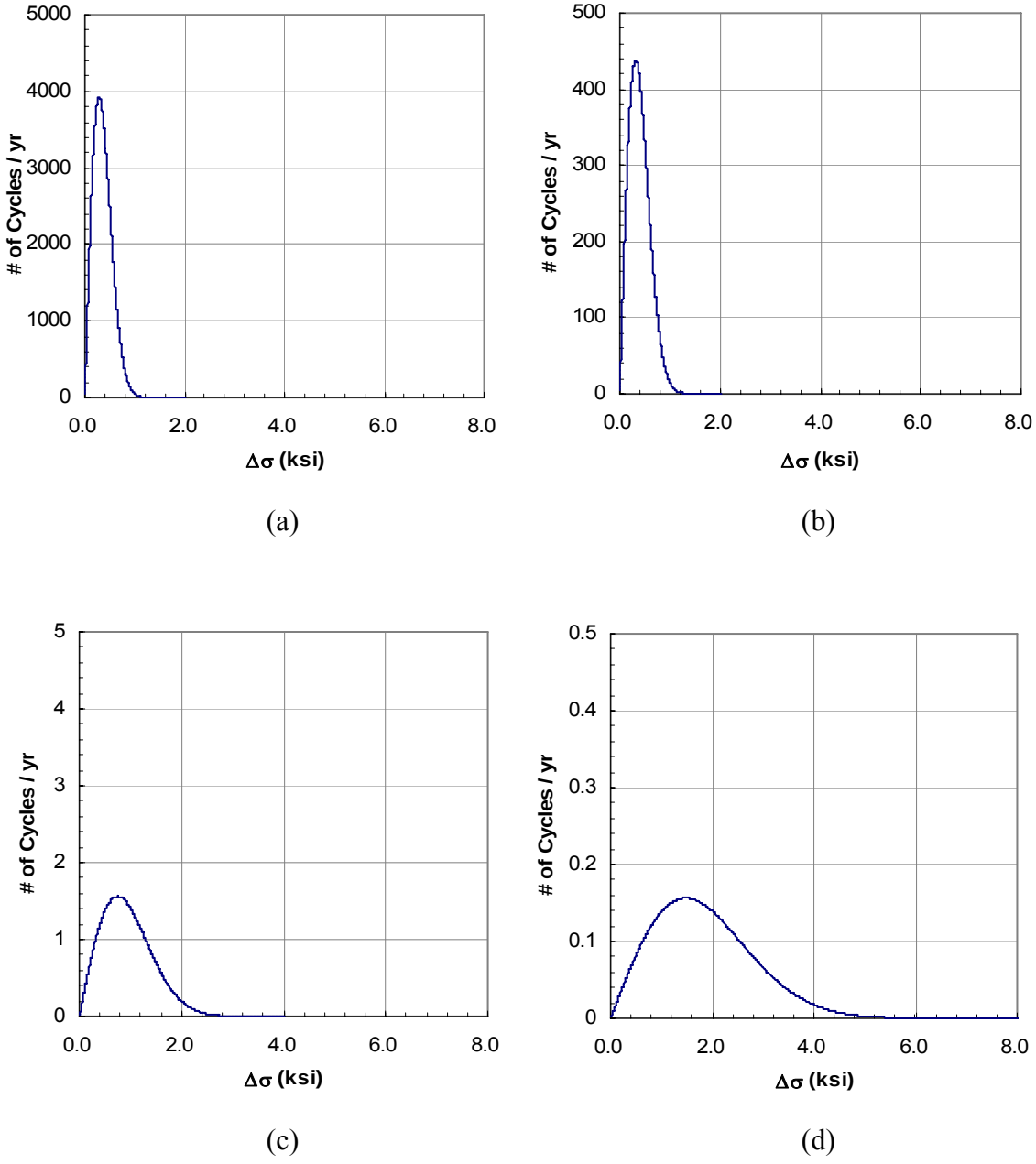

Fig. 40. Stress histograms for 102 ft elevation. (a) Sea 1 (b) Sea 10 (c) Sea 15 (d) Sea 20.

4.3.1. Semi-log S-N relationships for composite

The uniaxial composite S-N curve from Ref. [60] shows extremely high fatigue resistance with the degradation constant *b* being only 0.01. The value of *b* for typical carbon-epoxy composites used for offshore applications ranges from 0.02 to 0.03, and 0.04 is a fairly conservative value [96]. First, based on the possible range of S-N relationships as discussed, the S-N relationships presented in Table 18 are applied to determine cycles to failure for each stress level.

The normalized maximum stress *S* for individual stress level ranges from 0.02 to 0.09, which is associated with extremely high cycles ($> 10^{18}$) as can be seen in Fig. 41. Therefore, it can be expected that the slightest difference in *b* would greatly affect the fatigue life estimate.

Table 18

Semi-log S-N relationships ($S = a - b\log N$)

Designation	a	b
SN1*	0.861	0.01
SN2	1	0.02
SN3	1	0.03
SN4	1	0.04
SN5	1	0.05

* Ref [60]

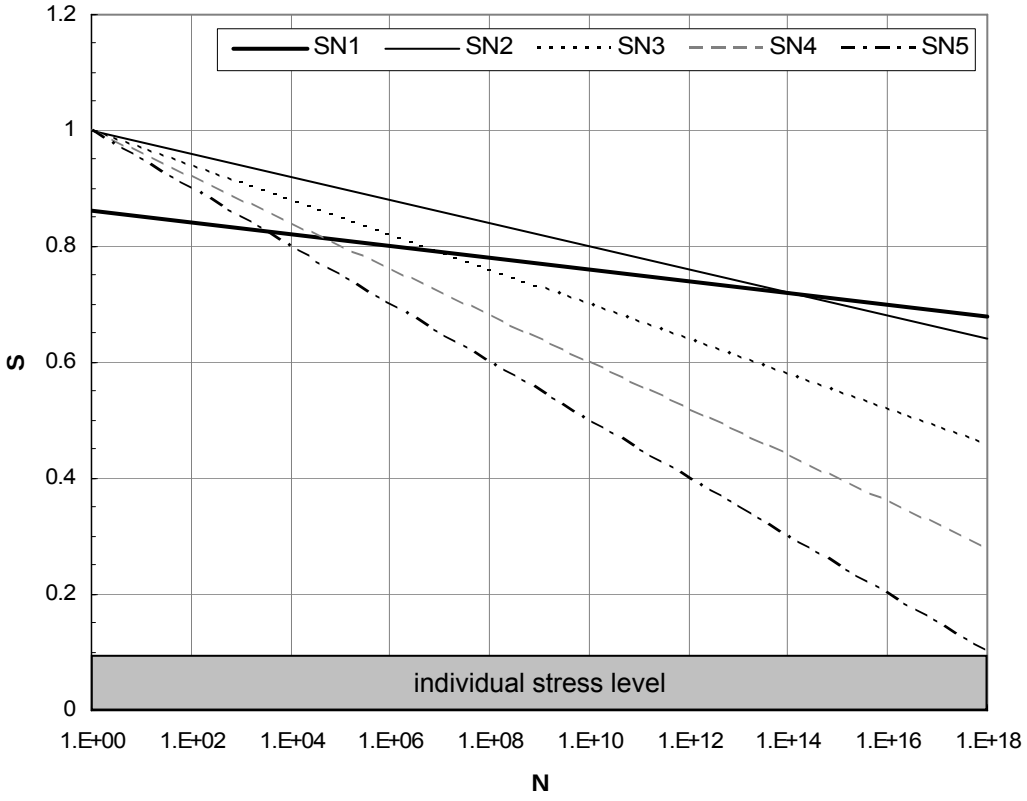

Fig. 41. Semi-log S-N curves for unidirectional carbon-epoxy composites.

Fatigue life estimates from each S-N curves are presented in Table 19, where it can be seen that the top sustains slightly more damage than the bottom. For b ≤ 0.04, expected fatigue life presents an ample safety margin, and when b ≤ 0.03, the life is nearly infinite. The calculated life at $b = 0.05$ (SN5) does not meet the intended design life. Even in the case of such an extensive damage, the damage from one category in the histograms appears negligible; the total damage is obtained through summing up tens of thousands of individual damage values. The contribution of each sea state to the total damage is presented in Fig. 42. The contributions are not affected by the degradation of the S-N curve, and the distribution is primarily determined by the probabilities of the sea

states, especially at the 102 ft location. The distribution at the top (5926 ft) is affected by both σ_{RMS} and the probabilities of occurrence.

Table 19

Fatigue life estimates (semi-log S-N)

Location	SN1	SN2	SN3	SN4	SN5
102 ft	2.7×10^{29}	1.5×10^{14}	1.1×10^{7}	3204.7	23.71
5926 ft	3.1×10^{28}	6.3×10^{13}	7.7×10^{6}	2693.5	22.75

(years)

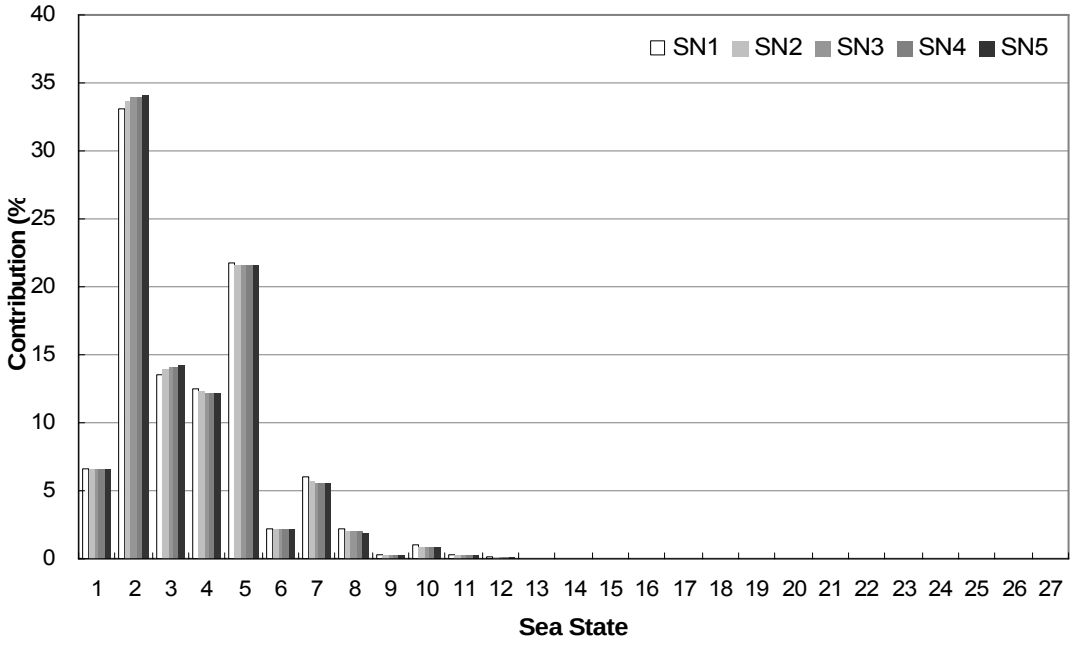

(a)

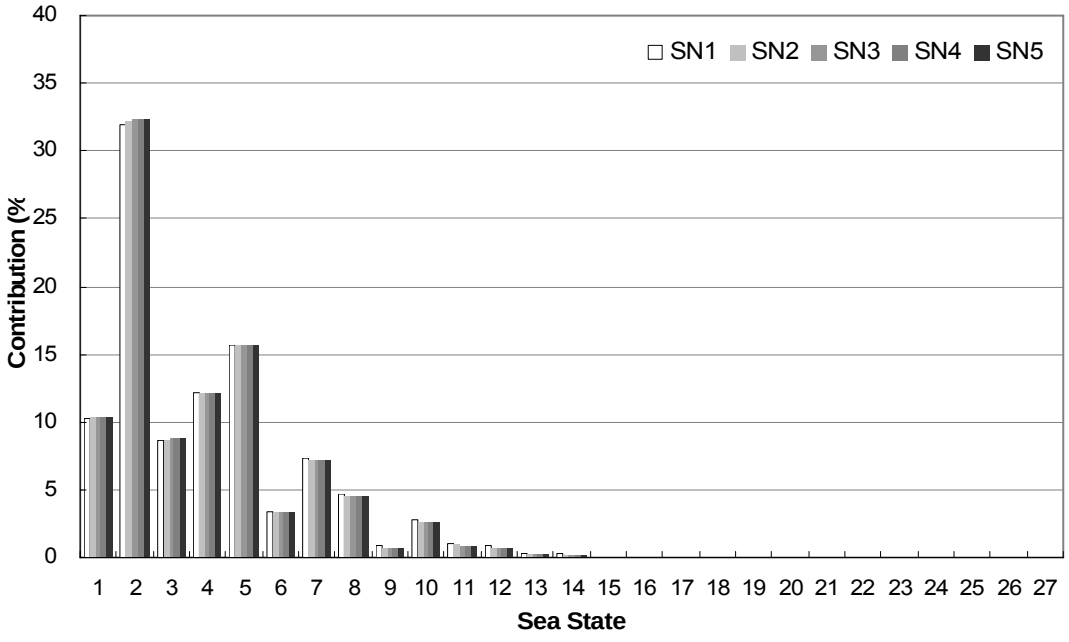

(b)

Fig. 42. Damage contribution of each sea state: semi-log S-N. (a) 102 ft (b) 5926 ft.

It was discussed in section 3.3 that when the effect of mean stress is taken into account, stress cycles for which $0.1 < R < 1$ result in less damage than the prediction from raw S-N curve with $R = 0.1$. Ref. [68] reported a very poor S-N curve with a degradation as high as 0.05 with $R = 0.1$, which is very similar to SN5. Now stresses are converted into equivalent stresses with $R = 0.1$, and the SN5 curve is utilized to examine how this adjustment affects the prediction. Equivalent stress for each stress level in the histograms is extrapolated from the known constant life lines before the SN5 curve is utilized to obtain the cycles to failure. The estimated fatigue life at the bottom is 34 years, which is about 45% increase from the previous prediction. The estimate for the top shows as much as 146% increase, with 56 years of fatigue life. It should be noted that the top is subjected to far greater mean stress due to higher mean tension. Without the adjustment, the top was estimated to undergo higher fatigue damage than the bottom, but the adjustment removes the overestimation which was caused by the high mean stresses.

4.3.2. Power law S-N relationships for composite

Next, a power law S-N relationship presented in Ref [74] is utilized to assess the fatigue of the composite body. As mentioned previously, the mean stress effect is taken into account by using the modified normalized stress. Only the axial stress and strength are used instead of an effective stress associated with a stress criterion, since the loading is uniaxial and the stresses in the other directions are negligible. In addition to the reported S-N curve whose exponent is 11.9, four hypothetical S-N curves with reduced exponent values are considered: $n^* = 11$, 10, 5, and 3. Fig. 43 compares the contribution of each sea state to the total damage. Unlike the semi-log S-N curves, dominant sea states differ depending on the degradation of the power law relationships. For $n^* \geq 10$, the sea states of large σ_{RMS} are responsible for most fatigue damage, which is opposite to the estimation of the semi-log relationships. Also, the patterns of sea state contribution at 102 ft (Fig. 43 (a)) and 5926 ft (b) are very dissimilar. Table 20 presents the estimate fatigue life; the results predict that the bottom location has longer fatigue life except

when $n^* = 3$.

As was seen from the results so far, the composite body of the riser is likely to have an infinite fatigue life if the fatigue performance of the material is moderate. Unfortunately, no test data for small stress / large number of cycles conditions are available; most literature data are limited to a million cycles. More accurate evaluations will require extensive test data in the high cycle range. Also, the representation of S-N data should be the form that best fits the high cycle range, preferably near 10^{20} cycles, since a slight difference in S-N data changes the prediction as to how damage is accumulated as well as what the total amount of damage is.

Table 20

Fatigue life estimates (power law S-N)

Location	n^*=11.9	n^*=11	n^*=10	n^*=5	n^*=3
102 ft	5.3×10^{20}	1.4×10^{19}	2.3×10^{17}	4.2×10^{7}	121.2
5926 ft	2.1×10^{20}	4.9×10^{18}	7.3×10^{16}	1.3×10^{7}	197.5

(years)

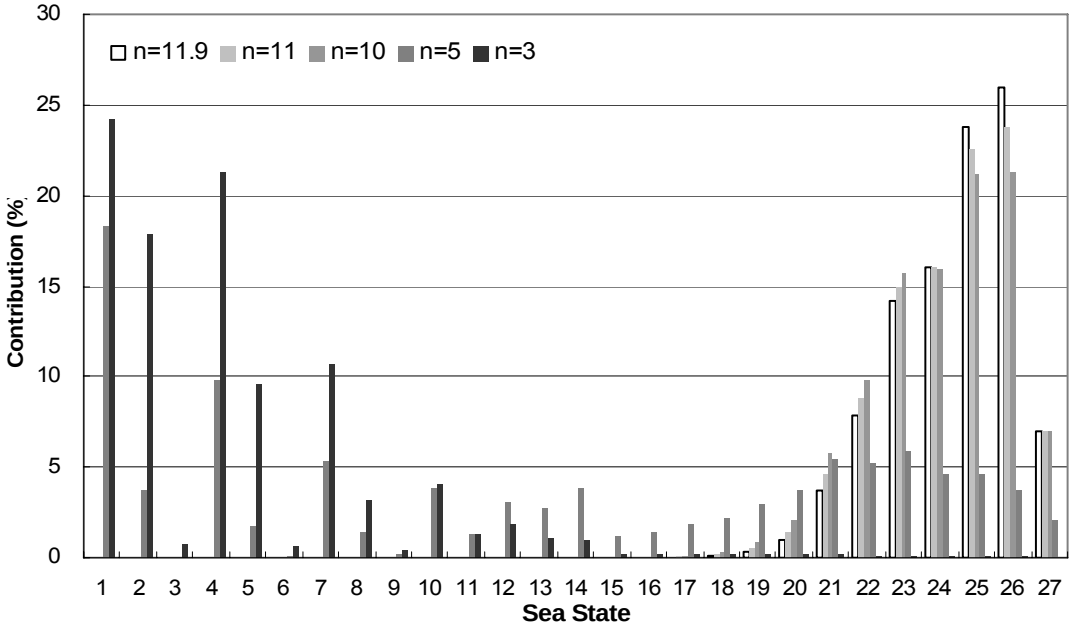

(a)

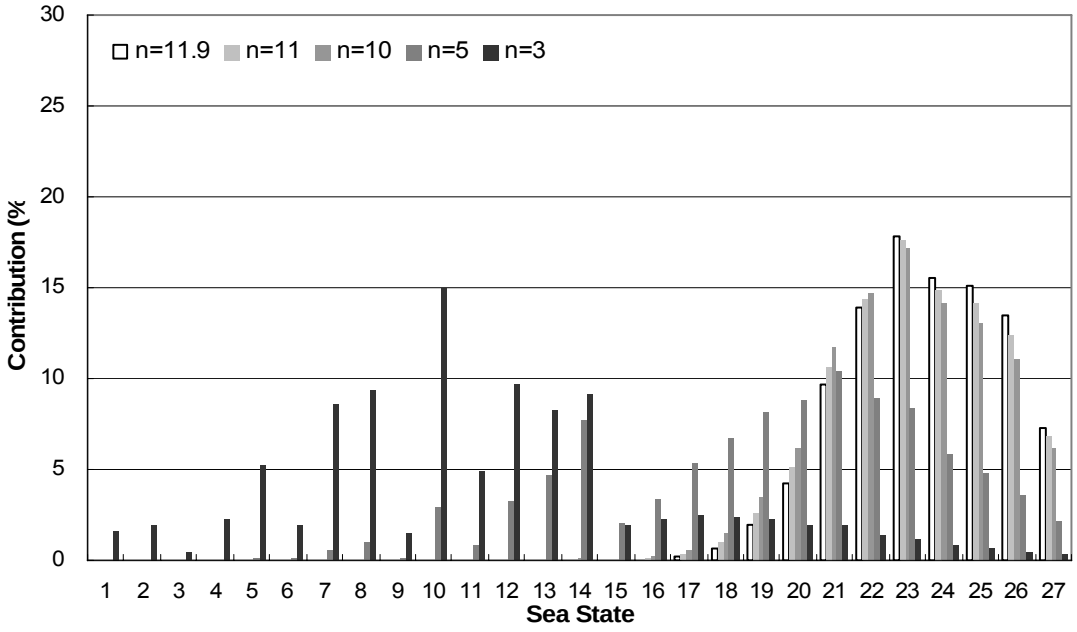

(b)

Fig. 43. Damage contribution of each sea state: power law S-N. (a) 102 ft (b) 5926 ft.

4.3.3. Steel liner

As the local combined loading analyses indicate, considerable amount of loads are transferred from the termination of a joint to the steel liner. Especially, fatigue failure of the weld that joins the steel liner to the metal end fitting is of the greatest concern. Using the same procedure, fatigue of the welds at the top and bottom of the composite riser region are evaluated. The estimated lives under two established S-N curves for welded sections are presented in Table 21. An equivalent steel riser system in the same environment has an estimated fatigue life of about a million years when the C curve is used [46]. The steel liner, whose thickness is less than 1/4 of the steel riser wall thickness, shows shorter but acceptable fatigue lives.

Table 21
Fatigue life estimates (steel liner)

Location	DNV-C	DNV-E
102 ft	7.7E+04	4.1E+03
5926 ft	8.7E+04	6.7E+03

(years)

The damage contribution of the sea states are shown in Fig. 44. The pattern for either location is very similar to the $n^* = 3$ case of the composite fatigue. Relatively, the bottom location is more influenced by the number of stress cycles. At the top location, stress magnitude plays as significant role as number of cycles.

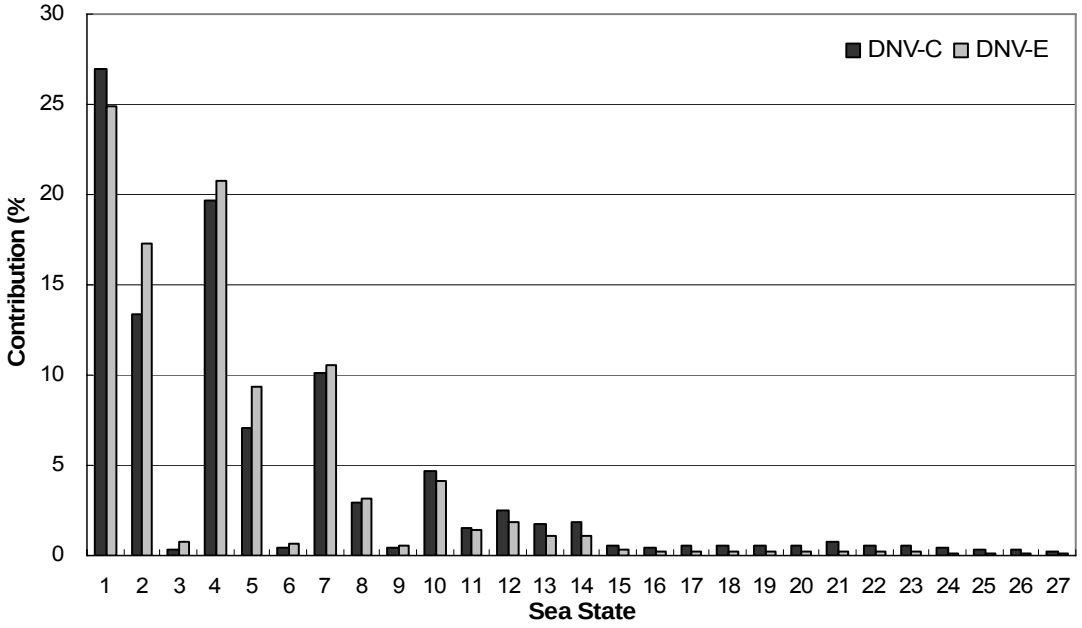

(a)

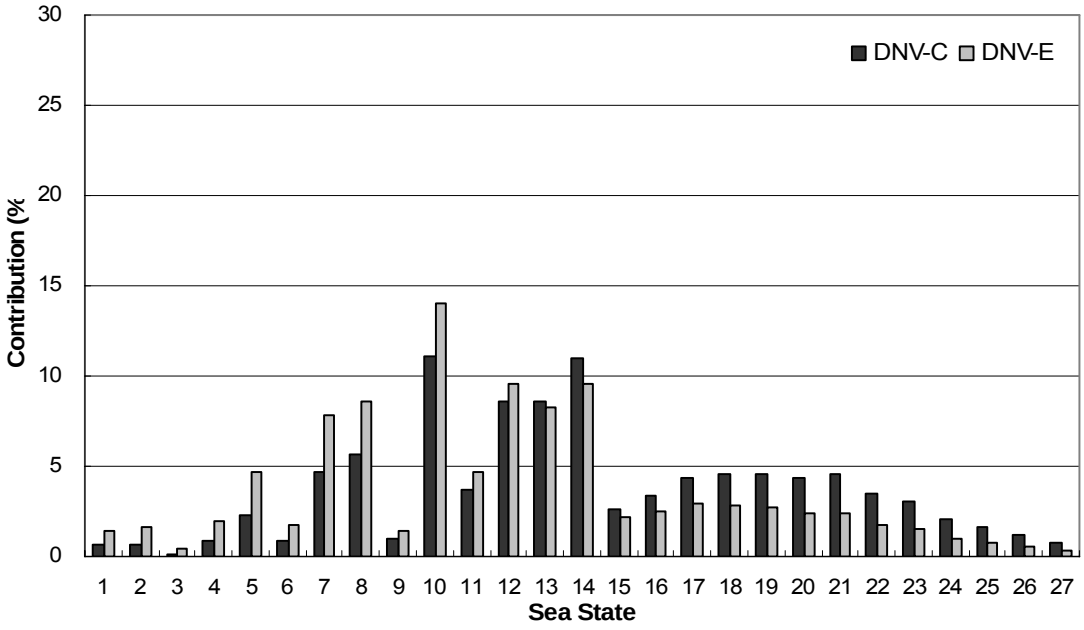

(b)

Fig. 44. Damage contribution of each sea state: steel liner. (a) 102 ft (b) 5926 ft.

4.4. Damping and resonant response

4.4.1. Damping

The specific damping capacity of the composite riser is estimated based on two sets of material data presented in Section 3.4. The lamina damping properties are considered as constants since specific damping capacity of a material is not affected by the stress amplitude as long as the amplitude is small [85]. Steel also provides damping, and the value differs from one alloy to another. Typical specific damping capacity of structural steel is about 1% (0.08% damping ratio), and this value is used in this study. Selected local loads from Table 10 are applied to the finite element model, and the resulting specific damping capacity is found to remain constant regardless of the choice of load condition. Although the local lamina stresses depend on the applied loads, contribution of each local stress component to the total strain energy does not vary significantly between different load cases. Note that σ_1 in axial layers are significantly large. Table 22 shows the energy quantities and specific damping properties resulting from two sets of lamina damping properties presented in Section 3.4.

Table 22
Estimated specific damping capacity of the composite riser based on lamina damping properties

Ref [86]				**Ref [83]**			
ΔU (in-lb)	U (in-lb)	ψ (%)	ζ (%)	ΔU (in-lb)	U (in-lb)	ψ (%)	ζ (%)
74.2	9043	0.82	0.07	113.6	9043	1.26	0.1

Regardless of the choice of lamina damping properties, the specific damping capacity of the composite riser is rather small and is of the same order as the specific damping capacity in the fiber direction (ψ_1) of the unidirectional lamina. Although it is not certain that the material properties used in this study are representative of typical carbon / epoxy laminae, the composite riser is not likely to have much higher damping due to its specially orthotropic lay-up and high axial stiffness, E_1. Major energy dissipation can be originated from local 2 and 12 directions, but in this particular lay-up, energies associated with those directions are relatively small. However, note that the estimates only involve the steel liner and composite body. Addition of protective layers or liners, which are usually glass / epoxy and/or elastomeric materials, may increase the specific damping capacity to some extent. Also, MCI may account for significant energy dissipation. At the current stage of composite riser research, it is not possible to determine a definitive range of damping. In the subsequent section, the largest estimate among the reported (a damping ratio of 2.3% from Ref. [93]) is assumed to perform vibration response analyses.

As discussed in Section 3.4, stiffness proportional damping, which reduces high frequency vibrations, is customarily used for offshore structures. Before carrying out steady state frequency sweep analyses to verify this common practice, natural frequencies of simple beam models are extracted. First, three short (100, 500, and 1000 ft) hinged-free beams consisting of composite riser joints are analyzed. The beams are assumed to be weightless, and no top tension is applied. The lowest natural mode is a rigid body mode. In this study, the steady state responses near the second natural frequency with stiffness proportional damping representing 0.1% damping ratio are examined. The peak (ω_0) and bandwidth (ω_1 and ω_2: frequencies on either side of resonant frequency for which the amplitude is $1/\sqrt{2}$ times the resonant amplitude) frequencies of the second mode and the calculated damping ratios are presented in Table 23.

Table 23

Bandwidth frequencies and damping ratio of short composite beams with stiffness proportional damping

l_{beam}	ω_0 (rad/s)	ω_1 (rad/s)	ω_2 (rad/s)	ζ (%)
100 ft	1.5252	1.5237	1.52675	0.09999
500 ft	0.061202	0.061141	0.061263	0.09967
1000 ft	0.015302	0.015287	0.015305	0.06143

The above results show that stiffness proportional damping does not yield the desired damping response for the 1000-ft beam. Since the practice of using stiffness proportional damping originated from experience related with steel structures, a steel beam of the identical length is analyzed in the same manner, with a damping ratio of 0.08%. Although the natural frequency of the steel beam is 0.0130694 Hz, which is slightly lower than the composite beam, the response faithfully showed the intended damping ratio with an error less than 0.002%. This may be accounted for by higher stiffness of the steel beam.

Next, a 6000-ft composite beam is analyzed with the same procedure. To approximate the actual riser condition, a distributed weight of 31 lbs/ft and 300 kip top tension are applied, and the riser bottom is constrained against motion. The analysis compares the two types of damping representation, stiffness proportional and mass proportional, at multiple natural frequencies. The responses near the first four modes are investigated, assuming a constant damping ratio regardless of excitation frequency and mode. Expectedly, the natural frequencies are very low, and stiffness proportional damping had very little effect on the responses. The calculated damping ratio based on the responses is less than 1% of the intended damping (ζ = 0.1%) in all modes. On the other hand, mass proportional damping showed excellent correspondence with the response, as shown in Table 24. A 6000-ft top tensioned steel beam also showed desired response when only mass proportional damping is specified.

Table 24

Bandwidth frequencies and damping ratio of 6000-ft composite beam with mass proportional damping

	ω_0 (rad/s)	ω_1 (rad/s)	ω_2 (rad/s)	ζ (%)
Mode 1	0.010993	0.010982	0.011004	0.10006
Mode 2	0.037895	0.037857	0.037933	0.10028
Mode 3	0.063822	0.063757	0.063887	0.10185
Mode 4	0.089685	0.089595	0.089775	0.10035

4.4.2. Excitation

First, the natural frequencies of the composite riser system in water (added mass taken into account) are obtained. Five modes, whose frequencies are close to the dominating wave frequencies of major storm conditions, are selected to study resonant responses. The natural mode shapes and frequencies are presented in Fig. 45 and Table 25. Note that the number of antinode (locations of vibration maxima) increases as mode number increases. Another feature of interest is the wavelength of a mode shape; it is smaller at the bottom due to the linearly decreasing tension.

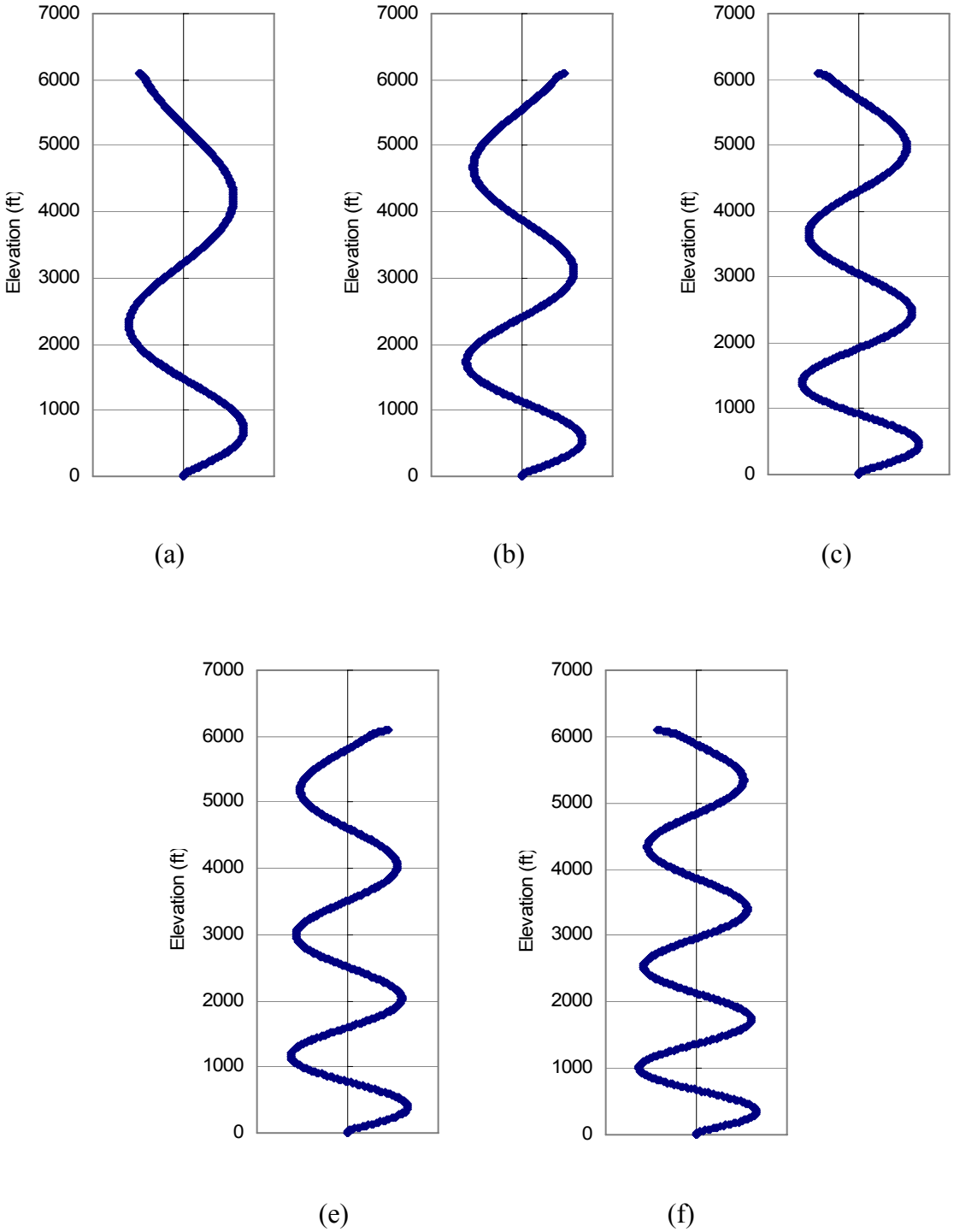

Fig. 45. Natural modes. (a) mode 4 (b) mode 5 (c) mode 6 (d) mode 7 (e) mode8.

Table 25

Natural frequencies and periods of the composite riser system

Mode	ω_0 (rad/s)	***f*** (Hz)	***T*** (sec)
4	0.3765	0.05992	16.688
5	0.4852	0.07722	12.949
6	0.5943	0.09459	10.572
7	0.7038	0.11201	8.928
8	0.8136	0.12948	7.723

In the next series of studies, the top of the riser is excited at each of the natural frequencies, and the resulting in-line and transverse responses are observed. Neither in-line response nor transverse response shows increases in vibration amplitude as can be seen in Fig. 46. However, the transverse response reaches steady state faster. Displacement and bending moment over one steady-state cycle of each excitation are presented in Fig. 47 - Fig. **50**. The hollow data markers represent no-damping responses, and the solid markers show the responses when 2.3% damping ratio is specified in the form of mass proportional damping.

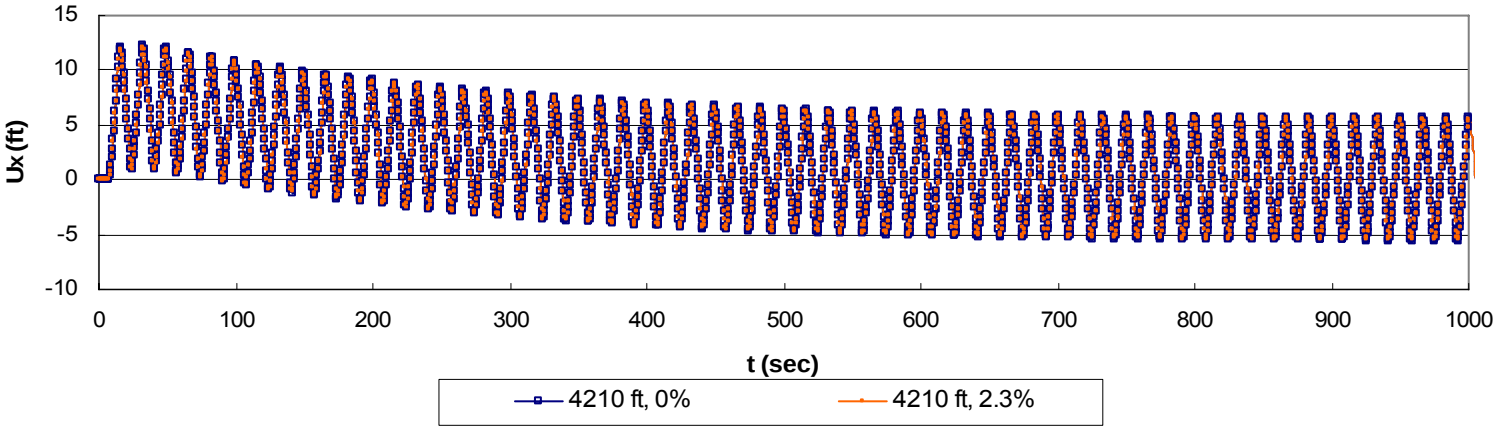

(a)

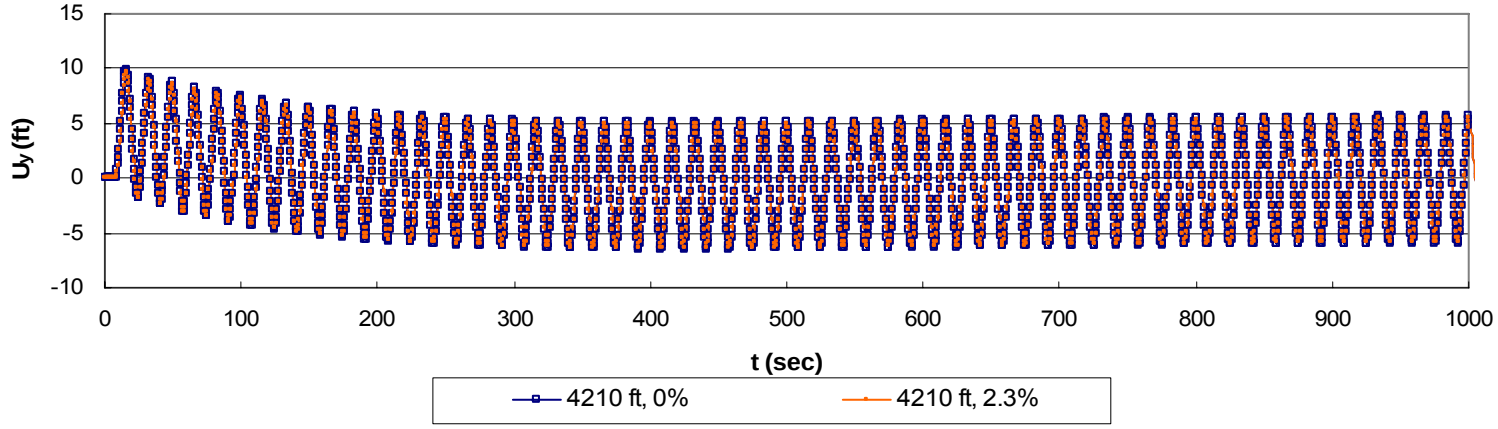

(b)

Fig. 46. Transient to steady state, mode 4 (ω = 0.3765 rad/s) at 4510 ft. (a) in-line (b) transverse.

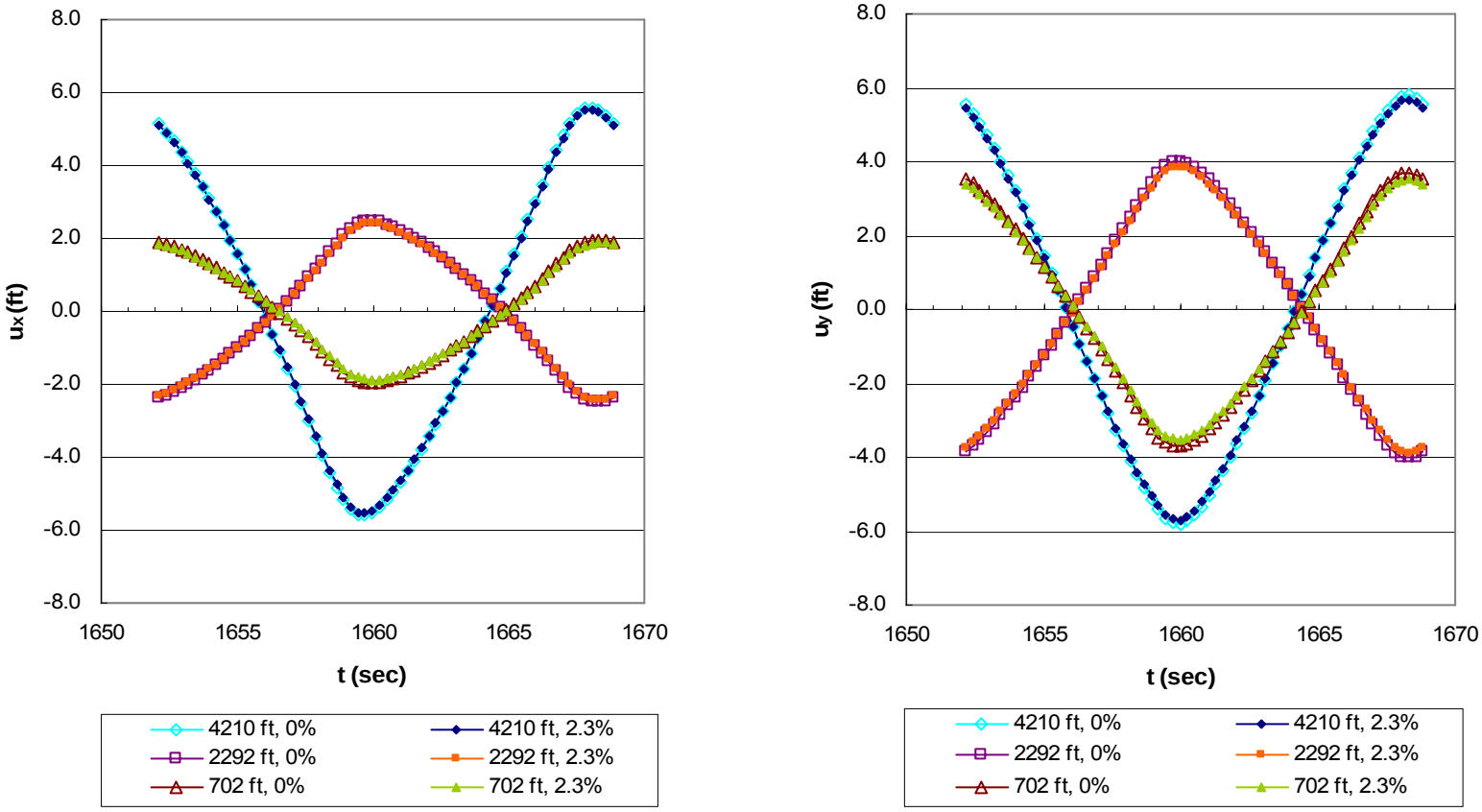

(a) (b)

Fig. 47. Displacements at antinodes of mode 4 (ω = 0.3765 rad/s). (a) in-line (b) transverse.

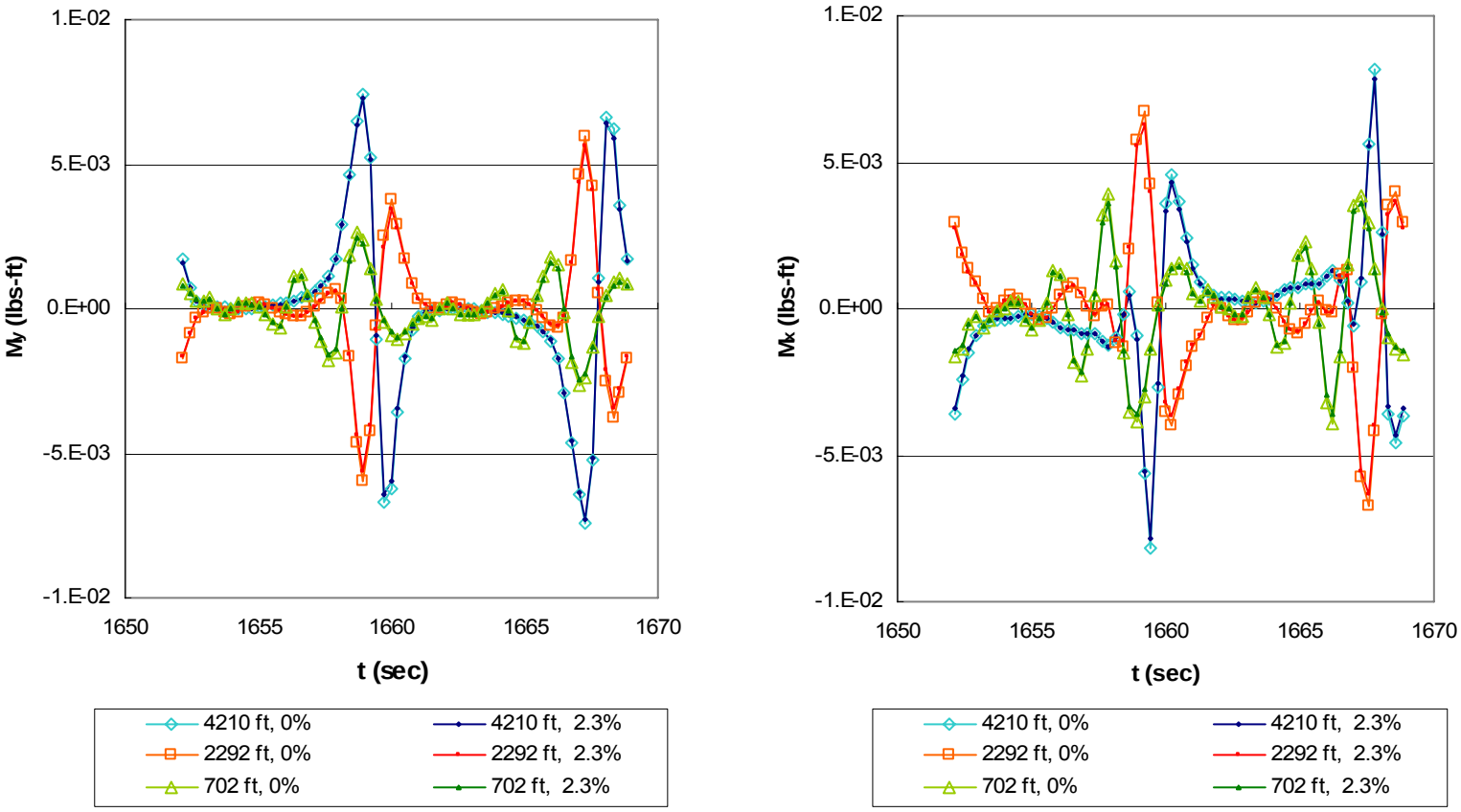

(a) (b)

Fig. 48. Bending moment at antinodes of mode 4 (ω = 0.3765 rad/s). (a) in-line (b) transverse.

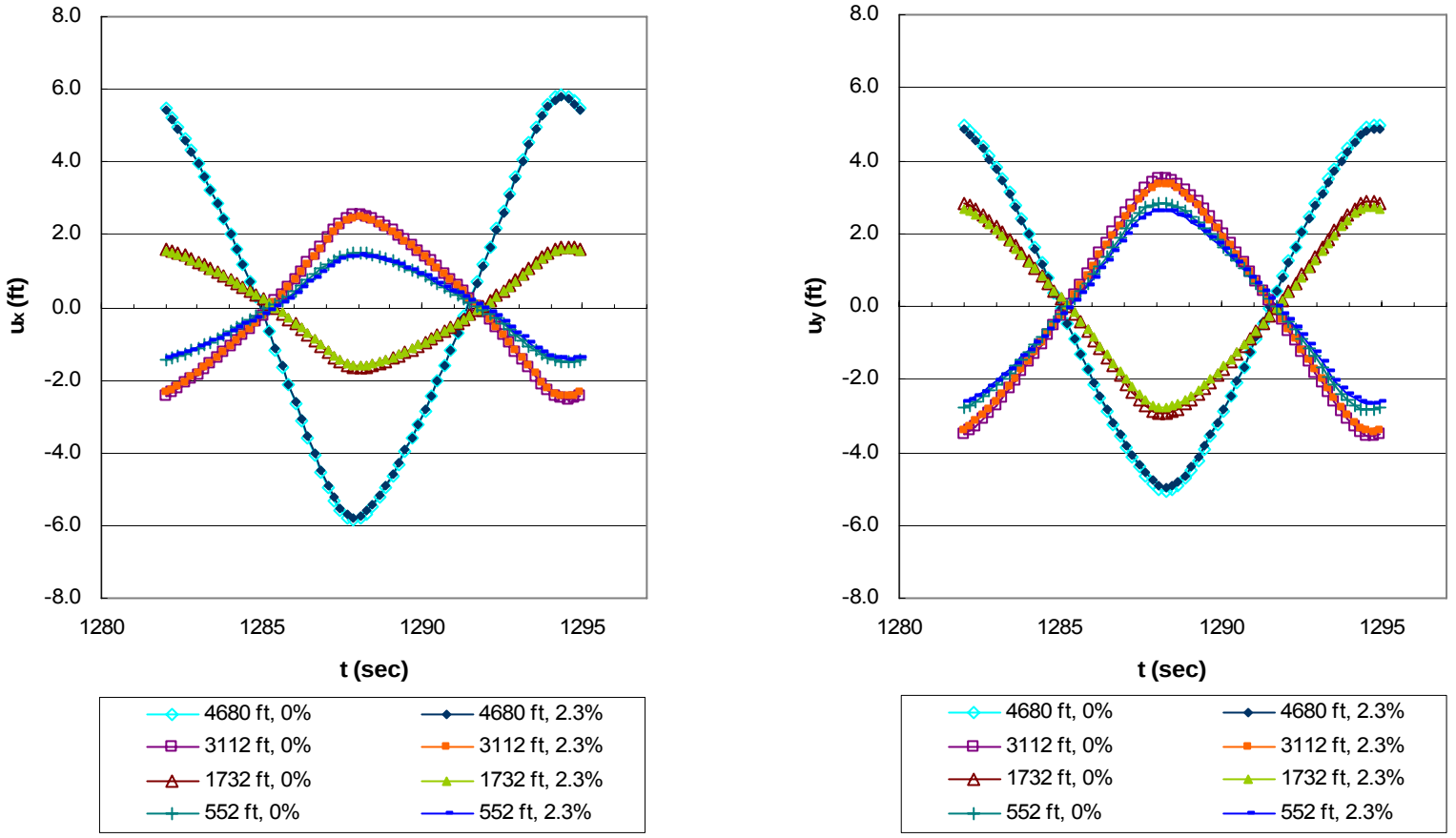

(a) (b)

Fig. 49. Displacements at antinodes of mode 5 (ω = 0.4852 rad/s). (a) in-line (b) transverse.

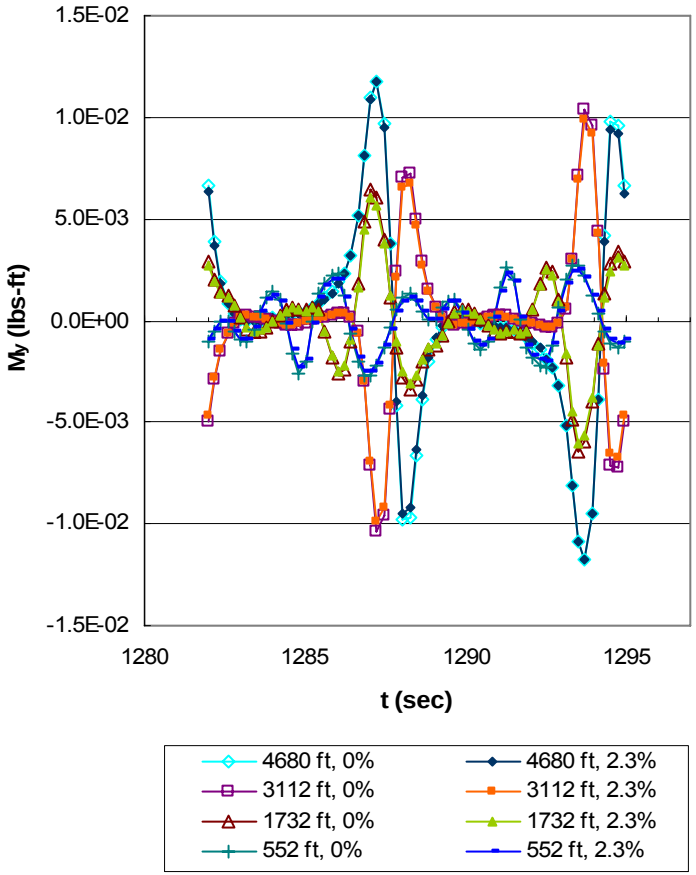

(a)

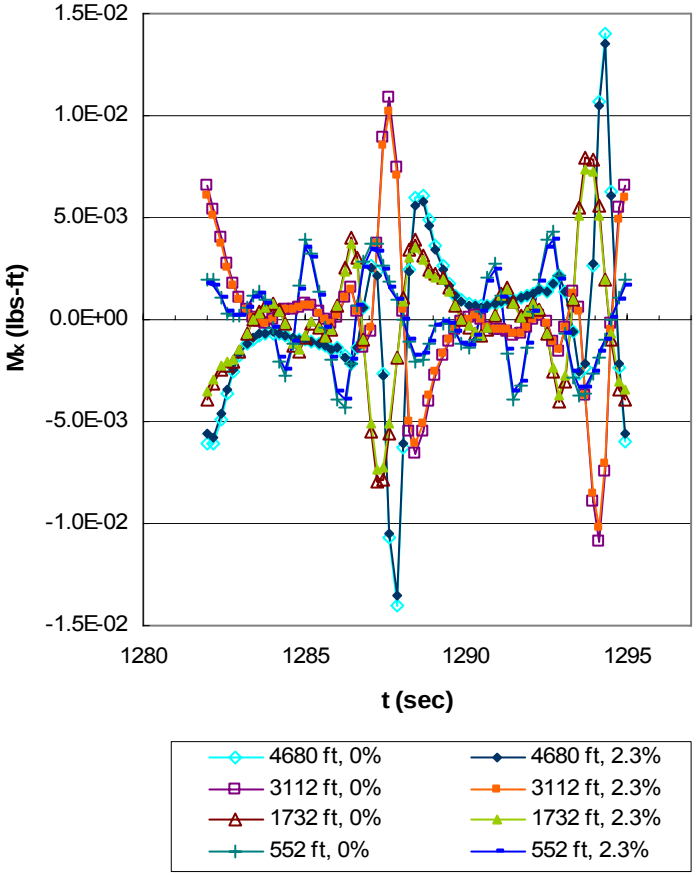

(b)

Fig. 50. Bending moment at antinodes of mode 5 (ω = 0.4852 rad/s). (a) in-line (b) transverse.

The constant vibration amplitude is due to the fact that fluid drag resists the movement of the structure. In most situations, resonance of a beam occurs from superposition of vibration waves [95]. When a wave sent from one end is reflected back and forth and is in phase with subsequent waves caused by a periodic excitation, the vibration amplitude increases significantly over time. In the case of the oscillating composite riser, no such reflection occurs. By the time a wave travels down and reaches the bottom end, it becomes extinct as can be seen in time snapshots of Fig. 51. Shapshots of transverse vibration concurrent with the in-line vibration are presented in Fig. 52. When the 6000-ft composite beam from Section 4.4.1 is oscillated in air, the response at the bottom antinode increases as shown in Fig. 53 (a). The effect of damping is more pronounced with apparent resonance in Fig. 53 (b). In Table 26, steady state vibration amplitudes at antinodes of modes 4 through 8 are presented. Decrease in vibration amplitudes at the top antinodes due to the specified damping is very small: about 1% for in-line vibration and 2% for transverse. At the bottom antinodes, damping reduces amplitudes by up to 11%.

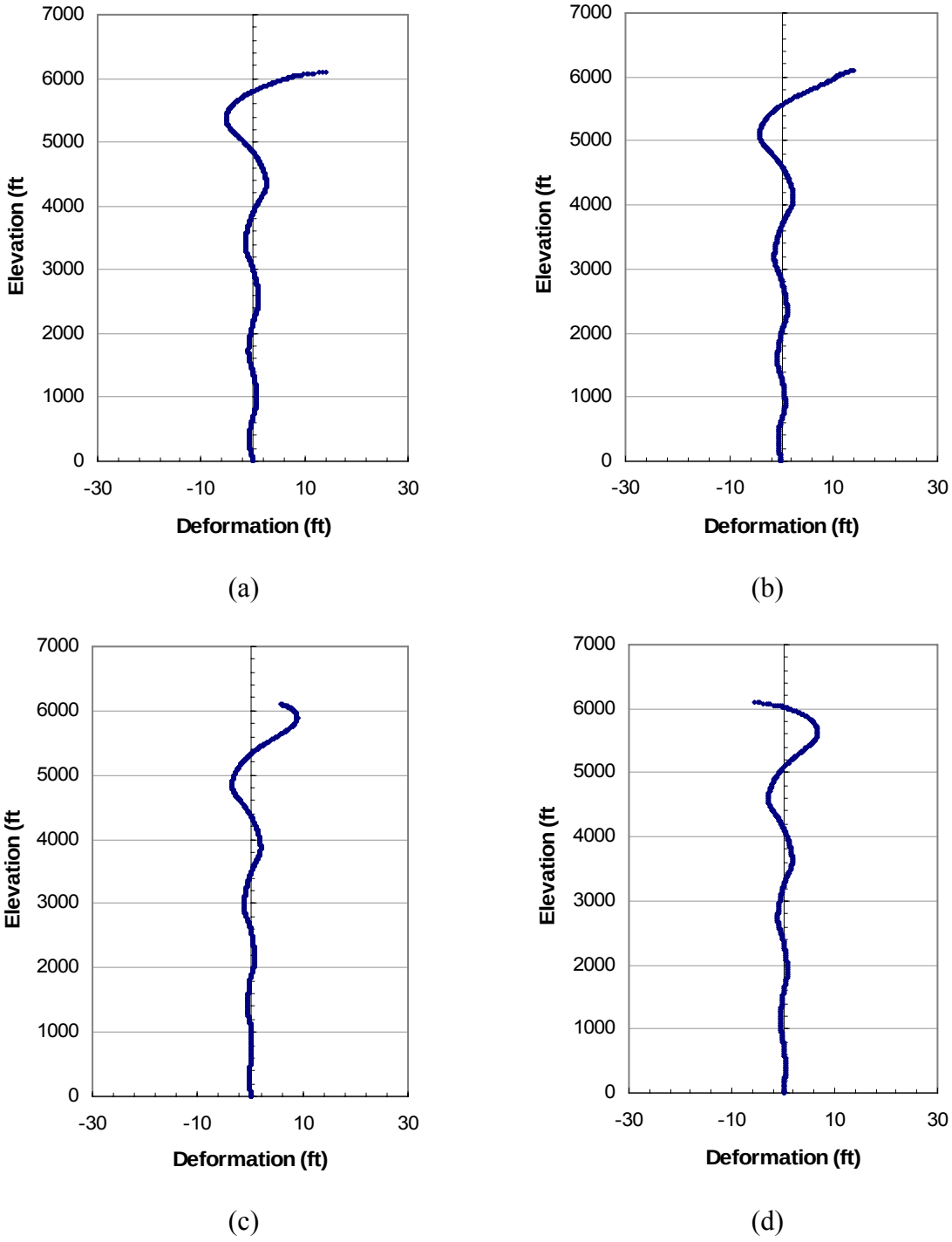

Fig. 51. Time snapshots of in-line vibration of composite riser, mode 8 (ω = 0.81357 rad/s). (a) 768.7 sec (b) 769.6 sec (c) 770.6 sec (d) 771.6 sec.

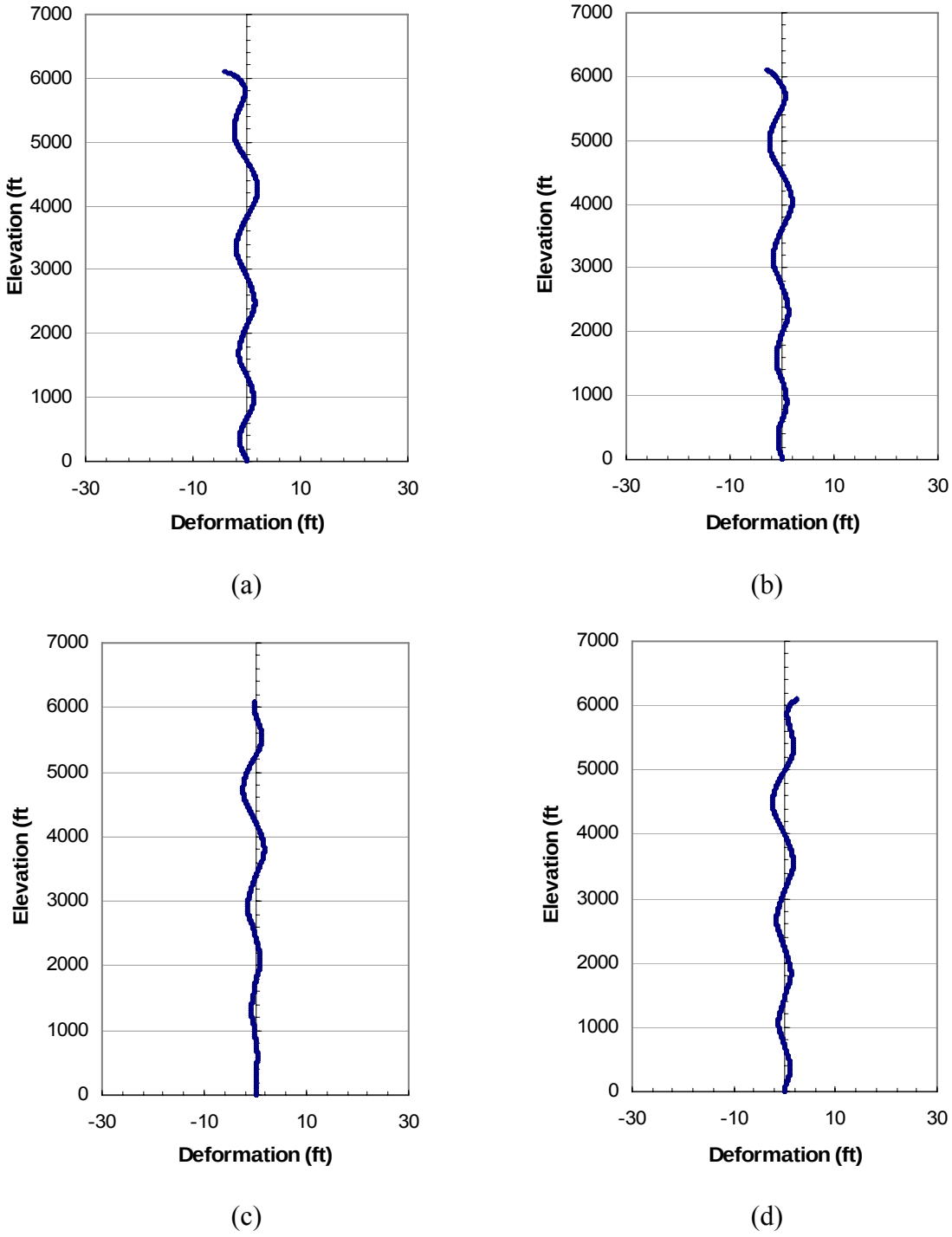

Fig. 52. Time snapshots of transverse vibration of composite riser, mode 8 (ω = 0.81357 rad/s). (a) 768.7 sec (b) 769.6 sec (c) 770.6 sec (d) 771.6 sec.

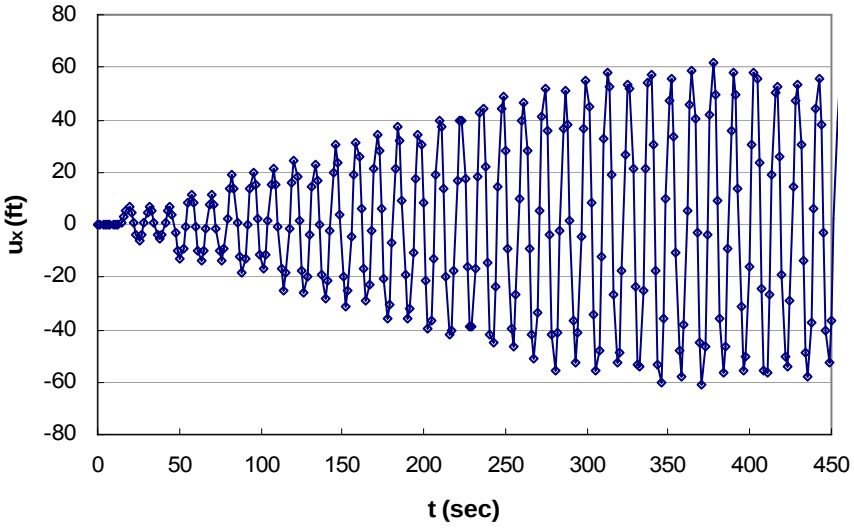

(a)

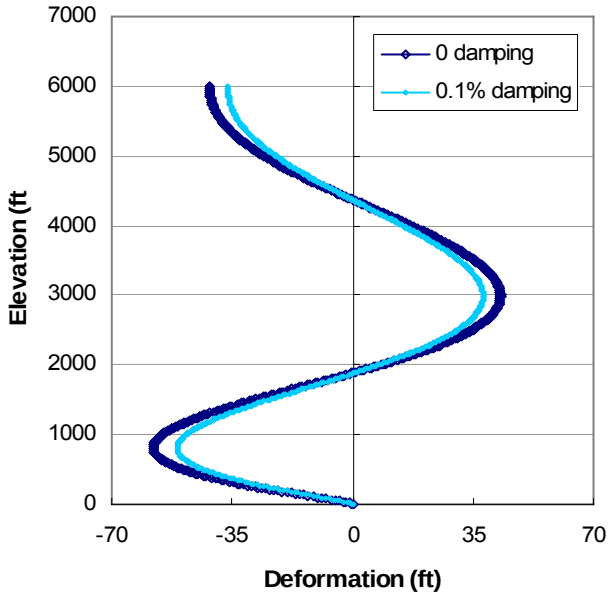

(b)

Fig. 53. Vibration response of 6000-ft composite beam in air. (a) increase of vibration amplitude at bottom antinode (b) snapshot at 436 sec.

Table 26

Vibration amplitude of composite riser

Mode	antinode elevation (ft)	Amplitude, in-line (ft)		Amplitude, transverse (ft)	
		$\zeta = 0$	$\zeta = 2.30\%$	$\zeta = 0$	$\zeta = 2.30\%$
Mode 4 T=16.69 s	4210	5.60	5.54	5.80	5.69
	2292	2.49	2.43	4.02	3.87
	702	1.96	1.89	3.70	3.52
Mode 5 T=12.95 s	4680	5.85	5.78	5.02	4.92
	3112	2.53	2.47	3.53	3.40
	1732	1.67	1.60	2.91	2.75
	552	1.49	1.42	2.83	2.65
Mode 6 T=10.57 s	4980	5.98	5.91	4.00	3.92
	3652	2.64	2.57	3.16	3.03
	2462	1.63	1.57	2.54	2.39
	1392	1.28	1.21	2.28	2.12
	462	1.20	1.13	2.27	2.09
Mode 7 T=8.93 s	5190	5.85	5.78	2.86	2.80
	4040	2.70	2.62	2.73	2.61
	2992	1.65	1.58	2.27	2.13
	2032	1.22	1.15	1.98	1.83
	1172	1.05	0.98	1.87	1.71
	392	1.01	0.94	1.87	1.70
Mode 8 T=7.72 s	5350	5.40	5.34	2.11	2.06
	4340	2.65	2.58	2.33	2.23
	3402	1.64	1.58	2.00	1.87
	2532	1.18	1.12	1.74	1.60
	1742	0.96	0.89	1.59	1.44
	1012	0.86	0.80	1.54	1.38
	352	0.87	0.80	1.57	1.40

For comparison, the steel riser is oscillated at two of its natural frequencies: ω = 0.3782 rad/s (mode 3) and 0.8345 rad/s (mode 6). The amplitude of the sinusoidal forcing function is again 10 ksi, and a damping ratio of 0.08% is applied in the form of mass proportional damping. Table 27 presents the amplitudes at the antinodes. For the steel riser, the amplitudes at the low-elevation antinodes are relatively large when compared to the responses of the composite riser shown in Table 26. Fig. 54 and Fig. 55 show time snapshots of the vibrations of the steel riser.

Table 27

Vibration amplitude of steel riser

Mode	**Antinode Elevation** (ft)	**Amplitude** (ft)	
		in-line	**transverse**
Mode 3 T=16.61	3254	6.00	5.25
	914	4.92	5.96
	4851	4.15	1.77
Mode 6 T=7.53	3534	2.96	2.26
	2354	2.41	2.45
	1324	2.21	2.61
	424	2.24	2.80

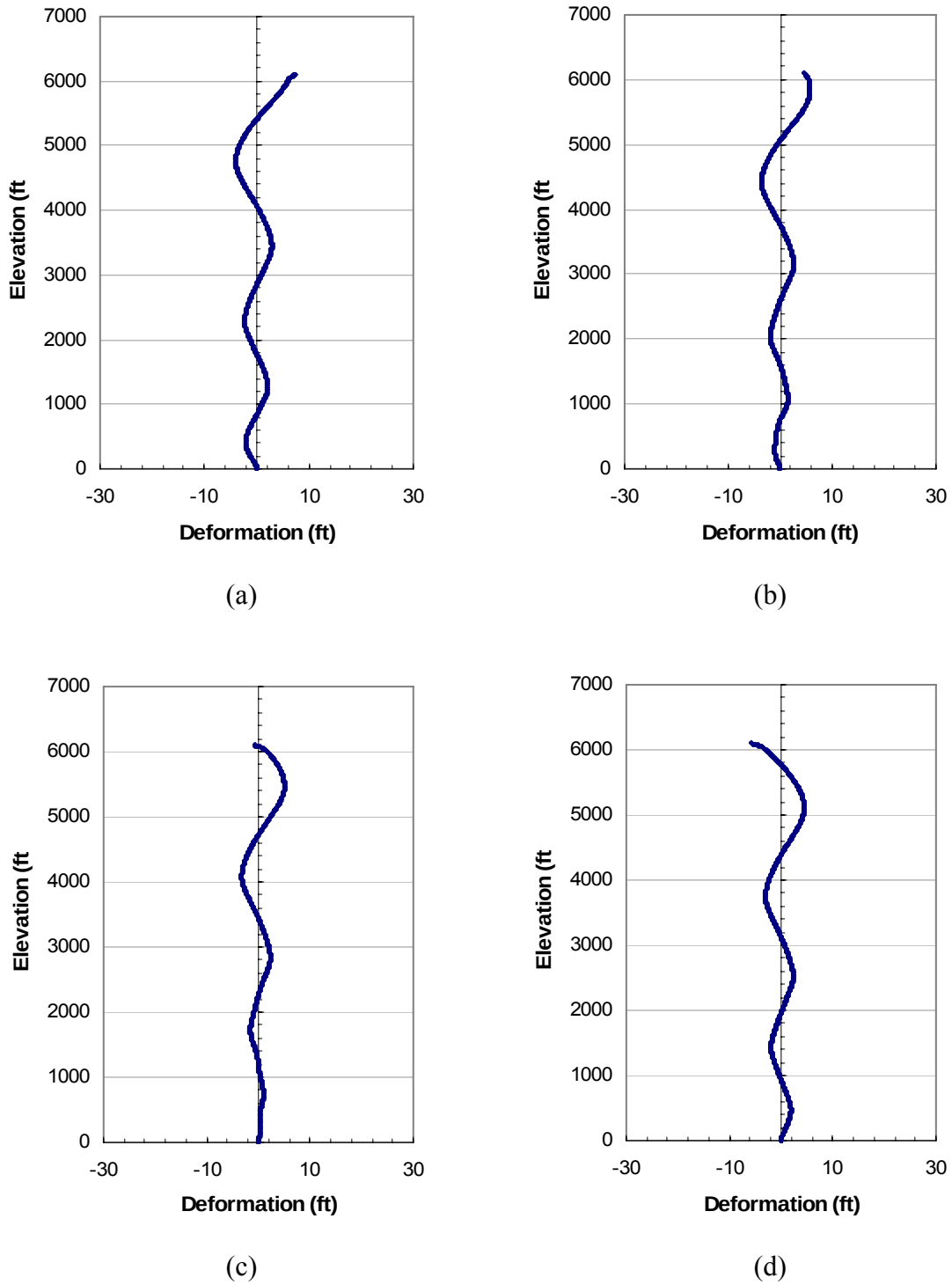

Fig. 54. Time snapshots of in-line vibration of steel riser, mode 6 (ω = 0.83451 rad/s). (a) 749.4 sec (b) 750.3 sec (c) 751.3 sec (d) 752.2 sec.

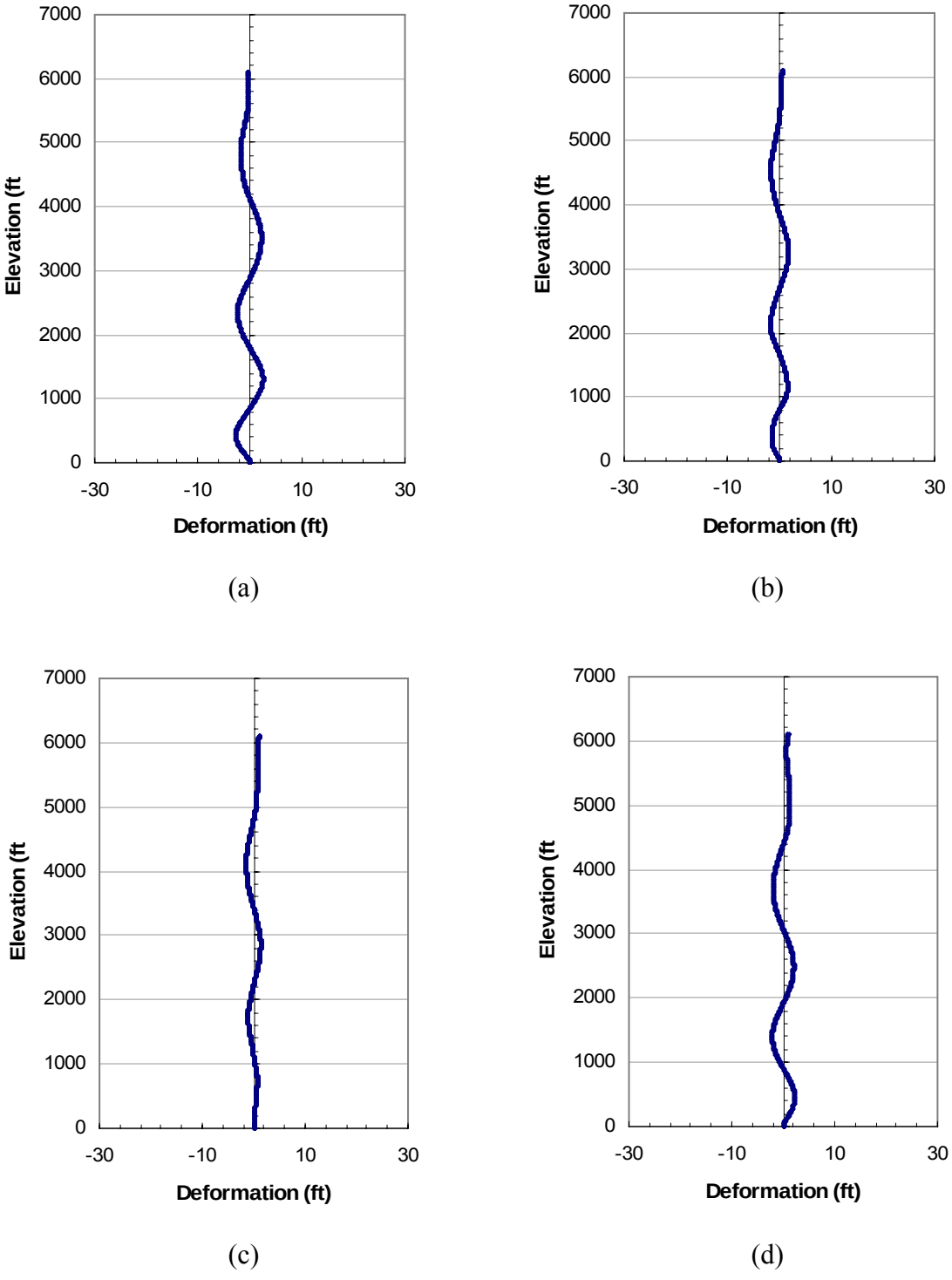

Fig. 55. Time snapshots of transverse vibration of steel riser, mode 6 (ω = 0.83451 rad/s). (a) 749.4 sec (b) 750.3 sec (c) 751.3 sec (d) 752.2 sec.

5. SUMMARY AND CONCLUSIONS

In this study, capacities and structural responses of a composite riser under various service and environmental loads have been investigated primarily through computational simulations. The analyses focused on identification of damage initiation and progression and on the discovery of the unique aspects of composite riser behavior. Even though the composite riser is expected to meet the same service requirements as steel risers, yet composite risers offer unlimited design possibilities: different lay-up, different combinations of constituent materials, introduction of new liner materials, and so on. The benefits will become most significant when they are tailored to a specific system and operating environment.

The current composite riser design consists of alternating hoop and axial layers. Due to the fact that the cylinder is near specially orthotropic, there is very little coupling between the two orientations. As a result, the pressure capacities are governed by the hoop layers, and the performance under combined axial tension / bending moment is determined by the axial layers. However, the use of the internal steel liner often limits the capabilities of the composite riser; although its function is not to share the applied loads, but to ensure fluid-tightness and to protect the structural composite from gouging, it inevitably carries significant amount of loads. This fact often complicates analyses and evaluations as observed throughout this study.

The performance of the composite riser associated with its hoop direction was evaluated by applying internal or external pressure. The resistance to extreme internal pressure caused by a leak in the production tubing is limited by the steel liner. However, it should be noted that yielding of the liner is not to be translated as burst of the entire wall, since the pressure is still sustained by the composite hoop layers and exceeding yield strength does not immediately lead to loss of containment. Moreover, the extreme pressure is not usually maintained for an extended period of time, and slight yielding leaves compressive residual stress in the liner upon returning to the normal operating pressure. It was observed that yielding of the liner caused slight increase in the slope of

load vs. stress graphs of the composite layers. Additional stress imposed on the hoop layers due to matrix cracking in the axial layers was not as apparent.

The collapse capacity of the composite riser, if the liner is firmly attached to the structural composite, far exceeds the hydrostatic pressure of 6000-ft water depth environment, even with moderate geometric imperfections. When a debond exists and pressure accumulates at the interface, the collapse capacity of the entire riser is determined solely by the deformation of the steel liner. Plastic collapse of a partially debonded steel liner does not occur immediately after yielding. Collapse is more dependent on the manner in which the deformation of the separated area progresses under incremental pressure. Although combinations of debond areas and large geometric imperfection may drastically impair the collapse resistance, the collapse capacities of the composite riser is larger than the maximum hydrostatic pressure in any extreme cases.

The advantage of the composite riser is pronounced in global analyses. Due to its light weight, axial tension and bending moment are reduced throughout the structure as well as on the composite riser itself, which gives flexibility for the design of other components in the system such as stress joint, tensioner, or even the hull of the platform. The major local stresses at the top of the composite riser resulting from various storm conditions show the same pattern; only the lower and upper limits vary. All the layers, including the internal liner, show ample amount of safety margins. Especially, the axial layers only experience up to 10% of their long term allowable. Therefore, it is reasonable to attempt to expand the use of the composite joints to the locations where the standard steel joints are currently used. To facilitate these evaluations, damage analyses for various combinations of axial tension and bending moment were performed. The results are used to construct damage envelopes which are equivalent to a failure envelope for steel. Since the composite riser wall consists of three major component, i.e., steel liner, hoop layers, and axial layers, there are three sets of curves indicating damage. From the envelopes, influence of damage history on subsequent damage can be clearly observed.

In the fatigue analysis, variation of wave-induced stress which is irregular in reality is converted into multiple regular stress cycles through Rayleigh probability

density function. Since the S-N curves of composite materials depend strongly on the combinations of constituent materials, various S-N curves were used to estimate the probable range of the fatigue life of the composite riser. The calculated results were highly sensitive to the material constants for the S-N relationships. In the stress histogram for a certain sea state, individual stress level is extremely small, usually associated with number of cycles far greater than billions. Therefore, it is important to construct an S-N curve that faithfully represents the high number of cycles range. Also, the representation, semi-log or log-log, must fit the high cycles range.

In the damping and resonant response analyses, a qualitative evaluation of the impact of supposedly high damping of composite risers has been performed. Based on the damping provided by the constituent materials, there is not likely to be significant amount of energy dissipation in the composite riser. Although there are other energy dissipation sources such as interfaces, cracks, and other liner materials that are not considered in this study, the major cause of the small estimated damping is its specially-orthotropic lay-up and high E_1. Storage and dissipation of energy occurs in the axial layers, where the damping capacity is merely in the same order as metals. It should be emphasized that while it is true that composites offer excellent damping properties, not all lay-ups can take advantage of this benefit. Another common misconception is that stiffness proportional damping is always appropriate for analyses of offshore structures. For stiff (metal) structures in moderate water depth, stiffness proportional damping is suitable, but as observed in the frequency sweep analyses, it may not be descriptive of larger scale structures. In the excitation simulations, resonance at natural frequencies did not take place due to the strong resistance by drag force. An interesting observation is that vibration amplitudes at low elevations of the composite riser are very small, while those of the steel riser are as large as mid-elevation. In other words, the vibration waves descending from the top of the steel riser do not deteriorate as much as they do in the composite riser. However, they are not strong enough to be reflected back and forth and amplify the vibration.

When designing a composite riser, it is extremely important to determine the

design requirements and allowables for each component comprising the wall. For example, the local debonding and plastic collapse of the steel liner investigated in this study is based on the assumption of damaged outer waterproof barrier generally made of synthetic rubber. If the riser was designed against water penetration through outer protective layers, liner collapse would not need to be treated as a problem of great magnitude. The intention of the study was to reveal the potential and limitations of composite risers. Exploration of design rationale or design optimization is left as subjects of future studies.

REFERENCES

[1] Pelsoci TM. Composites manufacturing technologies: Applications in automotive, petroleum, and civil infrastructure industries, NIST GCR 04-863. National Institute of Standards and Technology, 2004.

[2] Baud RD, Peterson RH, Richardson GE, French LS, Regg J, Montgomery T, Williams TS, Doyle C, Dorner M. Deepwater Gulf of Mexico 2002: America's expanding frontier. Minerals Management Service, U.S. Department of Interior, 2002.

[3] Demirbilek Z. Tension leg platform - a state of the art review. New York: American Society of Civil Engineers, 1989.

[4] Saad P, Salama MM, Jahnsen O. Application of composites to deepwater top tensioned riser systems. 21st International Conference on Offshore Mechanics and Arctic Engineering, Oslo, Norway, 2002. OMAE2002-28325.

[5] Salama MM. Lightweight materials for deepwater offshore structures. Offshore Technology Conference, Houston, TX, 1986. OTC 5185.

[6] Salama MM. Some challenges and innovations for deepwater developments. Offshore Technology Conference, Houston, TX, 1997. OTC 8455.

[7] Karayaka M, Wu S, Wang SS, Lu X, Ganguly P. Composite production riser dynamics and its effects on tensioners, stress joints, and size of deep water tension leg platforms. Offshore Technology Conference, Houston, TX, 1998. OTC 8666.

[8] Lo KH, Williams JG, Karayaka M, Salama MM. Progress, challenges, and opportunities in the application of composites offshore. In: Wang SS, Williams, J. G., and Lo, K. H., editors. Composite Materials for Offshore Operations - 3, Houston, TX: University of Houston - CEAC, 2000. p. 3-17.

[9] Andersen WF, J. AJ, Mickelson CS, Sweeney TF. The application of advanced composite technology to marine drilling riser systems: Design, manufacturing and test. Offshore Technology Conference, Houston, TX, 1997. OTC 8433.

[10] Leveque ME, Salama MM, Sokoll RE, Paulshus B. The magnolia composite

production riser joint industry project: Design, testing and manufacturing overview. Composite Materials for Offshore Operations - 4, Houston, TX, 2005.

[11] Melve B, Fjelheim P, Storhaug T. Long term experience of the composite drilling riser joint at Heidrun TLP. Composite Materials for Offshore Operations - 4, Houston, TX, 2005.

[12] Andersen WF, Burgdorf O, Sweeney TF. Comparative analysis of 12,500 ft. Water depth steel and advanced composite drilling risers. Offshore Technology Conference, Houston, TX, 1998. OTC 8732.

[13] Andersen WF, Anderson JJ, Landriault LS. Full-scale testing of prototype composite drilling riser joints - interim report. Offshore Technology Conference, Houston, TX, 1998. OTC 8668.

[14] Baldwin DD, Newhouse NL, Lo KH, Burden RC. Composite production riser design. Offshore Technology Conference, Houston, TX, 1997. OTC 8431.

[15] Baldwin DD, Lo KH, Long JR. Design verification of a composite production riser. Offshore Technology Conference, Houston, TX, 1998. OTC 8664.

[16] Drey MD, Salama MM, Long JR, Abdallah MG, Wang SS. Composite production riser - testing and qualification. Offshore Technology Conference, Houston, TX, 1997. OTC 8432.

[17] Johnson DB, Salama MM, Long JR, Wang SS. Composite production riser - manufacturing development and qualification testing. Offshore Technology Conference, Houston, TX, 1998. OTC 8665.

[18] Johnson DB, Baldwin DD, Long JR. Mechanical performance of composite production risers. Offshore Technology Conference, Houston, TX, 1999. OTC 11008.

[19] Karayaka M. Integration of advanced material components to deepwater platforms. Offshore Technology Conference, Houston, TX, 2000. OTC 12027.

[20] Salama MM. Lightweight materials for mooring lines of deepwater tension leg platforms. Marine Technology 1984;21(3):234-241.

[21] Sparks C. Lightweight composite production risers for a deep water tension leg

platform. 5th International Conference on Offshore Mechanics and Arctic Engineering, Tokyo, Japan, 1986. p. 86-93.

[22] Sparks CP, Odru P, Bono H, Metivaud G. Mechanical testing of high-performance composite tubes for tlp production risers. Offshore Technology Conference, Houston, TX, 1988. OTC 5797.

[23] Jansons JO, Glejbol K, Rytter J, Aniskevich AN, Arnautov AK, Kulakov VL. Effect of water absorption, elevated temperatures and fatigue on the mechanical properties of carbon-fiber-reinforced epoxy composites for flexible risers. Mechanics of Composite Materials 2002;38(4):299-310.

[24] Ochoa OO, Ross GR. Hybrid composites: Models and tests for environmental aging. Journal of Reinforced Plastics and Composites 1998;17(9):787-799.

[25] Ross GR, Ochoa OO. Hygroscopic response of hybrid tubes. Corrosion95, Orlando, FL: National Association of Corrosion Engineers, 1995. Paper #140.

[26] Ross GR, Ochoa OO. Environmental effects on unsymmetric composite laminates. Journal of Thermoplastic Composites 1991;4:266-284.

[27] Venkatesan R, Dwarakadasa ES, Ravindran M. Study on behavior of carbon fiber-reinforced composite for deep sea applications. Offshore Technology Conference, Houston, TX, 2002. OTC 14325.

[28] Baldwin D, Lo KH. A general discussion on riser composite/metal interface design and analysis. In: Wang SS, Williams JG., Lo KH, editors. Composite Materials for Offshore Operations - 3, Houston, TX: University of Houston - CEAC, 2000. p. 215-229.

[29] Baldwin DD, Johnson DB. Rigid composite risers: Design for purpose using performance-based requirements. Offshore Technology Conference, Houston, TX, 2002. OTC 14319.

[30] Salama MM, Stjern, G, Storhaug T, Spencer B, Echtermeyer A. The first offshore field installation for a composite riser joint. Offshore Technology Conference, Houston, TX, 2002. OTC 14018.

[31] Sun CT, Li S. Three-dimensional effective elastic constants for thick laminates.

Journal of Composite Materials 1988;22:629-639.

[32] Abaqus user's manual. Pawtucket, RI: Hibbitt, Karlsson & Sorensen, Inc., 2000.

[33] Cook RD, Young WC. Advanced mechanics of materials. New York: Macmillan, 1985.

[34] Young WC. Roark's formulas for stress and strain. New York: McGraw-Hill, 1989.

[35] Lai WM, Rubin D, Krempl E. Introduction to continuum mechanics. Woburn, MA: Butterworth-Heinemann, 1993.

[36] Verijenko VE, Adali S, Tabakov PY. Stress distribution in continuously heterogeneous thick laminated pressure vessels. Composite Structures 2001;54:371-377.

[37] Xia M, Takayanagi H, Kemmochi K. Analysis of multi-layered filament-wound composite pipes under internal pressure. Composite Structures 2001;53:483-491.

[38] The composite materials handbook. MIL-HDBK-17. West Conshohocken, PA: ASTM International, 2002.

[39] Hashin Z. Failure criteria for unidirectional fiber composites. Journal of Applied Mechanics 1980;47:329-334.

[40] Jones RM. Mechanics of composite materials. New York: McGraw-Hill, 1975.

[41] Daniel IM, Ishai O. Engineering mechanics of composite materials. New York: Oxford University Press, 1994.

[42] Hua Z, Dongxing L. Mechanical analysis of the elastic buckling of an orthogonal anisotropic circular conical shell under uniform external pressure. International Journal of Pressure Vessels and Piping 1991;48:111-122.

[43] Zou RD, Foster CG. Simple solution for buckling of orthotropic circular cylindrical shells. Thin-Walled Structures 1995;22:143-158.

[44] Mirfakhraei P, Redekop D. Buckling of circular cylindrical shells by the differential quadrature method. International Journal of Pressure Vessels and Piping 1998;75:347-353.

[45] Vodenitcharova T, Ansourian P. Buckling of circular cylindrical shells subject to uniform lateral pressure. Engineering Structures 1996;18(8):604-614.

[46] Miller CA. Personal Communication. Stress Engineering Services, Inc. Houston, TX, 2005.

[47] Reddy JN. An introduction to the finite element method. McGraw-Hill, 1993.

[48] Cook RD. Concepts and applications of finite element analysis. John Wiley & Sons, 1981.

[49] Young RD, Fowler JR, Fisher EA, Luke RR. Dynamic analysis as an aid to the design of marine risers. Journal of Pressure Vessel Technology 1978;100:200-205.

[50] Burke BG. An analysis of marine risers for deep water. Offshore Technology Conference, Houston, TX, 1973. OTC 1771.

[51] Chakrabarti SK, Frampton RE. Review of riser analysis techniques. Applied Ocean Research 1982;4(2):73-90.

[52] Kirk CL, Etok EU, Cooper MT. Dynamic and static analysis of a marine riser. Applied Ocean Research 1979;1(3):125-135.

[53] Sorensen RM. Basic coastal engineering. New York: International Thompson Publishing, 1997.

[54] Design of risers for floating production systems (FPSs) and tension-leg platforms (TLPs). RP 2RD. American Petroleum Institute, 1998.

[55] Blevins RD. Flow-induced vibration. New York: Van Nostrand Reinhold, 1990.

[56] Krolikowski LP, Gay TA. An improved linearization technique for frequency domain riser analysis. Offshore Technology Conference, Houston, TX, 1980. OTC 3777.

[57] Miner MA. Cumulative damage in fatigue. Journal of Applied Mechanics 1945;12:159-164.

[58] Whitworth HA. A stiffness degradation model for composite laminates under fatigue loading. Composite Structures 1998;40(2):95-101.

[59] Yang JN, Jones DL, Yang SH, Meskini A. A stiffness degradation model for graphite/epoxy laminates. Journal of Composite Materials 1990;24:753-769.

[60] Halverson HG, Curtin WA, Reifsnider KL. Fatigue life of individual composite specimens based on intrinsic fatigue behavior. International Journal of Fatigue

1996;19(5):369-377.

[61] Hashin Z. Cumulative damage theory for composite materials: Residual life and residual strength methods. Composite Science and Technology 1985;23:1-19.

[62] Hashin Z, Rotem A. A fatigue failure criterion for fiber reinforced materials. Journal of Composite Materials 1973;7:448-464.

[63] Schaff JR, Davidson BD. Life prediction methodology for composite structures. Part I - Constant amplitude and two-stress level fatigue. Journal of Composite Materials 1997;31(2):128-157.

[64] Schaff JR, Davidson BD. A strength-based wearout model for predicting the life of composite structures. In: Armanios EA, editor. Composite materials: Fatigue and fracture. ASTM STP 1285. Volume 6, 1997. p. 179-200.

[65] Poursartip A, Ashby MF, Beaumont PWR. The fatigue damage mechanics of a carbon fibre composite laminate: I - Development of the model. Composite Science and Technology 1986;25:193-218.

[66] Tsai GC, Doyle JF, Sun CT. Frequency effects on the fatigue life and damage of graphite/epoxy composites. Journal of Composite Materials 1987;21:2-13.

[67] Hwang W, Han KS. Cumulative damage models and multi-stress fatigue life prediction. Journal of Composite Materials 1986;20:125-153.

[68] Harris B, Reiter H, Adam T, Dickson RF, Fernando G. Fatigue behaviour of carbon fibre reinforced plastics. Composites 1990;21(3):232-242.

[69] Guidance notes on spectral-based fatigue analysis for floating offshore structures. Houston, TX: American Bureau of Shipping, 2005.

[70] Green AK, Pratt PL. The axial fatigue behaviour of unidirectional type IIIs carbon fibre-epoxy composites. Composites 1974;5(2):63-66.

[71] Lee J, Daniel IM, Yaniv G. Fatigue life prediction of cross-ply composite laminates. In: Lagace PA, editor. Composite materials: Fatigue and fracture, second volume. ASTM STP 1012. Philadelphia: American Society of Testing and Materials, 1989. p. 19-28.

[72] Lorenzo L, Hahn HT. Fatigue failure mechanisms in unidirectional composites. In:

Hahn HT, editor. Composite materials: Fatigue and fracture. ASTM STP 907. Philadelphia: American Society of Testing and Materials, 1986. p. 210-232.

[73] Sims DF, Brogdon VH. Fatigue behavior of composites under different loading modes. In: Reifsnider KL, Lauraitis KN, editors. Fatigue of filamentary composite materials. ASTM STP 636. Philadelphia: American Society of Testing and Materials, 1977. p. 185-205.

[74] Kawai M. A phenomenological model for off-axis fatigue behavior of unidirectional polymer matrix composites under different stress ratios. Composites Part A: Applied Science and Manufacturing 2004;35(7-8):955-963.

[75] Fatigue design of offshore steel structures. Recommended practice DNV-RP-C203. Hovik, Norway: Det Norske Veritas, 2005.

[76] Chandra R, Singh SP, Gupta K. Damping studies in fiber-reinforced composites - a review. Composite Structures 1999;46:41-51.

[77] Hashin Z. Complex moduli of viscoelastic composites - I. General theory and application to particulate composites. International Journal of Solids and Structures 1970;6:539-552.

[78] Hashin Z. Complex moduli of viscoelastic composites - II. Fiber reinforced materials. International Journal of Solids and Structures 1970;6:797-807.

[79] Nashif AD, Jones DIG, Henderson JP. Vibration damping. New York: John Wiley & Sons, Inc., 1985.

[80] Suarez SA, Gibson RF, Sun CT, Chaturvedi SK. The influence of fiber length and fiber orientation on damping and stiffness of polymer composite materials. Experimental Mechanics 1986;26(2):175-184.

[81] Sun CT, Gibson RF, Chaturvedi SK. Internal material damping of polymer matrix composites under off-axis loading. Journal of Materials Science 1985;20:2575-2585.

[82] Adams RD, Fox MAO, Flood RJL, Friend RJ, Hewitt RL. The dynamic properties of unidirectional carbon and glass fiber reinforced plastics in torsion and flexure. Journal of Composite Materials 1969;3:594-603.

[83] Gibson RF, Hwang SJ, Kwak H. Micromechanical modeling of damping in composites including interphase effects. 36th International SAMPE Symposium, San Diego, CA: Society for Advancement of Materials and Process Engineering, 1991. p. 592-606.

[84] Hwang SJ, Gibson RF. The use of strain energy-based finite element techniques in the analysis of various aspects of damping of composite materials and structures. Journal of Composite Materials 1992;26(17):2585-2605.

[85] Lin DX, Ni RG, Adams RD. Prediction and measurement of the vibrational damping parameters of carbon and glass fibre-reinforced plastic plates. Journal of Composite Materials 1984;18:132-152.

[86] Ni RG, Adams RD. The damping and dynamic moduli of symmetric laminated composite beams - theoretical and experimental results. Journal of Composite Materials 1984;18:104-121.

[87] Ni RG, Adams RD. A rational method for obtaining the dynamic mechanical properties of laminae for predicting the stiffness and damping of laminated plates and beams. Composites 1984;15(3):193-199.

[88] Vantomme J. A parametric study of material damping in fibre-reinforced plastics. Composites 1995;26(2):147-153.

[89] Lim F, Bridge C, Hatten S, Robinson L, Beynet P. Structural damping test for the BP Shah Deniz risers. Offshore Technology Conference, Houston, TX, 2005. OTC 17198.

[90] Omar AF, Karayaka M, Murray JJ. A comparative study of the performance of top-tensioned composite and steel risers under vortex-induced loading. Offshore Technology Conference, Houston, TX, 1999. OTC 11009.

[91] Patel MH, Witz JA. Compliant offshore structures. Oxford: Butterworth-Heinemann, 1991.

[92] Huang KZ. Composite TTR design for an ultradeepwater TLP. Offshore Technology Conference, Houston, TX, 2005. OTC 17159.

[93] Majewski T. Damping evaluation of composite cylinders (Unpublished report).

Texas A&M University, College Station, TX, 2002.

[94] Dynamic risers. Offshore standard DNV-OS-F201. Hovik, Norway: Det Norske Veritas, 2001.

[95] Sparks C. Transverse modal vibrations of vertical tensioned risers. Oil & Gas Science and Technology 2002;57(1):71-86.

[96] Lo KH. Personal Communication. Shell. Houston, TX, 2006.

[97] Bathe KJ. Finite element procedures. Englewood Cliffs, NJ: Prentice Hall, 1996.

[98] Whitney JM. Structural analysis of laminated anisotropic plates. Lancaster, PA: Technomic Publishing Company, Inc., 1987.

APPENDIX A

The displacements for the 8 node linear hexahedron written in terms of the interpolation functions, N_i, are as follows [32,48,97].

$$u = \sum_i^8 N_i u_i$$

$$\begin{aligned} &= \frac{1}{8}(1-\xi)(1-\eta)(1-\zeta)u_1 + \frac{1}{8}(1+\xi)(1-\eta)(1-\zeta)u_2 \\ &+ \frac{1}{8}(1+\xi)(1+\eta)(1-\zeta)u_3 + \frac{1}{8}(1-\xi)(1+\eta)(1-\zeta)u_4 \\ &+ \frac{1}{8}(1-\xi)(1-\eta)(1+\zeta)u_5 + \frac{1}{8}(1+\xi)(1-\eta)(1+\zeta)u_6 \\ &+ \frac{1}{8}(1+\xi)(1+\eta)(1+\zeta)u_7 + \frac{1}{8}(1-\xi)(1+\eta)(1+\zeta)u_8 \end{aligned} \tag{34}$$

$$v = \sum_i^8 N_i v_i$$

$$w = \sum_i^8 N_i w_i$$

where

ξ, η, and ζ : normal or natural coordinates, ranging from -1 to +1

u_i : nodal displacements

Strains are obtained by taking first derivatives of the displacements with respect to local coordinates:

$$\begin{Bmatrix} \varepsilon_x \\ \varepsilon_y \\ \varepsilon_z \\ \gamma_{xy} \\ \gamma_{yz} \\ \gamma_{zx} \end{Bmatrix} = \begin{bmatrix} 1 & 0 & 0 & 0 & 0 & 0 & 0 & 0 & 0 \\ 0 & 0 & 0 & 0 & 1 & 0 & 0 & 0 & 0 \\ 0 & 0 & 0 & 0 & 0 & 0 & 0 & 0 & 1 \\ 0 & 1 & 0 & 1 & 0 & 0 & 0 & 0 & 0 \\ 0 & 0 & 0 & 0 & 0 & 1 & 0 & 1 & 0 \\ 0 & 0 & 1 & 0 & 0 & 0 & 1 & 0 & 0 \end{bmatrix} \begin{Bmatrix} \frac{\partial u}{\partial x} & \frac{\partial u}{\partial y} & \frac{\partial u}{\partial z} & \frac{\partial v}{\partial x} & \frac{\partial v}{\partial y} & \frac{\partial v}{\partial z} & \cdots \end{Bmatrix}^T \tag{35}$$

Since the interpolation function is defined in terms of natural coordinates, a coordinate transformation is required to obtain the strains. Using the chain rule, the following matrix equation can be obtained.

$$\begin{Bmatrix} \frac{\partial u}{\partial \xi} \\ \frac{\partial u}{\partial \eta} \\ \frac{\partial u}{\partial \zeta} \end{Bmatrix} = \begin{bmatrix} \frac{\partial x}{\partial \xi} & \frac{\partial y}{\partial \xi} & \frac{\partial z}{\partial \xi} \\ \frac{\partial x}{\partial \eta} & \frac{\partial y}{\partial \eta} & \frac{\partial z}{\partial \eta} \\ \frac{\partial x}{\partial \zeta} & \frac{\partial y}{\partial \zeta} & \frac{\partial z}{\partial \zeta} \end{bmatrix} \begin{Bmatrix} \frac{\partial u}{\partial x} \\ \frac{\partial u}{\partial y} \\ \frac{\partial u}{\partial z} \end{Bmatrix} = [J] \begin{Bmatrix} \frac{\partial u}{\partial x} \\ \frac{\partial u}{\partial y} \\ \frac{\partial u}{\partial z} \end{Bmatrix} \tag{36}$$

where [*J*] is called the Jacobian matrix. The inverse of [*J*] enables the strains in Eqn (35) to be rewritten in terms of derivatives of the displacements with respect to the natural coordinates.

The linear displacement fields of isoparametric linear elements are incapable of representing the bending mode since the edges remain straight under bending. For example, the deformations for a linear rectangular element under pure bending are

$$u = \overline{u}\,\xi\eta = \overline{u}\,\frac{4xy}{WH}, \quad v = 0 \tag{37}$$

where $\overline{u}$ is the displacement at the nodes, *W* is the width of the element, and *H* is the height. The inaccurate displacement *v* results in the following shear strain,

$$\gamma_{xy} = \frac{\partial u}{\partial y} + \frac{\partial v}{\partial x} = \bar{u}\frac{4x}{WH} \tag{38}$$

which should not exist in pure bending.

Incompatible mode elements have additional bending modes in the displacement fields. Each displacement field of the 8 noded incompatible mode element has three internal degrees of freedom, a_i, which are not associated with any node.

$$u = \sum_{i}^{8} N_i u_i + (1-\xi^2)a_1 + (1-\eta^2)a_2 + (1-\zeta^2)a_3 \tag{39}$$

The summation part is identical to Eqn. (34).

The interpolation functions for the 20 node quadratic hexahedron can be grouped into two types. The interpolation functions associated with the corner nodes are

$$\begin{aligned} N_1 &= -\frac{1}{8}(1-\xi)(1-\eta)(1-\zeta)(2+\xi+\eta+\zeta) \\ N_2 &= -\frac{1}{8}(1+\xi)(1-\eta)(1-\zeta)(2-\xi+\eta+\zeta) \\ &\cdots \end{aligned} \tag{40}$$

Those associated with the mid-edge nodes are

$$\begin{aligned} N_9 &= \frac{1}{4}(1-\xi)(1+\xi)(1-\eta)(1-\zeta) \\ N_{10} &= \frac{1}{4}(1+\xi)(1-\eta)(1+\eta)(1-\zeta) \\ &\cdots \end{aligned} \tag{41}$$

APPENDIX B

For an elastic orthotropic material, which has three mutually perpendicular planes of symmetry, the constitutive relations can be represented by the following equation.

$$\begin{Bmatrix} \sigma_1 \\ \sigma_2 \\ \sigma_3 \\ \tau_{23} \\ \tau_{31} \\ \tau_{12} \end{Bmatrix} = \begin{bmatrix} C_{11} & C_{12} & C_{13} & 0 & 0 & 0 \\ C_{12} & C_{22} & C_{23} & 0 & 0 & 0 \\ C_{13} & C_{23} & C_{33} & 0 & 0 & 0 \\ 0 & 0 & 0 & C_{44} & 0 & 0 \\ 0 & 0 & 0 & 0 & C_{55} & 0 \\ 0 & 0 & 0 & 0 & 0 & C_{66} \end{bmatrix} \begin{Bmatrix} \varepsilon_1 \\ \varepsilon_2 \\ \varepsilon_3 \\ \gamma_{23} \\ \gamma_{31} \\ \gamma_{12} \end{Bmatrix} \tag{42}$$

The stiffness matrix is symmetric and consists of nine independent constants. The same applies to its inverse, compliance matrix. In many cases, fibers are considered to be packed in a hexagonal array, and the mechanical properties in 2 and 3 directions are identical. When a material meets this condition, the material is called transversely isotropic with the 2-3 plane being the plane of isotropy. Since the properties in 2 and 3 directions are identical, the number of independent constants reduces to five, since $C_{12} = C_{13}$, $C_{22} = C_{33}$, and $C_{55} = C_{66}$.

When expressing the constitutive relations in terms of engineering constants, it is more convenient to use compliances as presented in the following equation.

$$\begin{Bmatrix} \varepsilon_1 \\ \varepsilon_2 \\ \varepsilon_3 \\ \gamma_{23} \\ \gamma_{31} \\ \gamma_{12} \end{Bmatrix} = \begin{bmatrix} \frac{1}{E_1} & -\frac{\nu_{21}}{E_2} & -\frac{\nu_{31}}{E_3} & 0 & 0 & 0 \\ -\frac{\nu_{21}}{E_2} & \frac{1}{E_2} & -\frac{\nu_{32}}{E_3} & 0 & 0 & 0 \\ -\frac{\nu_{31}}{E_3} & -\frac{\nu_{32}}{E_3} & \frac{1}{E_3} & 0 & 0 & 0 \\ 0 & 0 & 0 & \frac{1}{G_{23}} & 0 & 0 \\ 0 & 0 & 0 & 0 & \frac{1}{G_{13}} & 0 \\ 0 & 0 & 0 & 0 & 0 & \frac{1}{G_{12}} \end{bmatrix} \begin{Bmatrix} \sigma_1 \\ \sigma_2 \\ \sigma_3 \\ \tau_{23} \\ \tau_{31} \\ \tau_{12} \end{Bmatrix} \tag{43}$$

where $E_i \nu_{ji} = E_j \nu_{ij}$.

The stiffness terms in Eqn. (42) can be expressed in terms of engineering constants using the following relations [41,98].

$$\begin{aligned} C_{11} &= \frac{(1-\nu_{23}\nu_{32})E_1}{\Delta} \\ C_{12} &= \frac{(\nu_{12}+\nu_{13}\nu_{32})E_2}{\Delta} \\ C_{13} &= \frac{(\nu_{13}+\nu_{12}\nu_{23})E_3}{\Delta} \\ C_{22} &= \frac{(1-\nu_{13}\nu_{31})E_2}{\Delta} \\ C_{23} &= \frac{(\nu_{23}+\nu_{21}\nu_{13})E_3}{\Delta} \\ C_{33} &= \frac{(1-\nu_{12}\nu_{21})E_3}{\Delta} \\ C_{44} &= G_{23} \\ C_{55} &= G_{13} \\ C_{66} &= G_{12} \end{aligned} \tag{44}$$

where

$$\Delta = \begin{vmatrix} 1 & -\nu_{21} & -\nu_{31} \\ -\nu_{12} & 1 & -\nu_{32} \\ -\nu_{13} & -\nu_{23} & 1 \end{vmatrix}$$

When a state of plane stress is assumed, Eqn. (42) is reduced to the following equation.

$$\begin{Bmatrix} \sigma_1 \\ \sigma_2 \\ \tau_{12} \end{Bmatrix} = \begin{bmatrix} Q_{11} & Q_{12} & 0 \\ Q_{12} & Q_{22} & 0 \\ 0 & 0 & Q_{66} \end{bmatrix} \begin{Bmatrix} \varepsilon_1 \\ \varepsilon_2 \\ \gamma_{12} \end{Bmatrix} \tag{45}$$

where

$$Q_{11} = \frac{E_1}{1-\nu_{12}\nu_{21}}$$

$$Q_{12} = \frac{\nu_{21}E_1}{1-\nu_{12}\nu_{21}}$$

$$Q_{22} = \frac{E_2}{1-\nu_{12}\nu_{21}}$$

$$Q_{66} = G_{12}$$

VITA

Won Ki Kim was born in Taegu, South Korea on November 1, 1973 and grew up in Seoul, South Korea. He entered the Mechanical Design and Production Engineering program at Yonsei University, Seoul, in 1992. In 1995, he joined the Korean Army and served in the 25th transportation battalion, U.S. Army, as an augmented soldier. He completed his service and returned to the university in 1997. Three semesters later, he received his B.S. degree and entered the joint graduate degree program from Yonsei University and Korea Institute of Science and Technology (KIST). In 2001, he received his M.S. degree in Mechanical Engineering. He continued to work at KIST as a researcher until he entered the Mechanical Engineering program at Texas A&M University in 2002. In 2003, he began working with Dr. Ozden Ochoa and participated in two composite riser projects of the Offshore Technology Research Center, granted by Minerals Management Services.

Won may be reached at
9507 Curry Landing Dr
Houston, TX 77095
wkim1101@gmail.com